STRUCTURES AND MATERIALS RESEARCH
DEPARTMENT OF CIVIL ENGINEERING
SERIES 100 ISSUE 6

# STRUCTURAL MODEL INVESTIGATIONS

# FOR

# OROVILLE DAM

A Report of an Investigation

by

Jerome M. Raphael
Associate Professor of Civil Engineering

to

THE DEPARTMENT OF WATER RESOURCES
STATE OF CALIFORNIA
Under Standard Service Agreement
No. 57-SA-100

Institute of Engineering Research
University of California
Berkeley, California

February, 1960

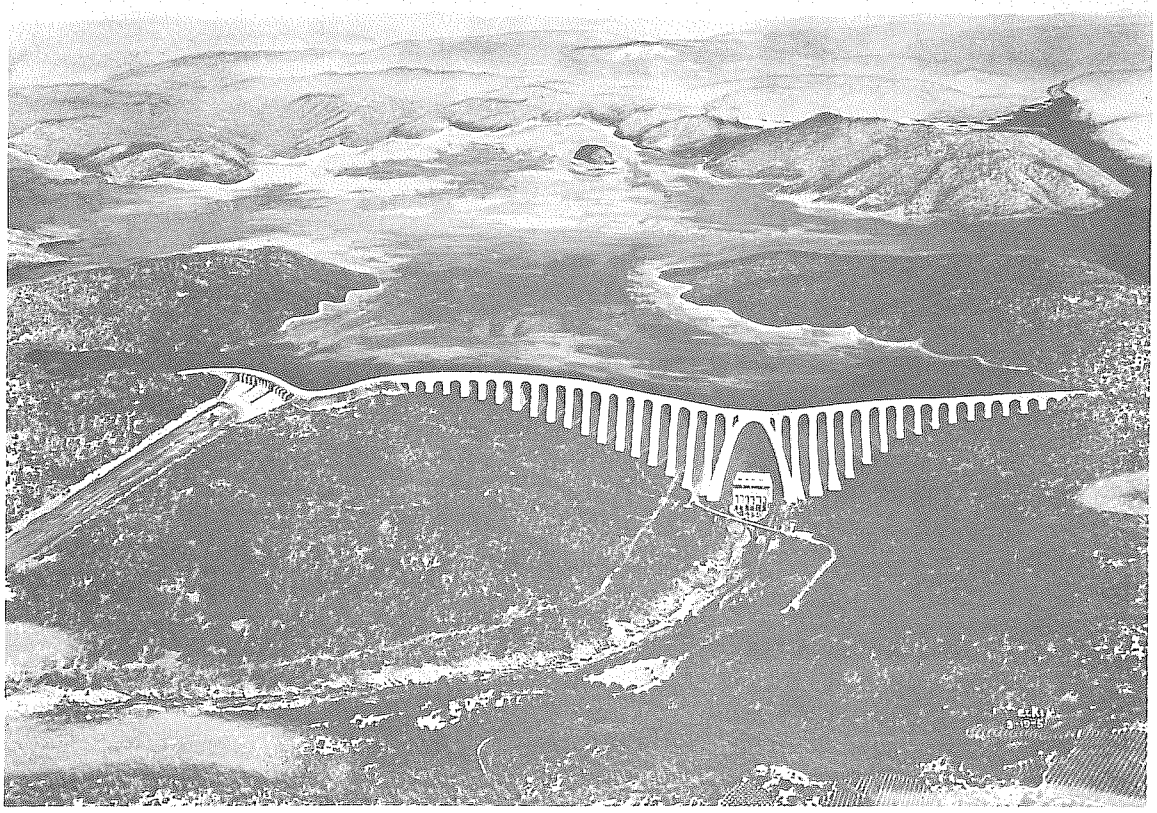

OROVILLE DAM, SPILLWAY, AND POWER PLANT

# TABLE OF CONTENTS


| | Page |
|---|---|
| INTRODUCTION | |
| Relation of the Feather River Project to the Structural Model Investigation | 1 |
| Previous Reports | 5 |
| Acknowledgements | 6 |
| PRELIMINARY CONSIDERATIONS | |
| General Assumptions and Requirements | 8 |
| Proportionality of Strain to Loading | 9 |
| Relative Size of Model and Foundation | 9 |
| Relative Stiffness of Dam and Foundation | 11 |
| Interaction of Structural Components | 12 |
| Area of Hydrostatic Loading | 12 |
| Method of Prototype Construction | 13 |
| CONSTRUCTION OF THE MODEL | |
| Selection of Material and Scale | 15 |
| General Scheme of Construction | 16 |
| Construction of Base Mold | 17 |
| The Plug Mold | 20 |
| The Main Arch Mold | 20 |
| Buttresses | 22 |
| The Testing Pit | 24 |
| Method of Pouring Plaster | 25 |
| Methods for Construction of Foundation | 26 |
| Construction of the Structural Models | 29 |

Page

TEST EQUIPMENT AND PROCEDURES

Hydrostatic Loading System 32

Manometer 38

Counterweight System 40

Instrumentation 42

Gage Locations 42

Strain Gages 43

Test Set, Switching, and Compensation 46

DETERMINATION OF STRESSES DUE TO HYDROSTATIC LOADING

Test Procedures 51

Model Similitude 54

Reduction of Data 58

Correction for Cross-Sensitivity of Strain Gages 58

Calculation of Principal Strains 60

Principal Stresses 62

Vertical and Horizontal Stresses and Shears 62

Normal Pressure Correction 63

Live Load Stresses 64

Deflections Due to Live Load 67

DETERMINATION OF STRESSES DUE TO DEAD LOAD

Dead Load Tests 69

Method of Applied Loads 69

Method of Inversion 69

Method of Immersion 70

Centrifugal Method 71

Page

DETERMINATION OF STRESSES DUE TO DEAD LOAD (Cont'd)

Method of Integration 73

Similitude Factors 75

Test Procedures 78

Dead Load Stresses 79

DETERMINATION OF STRESSES DUE TO COMBINED LOADS

Computation of Stresses Due to Combined Loads 89

Combined Live and Dead Load Stresses 89

DISCUSSION

Validity of Results 93

Comparison of Experimental and Theoretical Results 93

Statics Check 96

Recommendations 101

APPENDIX - PROPERTIES OF PLASTER-CELITE MIXTURES

Introduction 104

The Setting of Plaster 105

Plaster 108

Celite 113

Independence of Celite and Plaster 116

Test Procedures 117

Consistency 117

Modulus of Elasticity and Compressive Strength 120

Flexural Modulus of Elasticity 122

Sonic Modulus of Elasticity 124

The Water-Plaster Ratio and Its Effect on Modulus of Elasticity 127

The Water-Plaster Ratio and Its Effect on Strength 130

Page

APPENDIX (Cont'd)

Tensile Strength 131

Poisson's Ratio 133

Maximum Strain 134

The Effect of Drying on Strength and Elasticity 135

The Effect of Water and Celite on Consistency 139

Time of Set 141

Effect of Water and Celite on Time of Set 141

Effect of Temperature on Time of Set 143

Effect of Retarder on Time of Set 144

Effect of Retarder on Consistency 145

Volume Change During Setting 146

Shrinkage 151

Bleeding 151

Effect of Mixing Time on Modulus of Elasticity 152

Creep 153

Design of Heavy Plaster Mixtures 155

Conclusions 159

REFERENCES 162

## LIST OF ILLUSTRATIONS


| Figure | Title | Page |
|---|---|---|
| Frontispiece- | Oroville Dam, Spillway, and Powerplant | i |
| 1 | Types of Dams Considered for Oroville Dam | 3 |
| 2 | The Oroville Arch and Buttress Dam | 4 |
| 3 | Steps in Construction of Foundation Mold | 18 |
| 4. | Steps in Construction of Plug Mold | 21 |
| 5 | Steps in Construction of Main Arch Mold | 23 |
| 6 | Construction Schemes Used for Pouring Foundation | 27 |
| 7 | Isometric Cutaway View of the Block Foundation | 29 |
| 8 | The Completed Model Being Fitted With Strain Gages | 31 |
| 9 | Schematic View of Water Load Test Equipment | 33 |
| 10 | Actual Hydrostatic Pressure Gradient and Equivalent Stepped Gradient | 34 |
| 11 | Sketch of Differential Pressure Controller | 36 |
| 12 | Backup Frame Being Fitted with Air Bags | 37 |
| 13 | Mercury Manometer for Checking Air Bag Pressures | 39 |
| 14 | Effect of Counterweight Forces on Stability | 40 |
| 15 | General View of Reaction Frame and Counterweight | 41 |
| 16 | Strain Gage Locations | 44 |
| 17 | Test for Action of Strain Gage Rosettes | 46 |
| 18 | Switching Circuits | 47 |
| 19 | Arrangement of Strain Gage Recording Equipment | 48 |
| 20 | General View of Testing Area | 50 |
| 21 | Loading and Instrumentation for Hydrostatic Load Tests | 52 |
| 22 | Linearity of Response of Model to Intensity of Load | 54 |

## LIST OF ILLUSTRATIONS (Cont'd)


| Figure | Title | Page |
|---|---|---|
| 23 | Strain Gage Rosette Computation Form | 59 |
| 24 | Orientation of Principal Stresses | 61 |
| 25 | Distribution of Principal Stresses Due to Water Load | 65 |
| 26 | Magnitude and Direction of Principal Stresses Due to Water Load | 66 |
| 27 | Displacements Due to Water Load | 68 |
| 28 | Notation for Method of Integration for Dead Load Stresses | 76 |
| 29 | Set Up for Dead Load Tests by Method of Integration | 80 |
| 30 | Distribution of Principal Stresses Due to Dead Load | 82 |
| 31 | Magnitude and Direction of Principal Stresses Due to Dead Load | 83 |
| 32 | Principal Stresses at Base Due to Dead Load at Various Stages of Construction | 85 |
| 33 | Vertical Dead Load Stresses at Various Stages of Construction | 86 |
| 34 | Normal Stresses at Base of Dam | 87 |
| 35 | Distribution of Principal Stresses Due to Live and Dead Loads Combined | 90 |
| 36 | Magnitude and Direction of Principal Stresses Due to Live and Dead Loads Combined | 91 |
| 37 | Comparison of Stresses Determined by Elastic Arch and Experimental Analyses | 95 |
| 38 | Differential Element for Transformation of Surface Stresses | 97 |
| 39 | Normal and Shear Stresses at Elevation 450 | 99 |
| 40 | Comparison of Resultant Observed Resisting Forces with Resultant Computed Live and Dead Loads | 101 |

## LIST OF ILLUSTRATIONS (cont'd)


| Figure | Title | Page |
|---|---|---|
| 41 | Thermograms of Plaster | 112 |
| 42 | Details of Consistometer | 118 |
| 43 | Measuring Consistency of Plaster with Consistometer | 119 |
| 44 | Lightweight Aluminum Compressometer for 3- by 6-inch Plaster Cylinders | 121 |
| 45 | Typical Stress-Strain Diagram for Plaster | 122 |
| 46 | Set Up for Determining Flexural Modulus of Elasticity | 123 |
| 47 | Stress-Strain Diagrams for Three Types of Test for Modulus of Elasticity | 124 |
| 48 | Apparatus for Determining Sonic Modulus of Elasticity of a Plaster Slab | 125 |
| 49 | Effect of Water-Plaster Ratio on Elasticity of Various Celite-Plaster Mixtures | 127 |
| 50 | Variation of Water-Plaster and Celite-Plaster Ratios with Elasticity for Plasters of Constant Consistency | 129 |
| 51 | Effect of Water-Plaster Ratio on Compressive Strength | 130 |
| 52 | Relation Between Elastic Modulus and Strength of Plaster | 131 |
| 53 | Measurement of Poisson's Ratio Using SR-4 Gages | 134 |
| 54 | Complete Stress-Strain Diagrams Showing Constant Limiting Strain for a Variety of Plasters | 135 |
| 55 | Effect of Drying on Modulus of Elasticity | 136 |
| 56 | Drying Rates at Various Storage Temperatures | 138 |
| 57 | Effect of Water on Consistency and Set | 139 |
| 58 | Effect of Celite on Consistency | 140 |
| 59 | Effect of Water and Celite on Time of Set | 142 |
| 60 | Effect of Temperature on Time of Set | 143 |
| 61 | Effect of Retarder on Time of Set | 144 |

## LIST OF ILLUSTRATIONS (Cont'd)


| Figure | Title | Page |
|---|---|---|
| 62 | Effect of Retarder on Consistency | 146 |
| 63 | Time, Temperature and Volumetric Relationships During Hydration of Plaster | 149 |
| 64 | Effect of Mixing Time on Consistency and Modulus of Elasticity | 153 |
| 65 | Effect of Repeated Loading on Flexural Creep | 154 |
| 66 | Design Chart for Heavy Plaster Mixtures | 158 |

# LIST OF TABLES


| | | Page |
|---|---|---|
| 1. | Comparison of Applied and Resisting Forces | 100 |
| 2. | Physical Properties of Calcium Sulphate | 107 |
| 3. | Physical and Chemical Analyses of Gypsum Plasters | 109 |
| 4. | Ratings of Plasters | 110 |
| 5. | Physical and Chemical Analyses of Diatomaceous Earths | 115 |
| 6. | Comparison of Sonic and Static Moduli of Elasticity | 126 |
| 7. | Relation Between Tensile and Compressive Strength of Plasters | 133 |
| 8. | Consistency Characteristics | 156 |

# STRUCTURAL MODEL INVESTIGATIONS FOR OROVILLE DAM

## INTRODUCTION

### Relation of the Feather River Project to the Structural Model Investigation

The California Water Plan[1]* is a master plan to guide and coordinate the activities of all agencies of the State of California in the planning, construction, and operation of works required for the control, development, protection, conservation, distribution, and utilization of California's water resources for the benefit of all areas of the State. The Feather River Project is the first unit of the California Water Plan. Its purposes are for flood control and irrigation in the Sacramento Valley, electric power generation, and the provision of a water supply to areas of water deficiency. Oroville Dam is the key unit of the Feather River Project. Oroville Reservoir, to be created by a dam 5-1/2 miles upstream from Oroville, Butte County, California, will have a gross capacity of about 3-1/2 million acre feet at a water surface elevation of 900 feet above mean sea level, and will inundate an area of about 15, 500 acres. The average seasonal natural runoff of the Feather River at Oroville is about 4-1/2 million acre feet.

Oroville Dam, including the spillway section, will have a total length of 6, 780 feet. The dam itself will have a height of 730 feet above stream bed elevation, and will be 4, 930 feet long. The 720-foot long spillway and flood control structure will be located in a saddle on the right abutment, and will be joined to the main section by 850 feet of earth-fill. It was estimated that some 14 million cubic yards of concrete would be necessary for the gravity dam section first considered. This compares with a total volume of 10, 585, 000 cubic yards in Grand Coulee Dam, which has a reservoir capacity of 9, 402, 000 acre feet, and the 6, 230, 000 cubic yards of concrete

* Note - numbers in text correspond to numbers in list of references at end of report

in Shasta Dam, which impounds a lake of 4, 493, 000 acre feet.

Facing a construction job of this magnitude, it was decided to investigate the possibilities of a number of different types of dams having the same controlling dimensions as those of the original gravity dam, in order to determine which type would be most economical and feasible. Thus, studies were initiated for buttress dams, multiple arch dams, arch-and-buttress dams, and rock-fill dams. An example of one study of each of these types is shown in Figure 1.

Although large in magnitude, none of these designs presented particular difficulties in engineering analysis, except that of the arch and buttress design shown in Figure 1-d.

This dam is shown in more detail in Figure 2. The main structural element is a conoidal arch, with vertex upstream, and with its abutments, formed of two elements of the cone, founded on the river banks at about elevation 230. The upstream face is made plane, to receive the hydrostatic force of the reservoir. The structure is conceived as acting as a number of independent parabolic arches, receiving the water load at the crown, and carrying the load to the foundation on catenary paths which curve downstream with each successive contribution of dead weight in the arch. A gravity plug replaces the vertex of the cone to avoid the large stress concentrations in this region, and to act as a cofferdam during construction.

Part of the water load in the vicinity of the arch is first taken on a massive-head buttress that in turn transmits its load downward through the flank of the arch to a common foundation. The remainder of the water barrier on each side of the main arch section is made up of independent massive-head buttresses at 130 ft. centers, with 50 ft. thick walls.

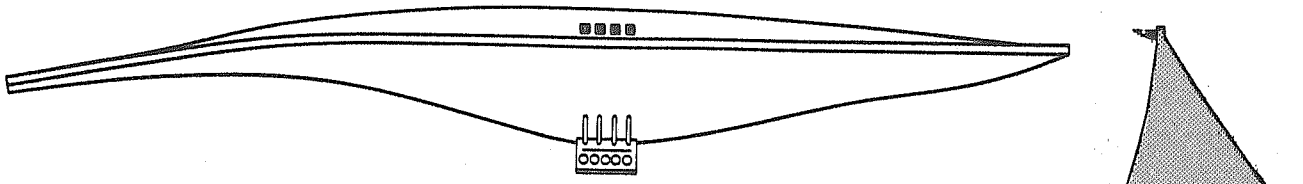

A - GRAVITY DAM

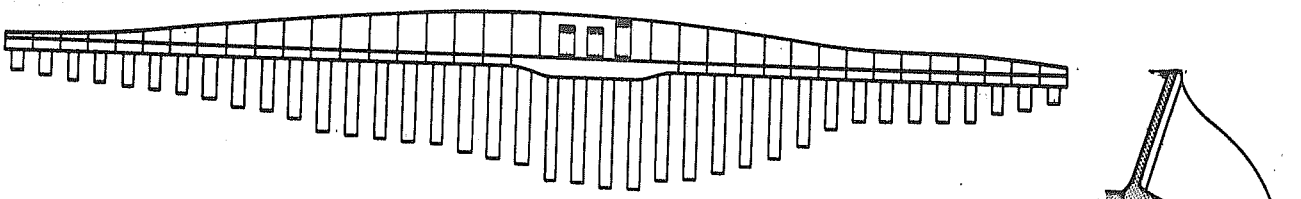

B - BUTTRESS DAM

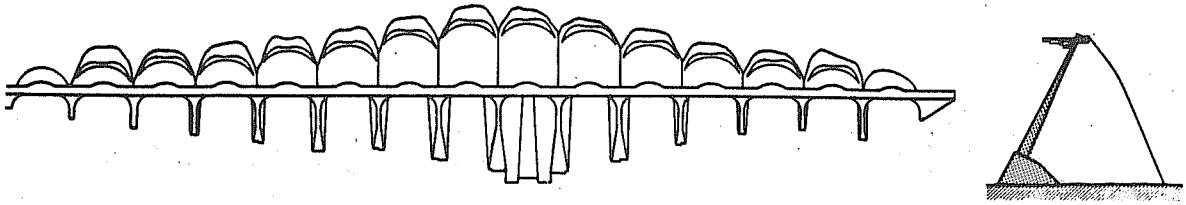

C - MULTIPLE ARCH DAM

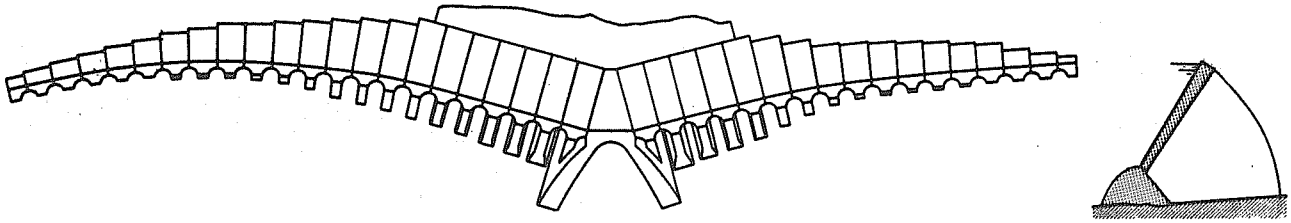

D - ARCH AND BUTTRESS DAM

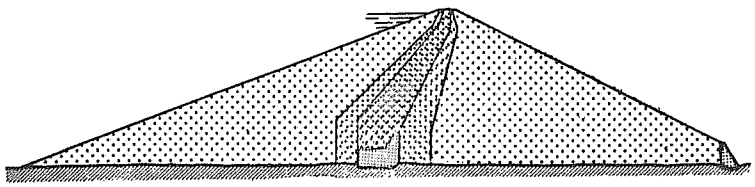

E - ROCKFILL DAM

FIGURE 1 - TYPES OF DAMS CONSIDERED FOR OROVILLE DAM

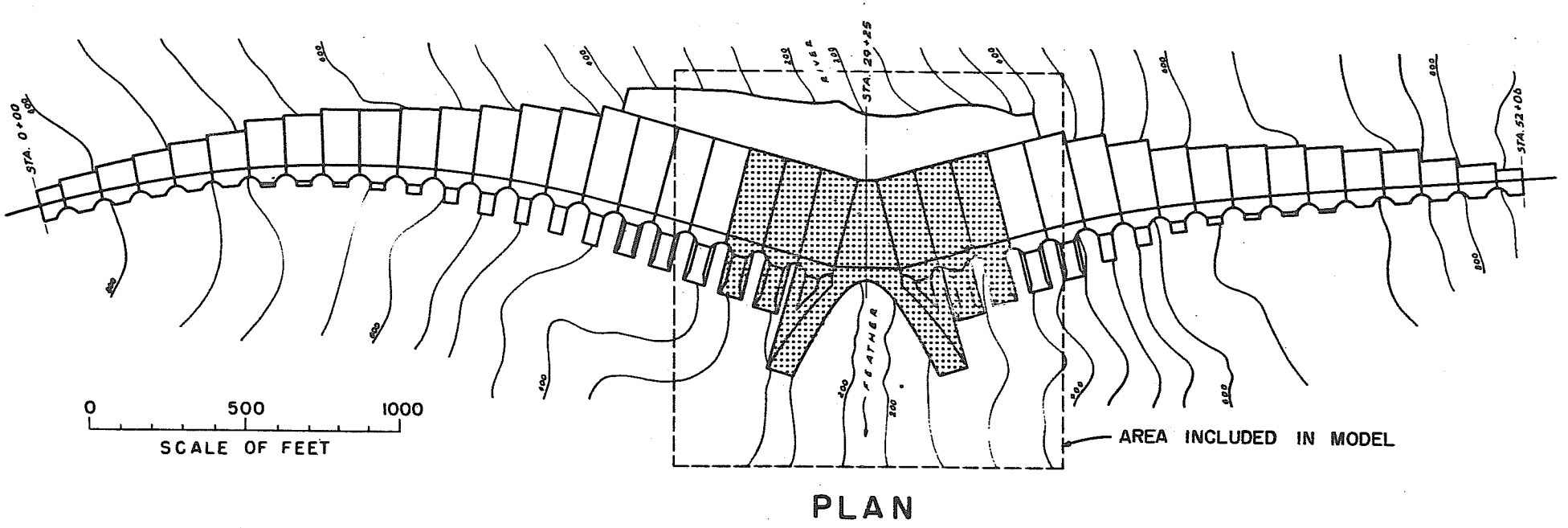


PLAN

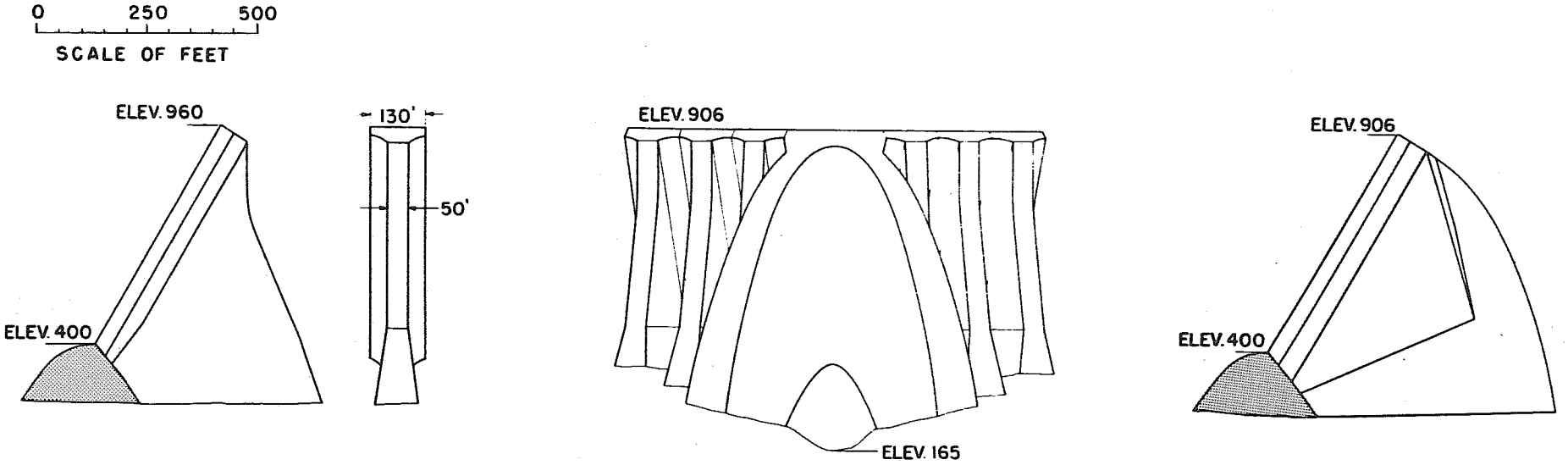


TYPICAL BUTTRESS

DOWNSTREAM ELEVATION

ARCH EXTRADOS

FIGURE 2 - THE OROVILLE ARCH AND BUTTRESS DAM

Such serious questions were raised as to the interaction of the arch and the buttress elements in this design, that it was decided to supplement the analytical studies of this dam with an experimental structural study of a reduced scale model of the dam in order to determine its stresses under dead and live loads. Accordingly, a service agreement was entered into between the Department of Water Resources of the State of California and the Institute of Engineering Research of the University of California at Berkeley on June 17, 1957, wherein the University was asked to conduct an experimental research project on the structural behavior of an arch and buttress dam under water load and dead load. Work began on this project as soon as authorized, and all experimental work and data reduction was completed by November 1958.

As a part of the experimental studies, work was also done on photoelastic models of the cross section of a power plant to be contained within the core wall of the proposed earth and rock filled dam. The photoelastic study of the core wall power plant is reported in "Photoelastic Analysis of the Concrete Core Block for Oroville Dam", Progress Report, March 1958, by Professor H. D. Eberhart.

Previous Reports

During the progress of the model tests, four reports were submitted documenting the progress of the work. These comprised:

1. Raphael, J. M., Progress Report - Oroville Dam Model Tests, University of California, Engineering Materials Laboratory, June 13, 1957

2. Raphael, J. M., Progress Report - Oroville Dam Model Studies, University of California, Engineering Materials Laboratory, July 15, 1958

3. Raphael, J. M., Feasibility Report - Determination of Dead Load Stresses, Oroville Dam, University of California, Engineering Materials Laboratory, July 17, 1958

4. Raphael, J. M., Progress Report - Oroville Dam Model Studies, University of California, Engineering Materials Laboratory, November 12, 1958

The material contained in the four reports previously submitted has been incorporated into this final report, which supersedes all previous reports on the Oroville Dam Model Studies.

Acknowledgment

The Oroville Dam Model Investigations were carried out under the terms of California Standard Service Agreement No. 57-SA-100 between the California Department of Water Resources, and the Institute of Engineering Research of the University of California. For the Department of Water Resources: Harver O. Banks was Director; Walter G. Schulz was Chief Engineer; Donald P. Thayer was Assistant Division Engineer, in direct charge of the design studies for the dam, assisted by Engineers Gordon W. Dukleth, Ed Stroppini, and James J. Doody. The Board of Consultants who considered the results of these investigations consisted of Raymond A. Hill, Chairman; John J. Hammond, Roger Rhoades, Byram W. Steele, and B. E. Torpen. In addition to Professor Jerome M. Raphael, in direct charge of the investigation at the University of California Engineering Materials Laboratory, Faculty Investigators who contributed greatly to the success of the investigation were Professors Howard D. Eberhart, David Pirtz, and Egor P. Popov. The members of the staff of the investigation were Associate Research Engineer Stuart N. Bartholomew; Assistant Engineer Edward L. Wilson; Junior Engineers G. L. Croy, V. K. Sondhi, A. T. Stover, and Y. Yoshikawa; Research Assistant S. Kokusho; Senior Engineering Aids Y. Katsura, J. L. Hemmer, and the late W. R. DeBoer; Engineering Aides W. Hayes, W. Rous, A. Bulow, R. W. Thomas; and

Electronics Technician G. L. Wilson. Members of the laboratory staff who contributed to the investigations were E. Brown, E. L. Whittier, A. Klein, L. Trescony, G. Hayler, N. Haavik, and H. Williams. Special thanks are given to Consulting Chemist Wallace C. Riddell, who contributed much of his knowledge of the technology of plaster. During the course of the investigation the project was visited by A. Coyne, Inspector General and Consulting Engineer, Paris, France; Professor G. Oberti of Istituto Sperimentale Modelli e Strutture, Bergamo, Italy; J. L. Serafim of Laboratorio Nacional de Engenharia Civil, Lisboa, Portugal; and Professor Y. Niwa of the Engineering Research Institute of Kyoto University, Kyoto, Japan whose helpful suggestions are gratefully acknowledged.

# PRELIMINARY CONSIDERATIONS

## General Assumptions and Requirements

The purpose of a structural model test is to predict the structural behavior of the prototype. This prediction is possible only when the model satisfies the three similitude requirements of scale, loading, and material properties. The scale requirement is met when the model is geometrically similar to the prototype. The type of loading must be similar to the type experienced by the prototype, and must be proportional in magnitude. The stress-strain properties of the model material must be similar to those of the prototype material within the stress range of the test. It would be ideal if all three similitude requirements could be met simultaneously and in all respects in a structural model test, but practical considerations may involve some approximations to these ideal conditions. For the Oroville Dam model tests, the most important approximations that were made involved:

a. The proportionality of strain to loading,

b. The relative stiffness of structure and foundation material,

c. The depth and area of model foundation,

d. The interaction of structural components,

e. The area of hydrostatic loading, and

f. The sequence of prototype construction.

These assumptions are discussed in detail in the following sections, together with their effect on the accuracy of the test results.

Proportionality of Strain to Loading

In concrete dams, the dead load increases gradually as the dam is constructed, and then remains in place, while the live load due to the reservoir may come and go. In models, dead loads do not produce measurable strains, so that it is necessary to perform special tests for the effect of dead loads. Thus it is desirable to test separately for the effects of dead and live loads in model dams. The total effect of live and dead load can be found by superposing the results of the separate tests. This superposition of stresses is possible only if the strains are a function of the load and are not affected by the deformation of the structure. If the structure is of such a nature that it deforms as it is loaded to the extent that a secondary system of stresses is set up, then direct superposition of stresses is not possible. Preliminary analysis of one of the inclined arch rings of the conoidal arch indicated that deformations due to load would be so small that such secondary strains could be neglected. However, the hydrostatic loading system was designed so that strains could be determined at a number of intensities of loading, to check the linear strain behavior of the model with load.

Relative Size of Model and Foundation

An important factor in deciding how large to make a foundation for the model is the effect of foundation deformations on strains in the arch dam. Arches are quite sensitive to abutment movements.

Since each separate buttress causes its own foundation deformations, it was necessary to include, in addition to the central arch of the dam, a number of adjacent buttresses in order to load the foundation of the model in much the same manner as would be the foundation for the prototype dam. In designing the foundation for the model, it was considered that by

making it wide enough to include the local deformations caused by two adjacent buttresses on each side of the main arch, the foundation deformations in the model would be similar to those of the prototype. However, as an extra precaution, the foundation was made wide enough to include a third buttress on each side of the central arch if it were found necessary.

The depth of the foundation was determined as a compromise between two opposing requirements. A load on the surface of a semi-infinite body such as the foundation of a dam causes unit deformation in that foundation of a decreasing magnitude with increasing depth from the point of application of the load. Total deformation at the surface is the integrated result of all the unit deformations from the surface downward. Thus, the more of the foundation that is included in the model, the more truly the local deformations at the surface reflect those in the prototype. However, constructing the foundation of a model is the most time-consuming element of the whole project, as each layer of the foundation has to be completely cured before the next layer can be constructed. Thus, the greater the thickness of foundation that is chosen, the longer time that will elapse before the model dam can be constructed and tested.

Boussinesq's solution to the foundation problem was used as an aid to determine the optimum depth of foundation. The arch and buttresses were assumed to form a continuous structure carrying a normal water load. Foundation stresses at various distances from the base of this continuous structure were computed using the Boussinesq's equations. It was concluded that although some error might be entailed if the depth

of the foundation was made about equal to the average width of the loaded strip, very little improvement would be found if the foundation was made say twice as deep. Accordingly, the boundaries of the model foundation were established at 400 feet (prototype measurement) below the base of the dam and 300 feet upstream of the dam.

Relative Stiffness of Dam and Foundation

Since the stresses in the model are modified by the relative stiffness of the dam and foundation, it was decided to make the model dam and foundation of materials having values of modulus of elasticity proportional to those of the concrete and rock of the prototype. The amphibolite rock of the Oroville Dam foundation had been tested by coring and by seismic methods. The cores had very high moduli of elasticity, averaging 16 million psi. These values were largely discounted as they represent only the best portions of the foundation, and do not reflect the effect of discontinuities suchas cracks and seams. The foundation in place had been evaluated by seismic test, which related the velocity of sound passing through various portions of the foundation and the average density of the foundation to the elastic modulus. Results of these experiments ranged from 6 to 15 million psi, and indicated that the average modulus of elasticity of the foundation in place was about 8 million psi.

From the strength requirements for the mass concrete for the dam, and from available information on the elastic modulus of mass concrete at the age of one year, it was estimated that the elastic modulus of the mass concrete would be 6 million psi. Considering the age of the concrete when the dam first receives its important loads, it was then

estimated that the effect of creep could be approximated by using an elastic modulus for the mass concrete of 4 million psi. In a similar manner, it was estimated that the elastic modulus for the plug would be approximately 2 million psi.

Considering these requirements together, it was then stipulated that the elastic moduli of the foundation rock, the main dam, and the plug should be in the proportion 4:2:1.

Interaction of Structural Components

In working at model scale, some latitude must be taken in setting boundary conditions. Difficult problems arise considering the interaction of the components of a structure as complex as the arch and buttress dam tested. In the prototype, the joints between adjacent buttresses were to be cushioned with a substantial rubber bearing block, but otherwise left free. In the model, these joints were made completely free. In the prototype, the joint between the arch and the plug was to be filled with a mastic material to prevent bond. It was considered that the enormous weight of the dam combined with creep of concrete would actually cause considerable transfer of compressive stress across this mastic joint, so that any evidence of tension due to water loads would only decrease existing compression from dead loads, and that the action of this joint could best be expressed in the model by bonding the dam to the plug. Due to the positioning of the rubber waterstop in the joints, some hydrostatic forces can exist in the joints of the prototype, but this was completely ignored in the model.

Area of Hydrostatic Loading

In the prototype, the reservoir load is transmitted not only to the

dam structure, but also to a large portion of the reservoir floor itself. These loads deform the crust of the earth itself not only in the vicinity of the reservoir, but for some distance outside it. Thus, very careful measurements[7] showed that Lake Mead deformed the crust of the earth by 7 inches at its center of weight and by some 5 inches near Hoover Dam itself. However, this deformation is spread over a tremendous area so that the differential deformations in any local area represented by a portion of a dam are slight. Because of the practical limits of the model foundation, it was impossible to reproduce the prototype loading in its entirety. Stresses in the arch are produced by loads directly on the arch and by differential foundation movements. Since most of the differential foundation deformations are produced by loads in the immediate vicinity of the arch, the area to be loaded hydrostatically was selected as the arch section, the gravity plug, and the two buttresses on each side of the arch section.

In order to check the magnitude of the effect of adjacent buttress loads on the stresses in the arch, the arch section was loaded independently of the buttresses as a part of the testing program. Results of this test indicated that the effect of loading on buttresses and plug was small; therefore, the selected loaded area appeared to be sufficiently large.

Method of Prototype Construction

The method of construction of a prototype dam has a considerable effect on the distribution of dead load stresses in the structure. For instance, in a dam constructed as a series of vertical columns, the dead load stresses at the base of each column will be representative of the

weight of the concrete directly above that spot; whereas in a dam constructed in a succession of horizontal lifts extending clear across the cross section of the dam, the dead load stresses will be distributed more or less in accordance with elastic theory, as was shown in the investigation of the structural behavior of Shasta Dam.[8] For the dead load tests of the Oroville model, it was assumed that the dam was to be constructed in horizontal layers from one end of the arch to the other. Accordingly, the dead load stresses were determined by a step-by-step method based on this construction sequence.

# CONSTRUCTION OF THE MODEL

## Selection of Material and Scale

Scale and material for the model cannot be selected independently, for they are mutually interdependent factors. While there is wide selection for the type of material to be used in a two-dimensional model, the three-dimensional highly indeterminate structure that was the prototype for Oroville Dam made it necessary to use a material having a Poisson's ratio close to that of concrete or rock. Two classes of material fell into this category: plasters and cement mortars. Of the two, it was felt that plasters offered the greatest opportunity for model manufacture due to its ease of molding, and to the relative facility with which it could be worked subsequent to molding.

Two methods have been used for modeling dams in plaster: the first is to cast the dam between molds to the desired shape; the second is to cast an oversized block, which is subsequently machined to final shape. Considering the intricate shape involved, it was decided to cast the dam to final shape, for the most part, except for some minor details which were to be precast and bonded for the final assembly.

As can be seen by an inspection of equation (6) which gives the conditions of similitude for strain, scale and elastic modulus of a model are interdependent: for the same intensity of loading, the same strains can be found with a large model having a high modulus of elasticity as with a small model having a low modulus of elasticity. After deciding to cast the model to final shape, the scale was fixed at 1:200 as offering the greatest possibility of accuracy in construction. It was desired to build

a model large enough so that small inaccuracies in molding or in affixing strain gages would have negligible effect on overall accuracy of the tests. It was considered that the model should have a maximum strain of 500 microinches per inch at maximum load in order that reading errors of no more than 2 percent would be found with a test set capable of reading strains to 10 microinches per inch. It was further considered that the model would be loaded with mercury or by some means giving a load equivalent to that of mercury. Considering scale, loading, maximum strain, and the modulus of the prototype concrete simultaneously, design value of the elastic modulus of the model material was set at 240,000 psi. Considering the elastic moduli of the concrete in the dam and the rock forming the foundation of the prototype, the design values of the elastic modulus for the foundation of the model was set at 480,000 psi and for the plug of the model at 120,000 psi. These then set the general requirements for the construction of the model.

In the section that follows, the actual methods used in constructing the model will be given in detail. The actual research leading to the formulation and control of the plaster-celite mix used in constructing the model is given in detail in the Appendix.

General Scheme of Construction

Having decided to cast the model to final dimension, there still remained the question of the construction of the molds. Working with student help, rather than with skilled pattern makers, it was necessary to choose a scheme for construction of the molds that could be handled simply. It was decided to make closely controlled prototype models to the exact dimension of the final structural model design, construct molds

around this prototype model, and pour the final structural model in this mold. This scheme, using fiberglas molds, worked out very easily, and is highly recommended for model making.

Construction of Base Mold

The prototype for the base was constructed of three-quarter inch waterproof fir plywood templates screwed and glued to a 2" by 12" fir frame, as shown in Figure 3A. This gave a guide line at every 12.5 foot contour, between which the ground surface was molded by hand in plaster. The surface of the templates was waterproofed with shellac, and a number of copper tacks were partially driven into the wood to help anchor the plaster.

Two bond breaking agents were then applied to the surface. First the smooth surface was rubbed with two coats of a mold-release wax, rubbing again between coats. A thin film of mold-release liquid, which is a water soluble cellophane, was sprayed on top of the wax.

Activated polyester resin was then brushed onto the surface, reinforced with alayer of 2 oz. fiberglas C-cloth. The thickness of the mold was then built up by applying another layer of resin reinforced with 6 oz. reinforcing mat. which was a fiberglas felt. Over this was laid another layer of resin and C-cloth, brushed out with a thin layer of resin. By this means, the thickness of the mold was built up to about 3/8 inch.

The mold which would have had a certain amount of stiffness due to its doubly-curved shape, was made still stiffer by adding a network of ribs or stiffeners, as shown in Figure 3B. These were made by fitting one-quarter inch by two-inch balsa ribs to the surface, and overlaying these with fiberglas and resin. The result was a strong, lightweight

A - ASSEMBLED PLYWOOD TEMPLETS ON FRAME

B - FITTING BALSA STIFFENER CORES ON FIBERGLAS MOLD

C - THE COMPLETED MOLD

FIGURE 3 - STEPS IN CONSTRUCTION OF FOUNDATION MOLD

mold able to resist the hydrostatic force of plaster poured beneath it without appreciable distortion.

The hardening process of the polyester resin is interesting. The resin is made by distilling together orthothallic acid, alkyd resins, and a styrene monomer. Five percent of Cabosil, or activated calcium silicate, is added to the resin as a thixotropic agent, or thickener, to prevent the resin from running off inclined and vertical surfaces. The polyester resin is a thermosetting plastic, and heat is needed to start the cross linkage that gives the plastic its hardness and strength. This heat is supplied by two agents which combine in an exothermic reaction. One of these agents is an additional two percent of cobalt naphthenate which is added to the resin. The other agent is methyl-ethyl-ketone peroxide which is carried separately in di-allyl-thalate solution, termed the catalyst. As long as resin and catalyst are kept separate, the materials are inert and can be stored for long periods. When resin and catalyst are combined, an exothermic reaction begins, the heat of which causes a molecular cross linkage during which the resin changes from a liquid to a solid polyester which binds to the fibrous glass. At the same time, a styrene monomer and a small amount of free hydrogen is given off creating a distinct odor.

During curing, 6 percent shrinkage takes place, but this interestingly enough is all directed toward the surface on which the fiberglas is laid, with no volume changes taking place parallel to this surface. Since all that is desired is that the molded surface remain true, the shrinkage does not affect at all the proportions of the mold, and the mold remains true to its shape.

The Plug Mold

Control for forming the plug was achieved by making a framework of 1/4 inch waterproof plywood, shown in Figure 4A. This was fitted in place onto the foundation prototype, and filled with plaster as shown in Figure 4B. Square openings and extra material were added at the crest so that the resulting mold could be filled to excess to aid removal of any bubbles that might form on the top horizontal surface. The mold was quite stiff, but a few stiffeners were added as and extra precaution. By forming the mold directly in place on the foundation, perfect register was achieved between the plug mold and the poured foundation, as can be seen in Figure 4C.

The Main Arch Mold

Steps in the construction of the mold for the main arch are shown in Figure 5. Templates for controlling the shape of the arch were cut from 0.080 inch aluminum alloy sheet for every 50 foot elevation actual size, or three inches in the model. These were held to exact spacing by short metal cylinders and long bolts. After the templates had been assembled and aligned carefully, most of the space between the templates was filled with burlap which had been dipped in plaster. The remaining space was filled with plaster, carefully finished by hand to the desired shape. The whole sub-assembly was then moved onto the prototype foundation, carefully located, and the lines of the dam faired into the foundation.

Automobile body finishing techniques were used to achieve a smooth finish to the arch prototype. Several coats of automotive lacquer were sprayed on the surface, and rubbed down by hand. The edges were trued with automotive putty, and sanded smooth. Although this gave a

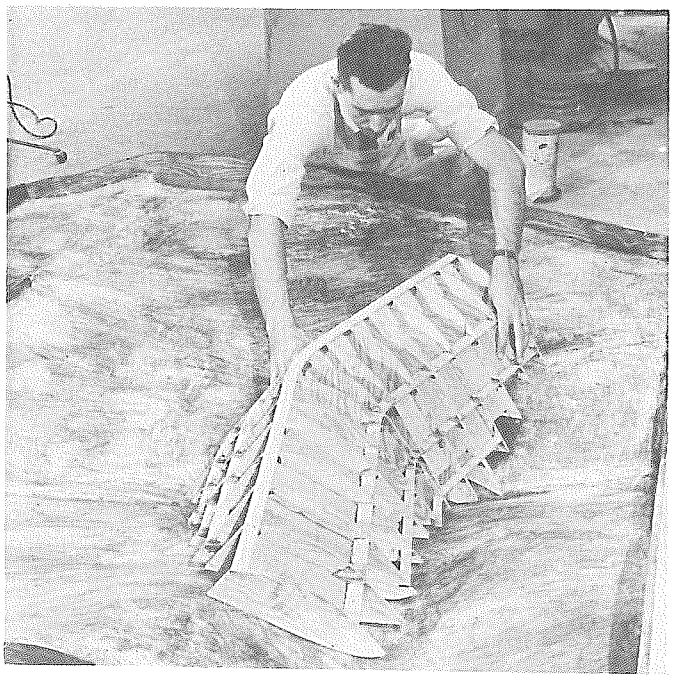

A - FRAMEWORK OF PLYWOOD TEMPLETS CONTROLS SHAPE OF PLUG

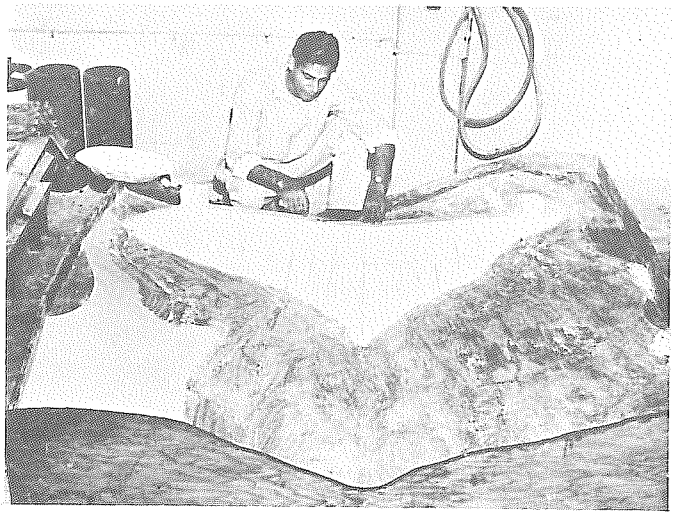

B - THE COMPLETED PROTOTYPE PLUG IN PLACE ON PROTOTYPE FOUNDATION SURFACED WITH PLASTER, WITH SPRUES ADDED

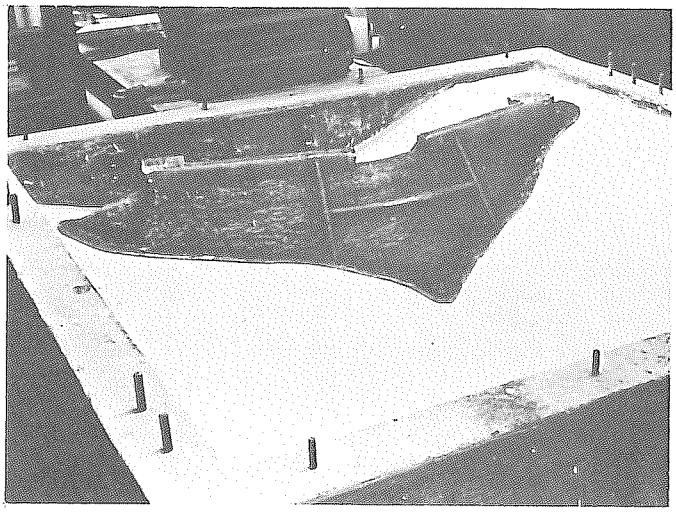

C - THE COMPLETED FIBERGLAS PLUG MOLD, IN PLACE ON THE POURED FOUNDATION, SHOWING PERFECT REGISTER

FIGURE 4 - STEPS IN CONSTRUCTION OF PLUG MOLD

mottled appearance to the model, its surfaces were true and smooth, and the resulting mold and model reflected the care taken at this stage.

The arch mold was made in six pieces to aid its removal from the poured model. One was the upstream face, one was the downstream face under the arch, two formed the side faces, and two formed the curving ends of the arch.

It was thus necessary to form flanges on the various pieces so that they could be reassembled accurately. For this purpose, sheet metal plates were fitted to the upstream and downstream faces of the two outstanding legs of the arch. The fiberglas was then applied to the side faces, and lapped onto the sheet metal "dams", to form the flanges. It had at first been feared that it would be difficult to apply the fiberglas under the arch of the intrados, but the thixotropic properties of the polyester resin prevented the fiberglass from running off, and the reinforcement stuck just like wall paper. In addition to the usual stiffeners on the mold parts to prevent local distortion, removable angle iron braces were fiberglassed into the intradosal form to maintain dimension between the outstanding legs of the arch. After the metal plates had served their purpose, they were removed, and the upstream and downstream faces too were fiberglassed. When all surfaces had been covered with the reinforced laminate, all flanges were drilled through every three inches for small machine bolts, before removal from the prototype. The form was thus matched for perfect register in reassembly.

Buttresses

The prototypes for the buttress molds were constructed of a variety of materials. The main part of the buttress was constructed of plywood,

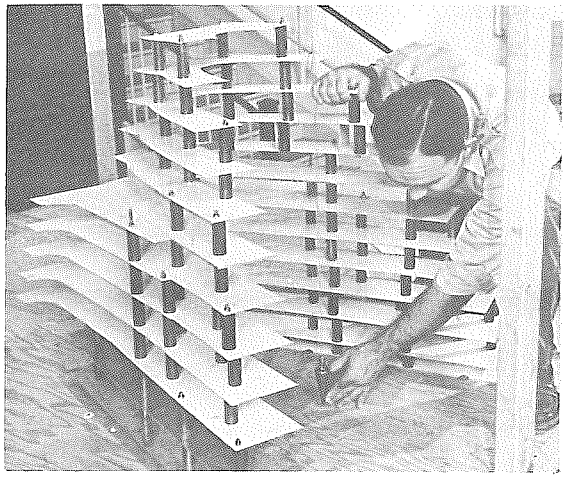

A - CONSTRUCTING TEMPLET

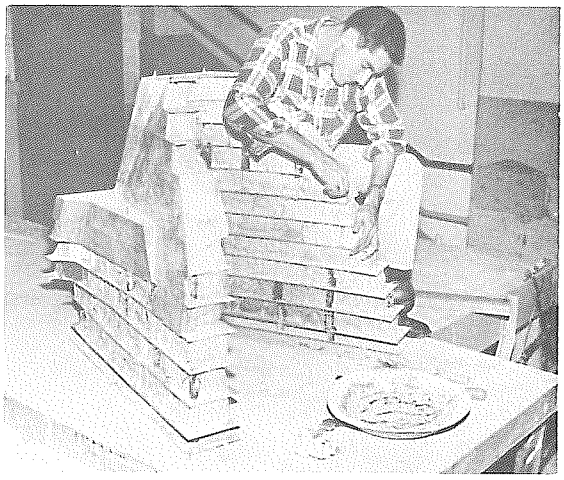

B - PLASTERING TEMPLET

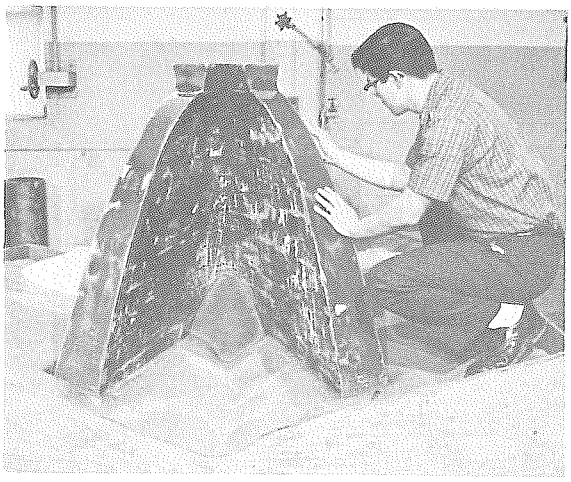

C - FINISHING PROTOTYPE

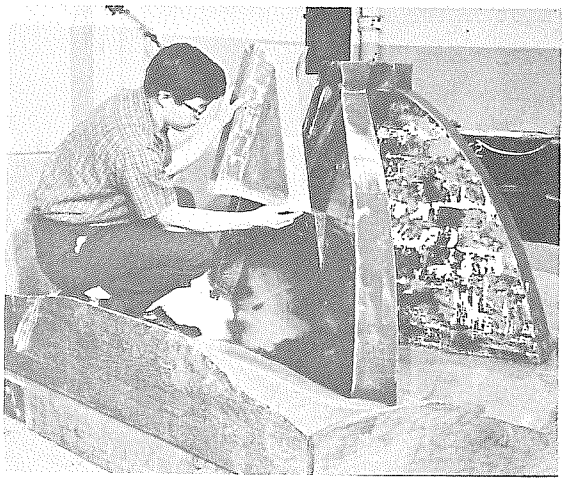

D - FITTING RIDING BUTTRESS

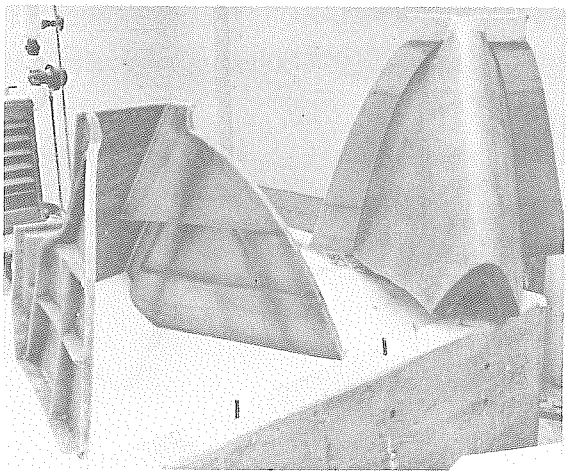

E - FIBERGLAS MOLDS EXPLODED

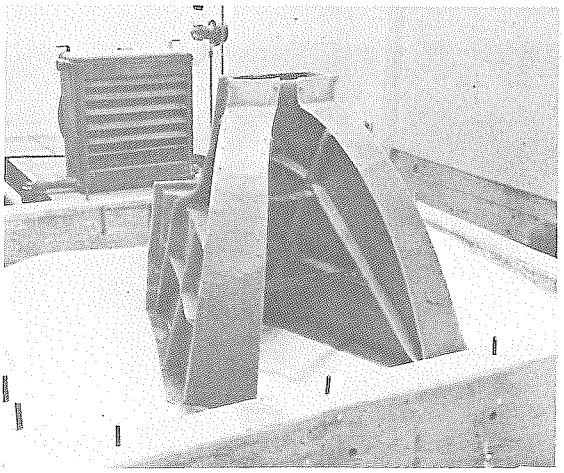

F - FIBERGLAS MOLD IN PLACE

FIGURE 5 - STEPS IN CONSTRUCTION OF MAIN ARCH MOLD

nailed and glued to a wooden frame. The buttress head was a solid piece of fir. The fillet between the buttress head and the buttress was made of plaster, with the curve controlled by short templates of No. 12 AWG aluminum alloy. The flared portion of the buttress again was plaster screeded between plywood templates. This illustrates the ease with which the prototypes for fiberglas molds can be made. It is important only to produce a surface on which the polyester resin can be applied. In the mold itself, since some of the surfaces are plane, or are easily adaptable to sheet metal, fairly stiff pieces of sheet metal were applied directly to the prototype to form part of the mold. Where the surfaces were more intricately shaped, fiberglas was used and lapped directly to the sheet metal. By drilling bolt holes between the lapped portions before the mold was disassembled, perfect register could be obtained upon reassembly.

Two buttress molds were made: one for the riding buttress that faired into the flanks of the main arch; and one for the full buttress. As shown in Figure 5C, the riding buttress rested on a plane surface at elevation 600. The two riding buttresses were cast identically, and then cut away by hand to fit against the extradosal flank of the arch. Similarly, all full buttresses were cast identically, and then hand fitted onto their respective foundations.

The Testing Pit

A reinforced concrete testing pit, 8 feet square by 4 feet high with 6 inch walls and base, was cast on 3/4" plywood sheets laid on the floor of a room having fairly stable humidity and temperature conditions. A light plywood shelter was erected on top of this pit, and an industrial

space heater fitted at one end with thermostatic control, so that hot air could be circulated over the model to dry out excess water. In addition, for the first poured foundation, thermostatically controlled copper heating coils were spaced throughout the base through which hot water from the building's hot water lines could be circulated to increase the thermal activity in the plaster base. The walls of the pit were fitted with a large number of conduits for taking tubes and conductors through the walls. Although this construction had ample strength for the tests, it deformed to such an extent under load that deformation measuring equipment could not be connected to the walls. In future testing, a more massive testing pit should be installed.

Method of Pouring Plaster

The largest batches of plaster that were poured at any one time had a volume of 8 cubic feet. The men and equipment had to be well organized to produce this much plaster to an exact strength specification. Ten 5-cubic foot aluminum bread mixers were placed in pairs, five of them filled with the measured quantity of water and celite, and the other five filled with the required amount of molding plaster. After having soaked the celite until all bubbles had been removed, the plaster was added to the water at a given signal. Plaster then dissolved into the water , and the lumps were removed by a steady paddling over a period of about 15 minutes. At this time, the individual batches were poured through a seive into a 15 cubic foot tank where they were further blended by paddling. This tank was then lifted by a chain hoist to an elevation above the mold to be filled. When the control pats indicated that the plaster was nearing the time of set, a quick-acting valve at the bottom

of the tank was opened, and the fluid plaster flowed by gravity through a 3-inch fire hose into the mold, filling all parts. At the same time, control cylinder and beam molds were filled as a check on the properties of the plaster. With careful control, the plaster usually set within two minutes after pouring had been completed. If the plaster were poured too soon, it had a tendency to bleed, and hence very careful control was necessary in order to pour at the last possible minute. Once the plaster had attained sufficient strength, the mold was removed, a plywood shelter placed on top of the testing pit, and drying commenced, to continue until all possible excess moisture had been removed from the lift.

Methods for Construction of Foundation

Two methods were used for constructing the foundation for the model. The first foundation was poured in place in layers under the fiberglas mold. When this proved unsatisfactory, it was demolished, and a second foundation assembled out of large prefabricated plaster blocks.

The foundation of the Oroville Dam model had a volume of 90 cubic feet, and a maximum thickness of 30 inches. If this volume had been poured at one time, it would have taken years to dry it to the point of uniform moisture content where it would be truly homogeneous and isotropic. Hence, it was poured in 3 inch thick layers, each layer dried to zero free moisture content, and the surface sealed before the next layer was poured. It was estimated that it would take approximately two weeks to dry out a 3 inch thick layer from the top surface.

If each layer were poured horizontally, a feather edge would result where the horizontal lift line encountered the sloping abutment surfaces.

The result would be a series of weak points in the foundation, and a procedure was devised to eliminate these feather edges. As shown in Figure 6, each layer was poured under the foundation mold, so that although uniformly thick, each layer undulated following the contours of the foundation. After pouring the first wedge-shaped portions of the foundation, the mold was supported the proper height above the free surface, the plaster poured in at one side flowing through the bottom of the mold

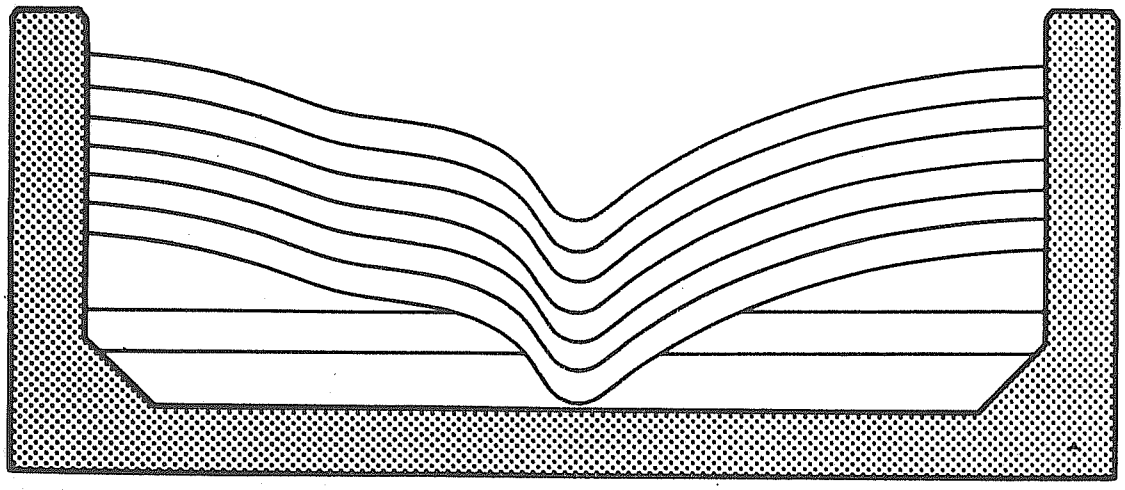

FIGURE 6 - CONSTRUCTION OF LAYERED FOUNDATION

and up the other side, filling the mold completely with no trouble. After the usual period of drying, the process was repeated until the correct thickness of the foundation had been built up.

After the model had been completed and loaded, it was noticed that even though the structure and the loading was symmetrical, the structure

was behaving decidedly unsymmetrically. By a series of sonic tests and bearing tests, it was shown that the layers of the foundation were out of contact at every convexity of the foundation. Evidently, the delayed expansion of the plaster, which occurs after it has attained its strength, had been confined within the limits of the testing pit walls. Where the foundation bulged inwardly, this expansion merely caused the plaster layer to press more firmly onto the layer below. However, where the foundation bulged outwardly, the expansion caused the layer of plaster to rise slightly away from the previous layer. Thus, when the model was loaded, the foundation acted as a sort of leaf spring, giving a variable resistance to deformation. This behavior was completely unsatisfactory, the model was removed, and the foundation was demolished.

With very little time left, a method had to be devised to replace the foundation quickly, and with uniform material. This was done by completely prefabricating the foundation of a series of standard 20 x 30 x 4 inch plaster slabs. These were made accurately in a mold, dried in an oven at 130°F to constant weight, and tested for sonic modulus of elasticity before installation in the foundation. A 3 inch base of plaster was cast in place in the foundation, screeded between 2 x 2 inch wood strips, which were carefully leveled in place. The standard blocks were then fitted and bonded into place on the foundation, using an epoxy adhesive for bonding the joints. Vertical joints were staggered as shown in Figure 7 in a pattern devised so that no two vertical joints occurred in the same plane. The blocks for the actual ground surface were cast on the foundation mold, disassembled, dried in the ovens, and reassembled on the foundation with very little trouble. The whole process of demolishing the previous foundation, manufacturing and drying the blocks

fairly bulky mass required six weeks for drying out completely.

While the plug was drying, four complete buttresses, and two riding buttresses were cast and dried in the ovens. Upon completion of the plug and while it was still drying, the mold for the main arch was assembled in place, as shown in Figure 5F, and the arch poured in place on the foundation. Drying the main arch took about two weeks. Next the prefabricated riding buttresses were carved to fit in place on the arch and bonded in place using epoxy adhesive. Finally, the independent free standing buttresses were fitted to the foundation and they, too, were bonded to the foundation using epoxy adhesive. Figure 8 shows the model as completed, before testing, but with some of the strain gage rosettes cemented in place.

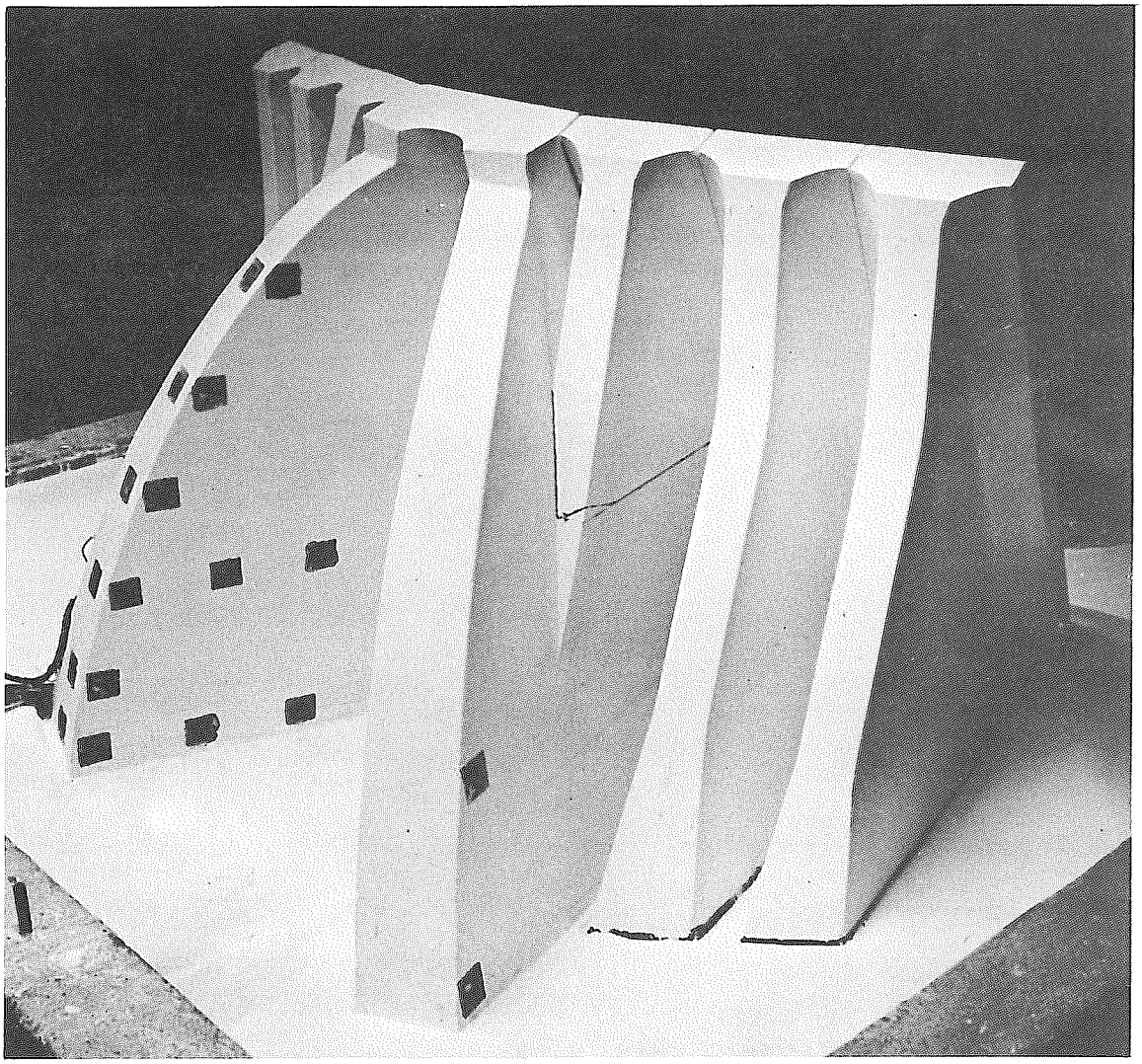

FIGURE 8 - THE COMPLETE MODEL BEING FITTED WITH STRAIN GAGES

# TEST EQUIPMENT AND PROCEDURES

## Hydrostatic Loading System

Four systems of loading were considered for the model: hydraulic jacks, mercury loading, water loading, and pneumatic loading.

Although hydraulic jacks offer great versatility in controlling the magnitude of the load, the concentration of the loads must be carefully dissipated in order to simulate the effect of the distributed loading in the actual protoytpe dam. In addition, a large number of jacks must be used in order to carry loads to all parts of the model at the varying magnitudes needed. The cost and the time necessary to manufacture a large number of jacks, together with the associated control equipment and piping, caused this method to be discarded.

Mercury loading had been used in a large number of model tests, because the loading resembles that of water, and because its high density causes strains in the model of large enough magnitude to be easily detected with the strain-measuring equipment. However, mercury loading can give only one magnitude of load, and the linearity of the strain cannot be checked against intensity of loading. Mercury is a potent industrial health hazard, and the conditions imposed for its use in testing caused search for still another method.

Water load had been used in previous tests by Pirtz[9] on a rock-filled dam, using a boom to control the head on a series of independent water bags pressing on the upstream face of a dam, so that the normal hydrostatic pressure of water could be greatly intensified. However, this scheme could not be used directly with a plaster model, since any leakage in the water bags would be absorbed immediately by the plaster, changing

its elastic properties. Hence, a modification of this idea was made.

The pneumatic loading device shown schematically in Figure 9 was used for the live loads on the Oroville Dam model. The dam is loaded by air in horizontal bags, each covering a vertical height of 50 feet in actual dimension, or 3 inches in model dimension. Thus, the uniformly increasing pressure variation due to hydrostatic loading is replaced by a uniformly stepped load. The differential pressure controller shown in the figure was devised so that the pressures in all bags could be maintained at a constant relation, without the necessity for separate control at each bag. Figure 10 shows how the uniformly increasing hydrostatic pressure having relative values of 0, 1, 2, 3, 4, at each even control elevation is replaced by an

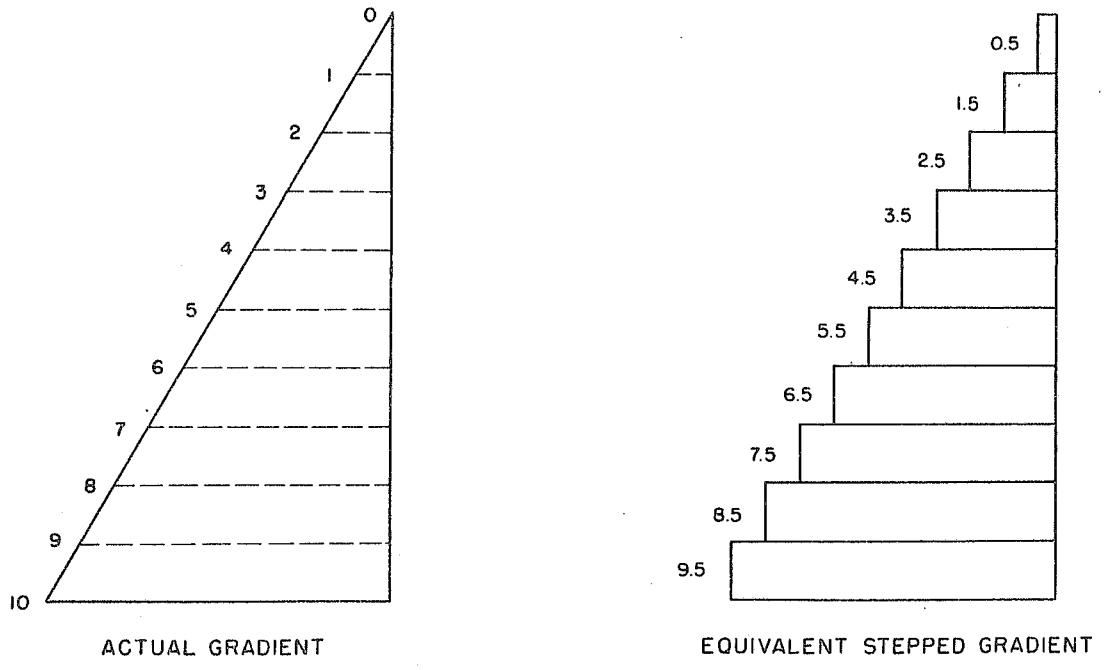


FIGURE 10 - ACTUAL HYDROSTATIC PRESSURE GRADIENT AND EQUIVALENT STEPPED GRADIENT

equivalent series of steps having average values of 0.5, 1.5, 2.5, 3.5... Thus, the top bag differs from atmospheric pressure by 0.5, and all succeeding bags differ from each other by the value of 1.

The differential pressure controller consists of a series of sealed plastic columns, connected in series by rubber tubes, and each filled to a constant head except the last which is filled with 1/2 head. Air is bubbled through the entire series of water columns, escaping to the atmosphere through the half water column. The supply pressure is immaterial, except that it has to be enough to overcome the pressure of the entire series of water columns. It can be seen that the air pressure above any two adjacent water columns will differ by the head in the column, and that the pressure in the next to the last column will differ from atmospheric by one half the head. Thus, the conditions have been set up as required in the problem.

The air pressure at the top of each column is led to a corresponding air bag, and in turn a tube at the far end of each air bag leads to a mercury manometer where the pressures in the individual air bags can be checked. The controller acts exactly the same as that of a single high column of water wherein the pressure is tapped off at equal increments. The relative height of this water column can be changed quickly by mounting all water columns on a single tilting table, and varying its inclination. Since the head depends only on the vertical height between the top of the water column and the air inlet, control of the intensity of pressure is easily accomplished.

The tilting table is shown in Figure 11 with the controller in operation. Beneath the table can be seen the crank which controls the inclination of the table, and thereby the intensity of pressure in the water columns.

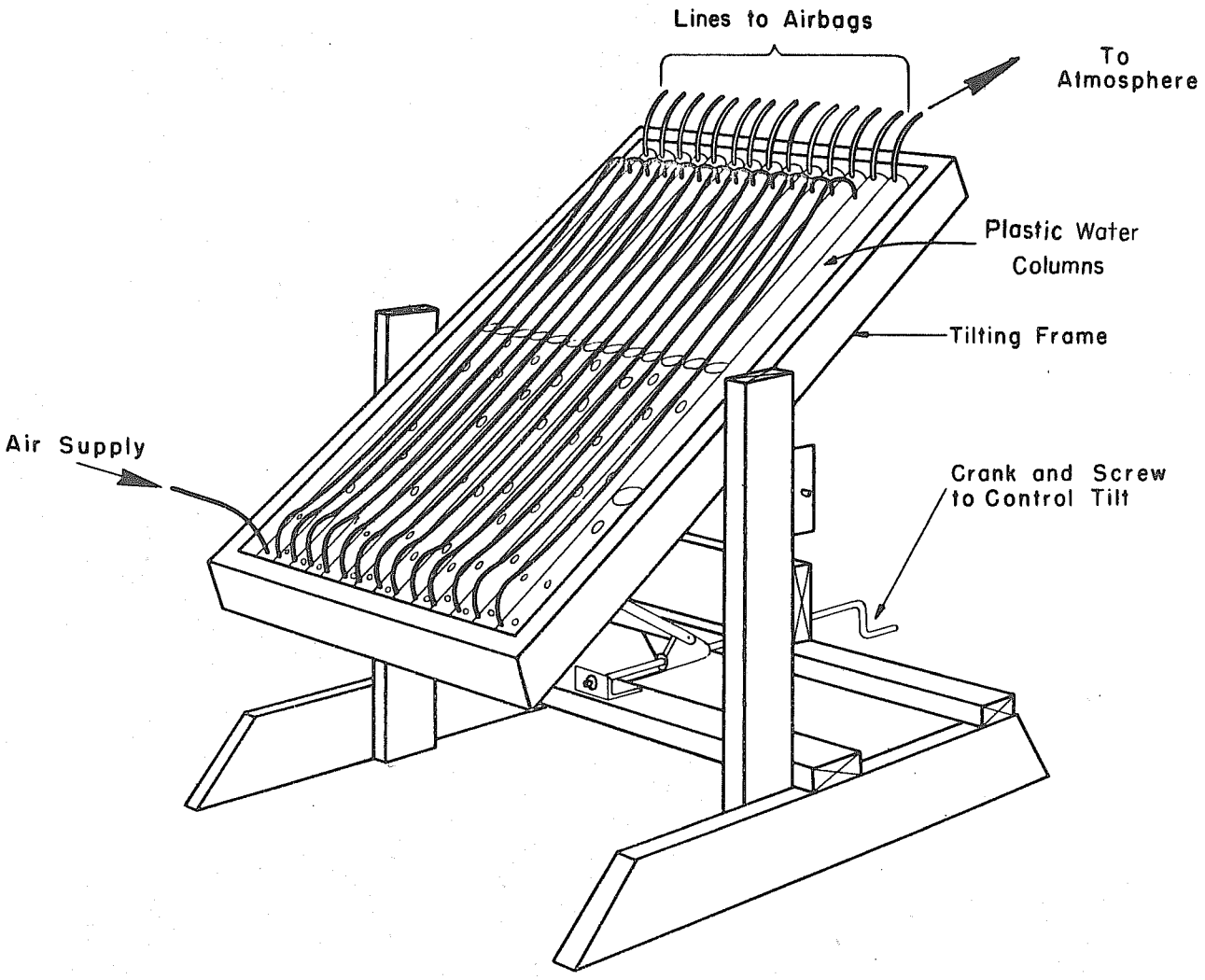


FIGURE 11 - SKETCH OF DIFFERENTIAL PRESSURE CONTROLLER

The air bags are shown in Figure 12 being fitted onto the backup frame. These are made of 1/16 inch pure gum rubber sheet weighing 3 pounds per yard. After cutting to size, the single-lapped joints were painted with vulcanizing cement, and a 1/32 inch layer of black vulcanizing gum was laid in the joint. Two tire valves were also mounted to each bag, and the entire unit was then vulcanized by the kettle process.

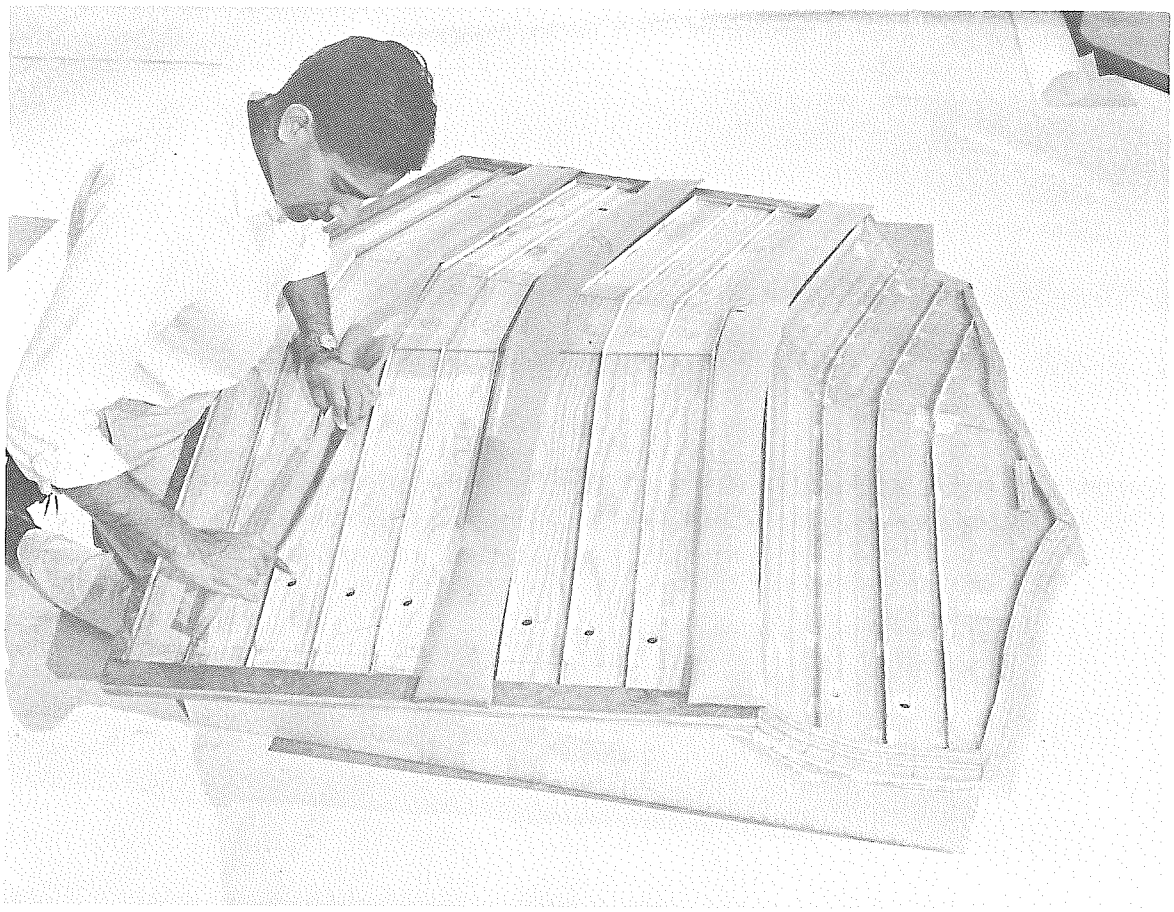

FIGURE 12 - BACKUP FRAME BEING FITTED WITH AIR BAGS

Figure 12 shows the back-up plate which was molded to follow the contour of the upstream face of the dam and plug, and which took the reaction of the air pressure. The figure also shows the thin narrow strips of aluminum that were bonded to the back-up plate in order to help maintain the air bags in position. In addition, the air bags were glued to the back-up plate for ease in handling, when removing the loading device from the model.

The operation of the pressure controller was quite simple. A crude inclinometer was attached to the side of the frame, and calibrated for various intensities of loading. For any test, the table was inclined to the proper angle, and air fed into the high-pressure column. It took an appreciable

time to fill each air bag in turn, indicated by the beginning of bubbling in each water column, but once all air bags had filled, the air supply could be cut down considerably to maintain the pressure. Final adjustment of the pressure was made by correcting the tilt of the table, and checking the manometer pressure.

Two compensating errors are introduced when using air bags for hydrostatic loading. There is a slight shift upward in the resultant force in each air bag, caused by the difference in location of the centroid of rectangular versus trapezoidal areas. This shift decreases as pressure increases, and the error in position of the resultant of all loads decreases with an increase in the number of bags. The force applied to the surface from the air bags is the product of the inside area of the bag and the pressure, and hence no pressure is applied to the face over narrow strips, at the juncture of each pair of bags, having a width of twice the thickness of the air bag walls. Separate tests were run to calibrate these effects, and control was established on the lowest bag bearing on the main arch to give the correct magnitude of the resultant load.

Manometer

The pressures in the individual air bags were read on the mercury manometer shown on Figure 13. As indicated on the schematic diagram, Figure 9, this consisted of fifteen 1/8 inch i. d. by 5 foot glass tubes, connected in parallel through a 1/2 inch black iron pipe to a 6 inch diameter reservoir. With a reservoir of this size, the change in zero caused by mercury displaced from the individual tubes under pressure was negligible, and the manometer became direct reading. The connection of glass tube to iron pipe was made through flexible tubing to avoid breakage. A sheet of

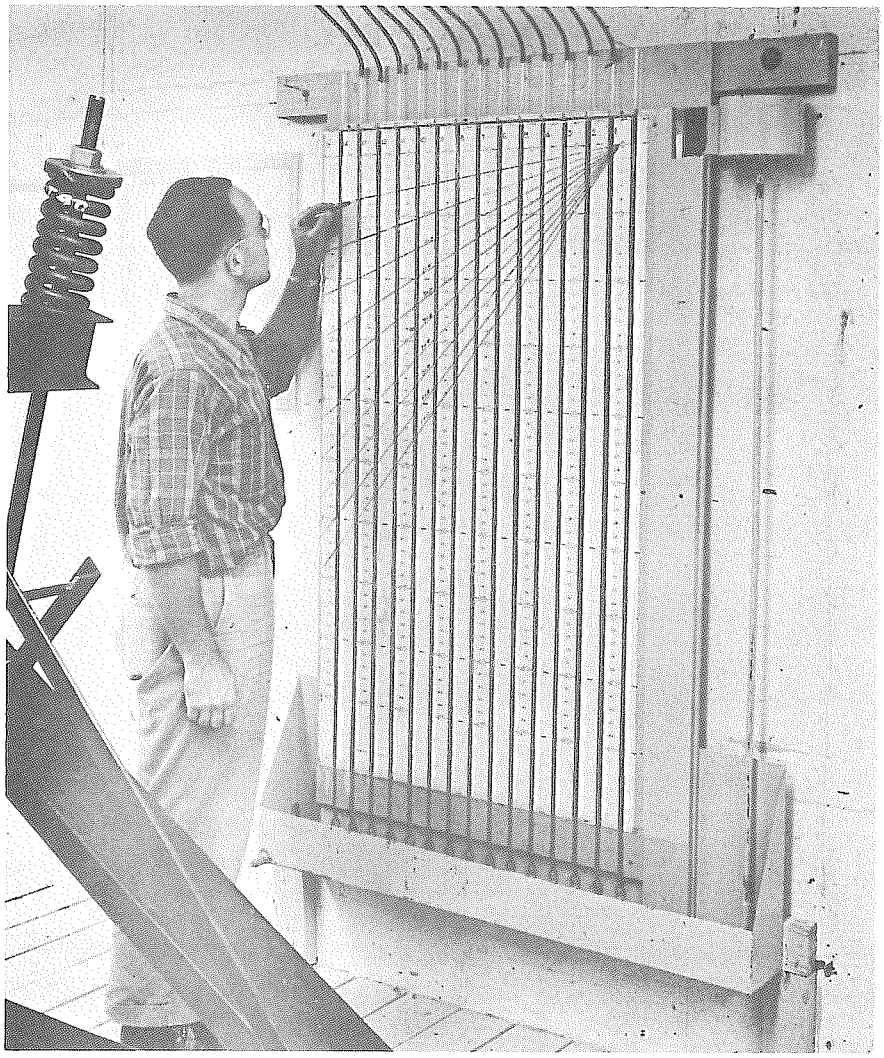

FIGURE 13 - MERCURY MANOMETER FOR CHECKING AIR BAG PRESSURE

transparent acetate was stapled over the tubes so that control gradients could be drawn with a grease pencil. These were drawn including the pressure correction for the air bags so that no further correction was needed on the readings. In practice, since the pressure system automatically maintained the correct gradient, it was not necessary to read the pressure on all bags, and only the lowest bag bearing on the dam, No. 10, was used to establish the control pressure. At the same time, a quick visual check on all bags was made by comparing the mercury in all tubes with the appropriate gradient line.

Counter-Weight System

As can be seen on Figure 14, the resultant of the live load passed through the base so close to the downstream edge of the model that tensile stresses which were a large percentage of the ultimate tensile strength of the model material were formed at the upstream edge of the foundation.

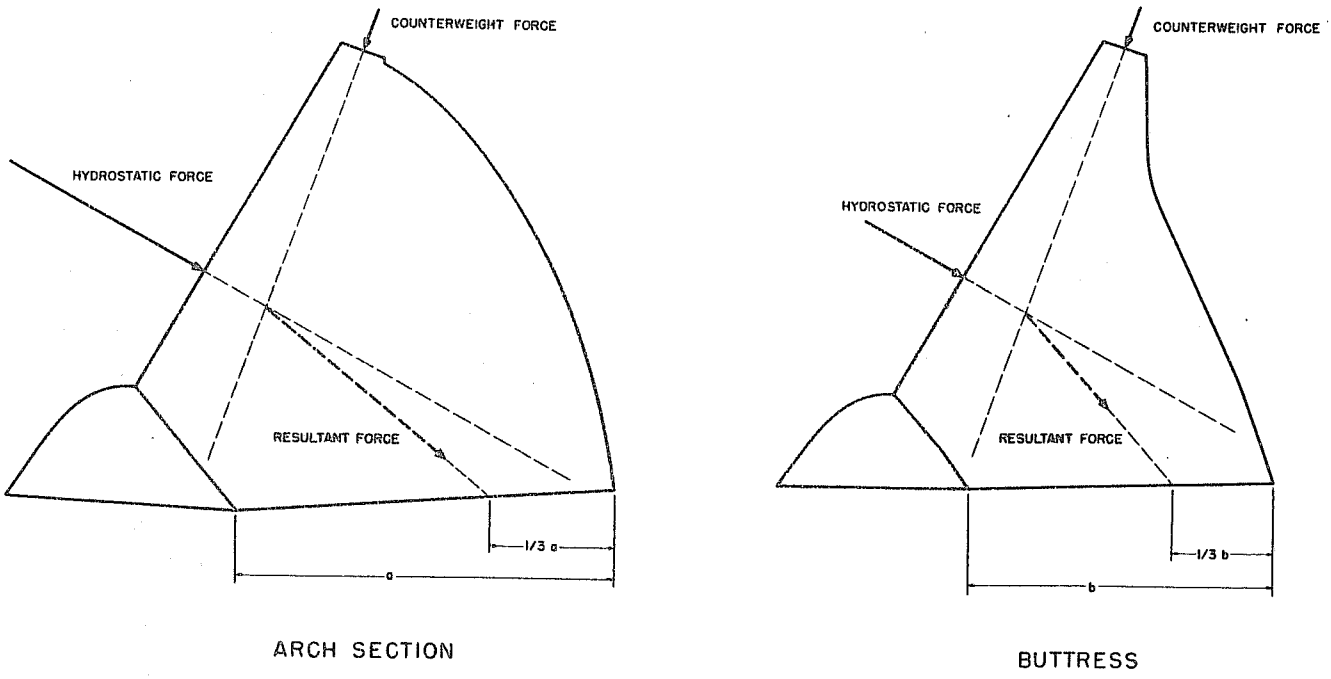


FIGURE 14 - EFFECT OF COUNTER WEIGHT FORCES ON STABILITY

In the independent buttresses, the resultant actually passed outside the base of the buttress, and it was potentially unstable. Of course, in an actual dam, the dead load of the dam would combine with the live load to bring the resultant well within the base of each member, but in the model, dead load is insignificant. For this reason, it was necessary to add a load to the model to cause the resultant of the load and the hydrostatic force to lie within the middle third of the foundation. The counter-weight load was applied and maintained through large springs, as shown in Figure 15. The magnitude of the load

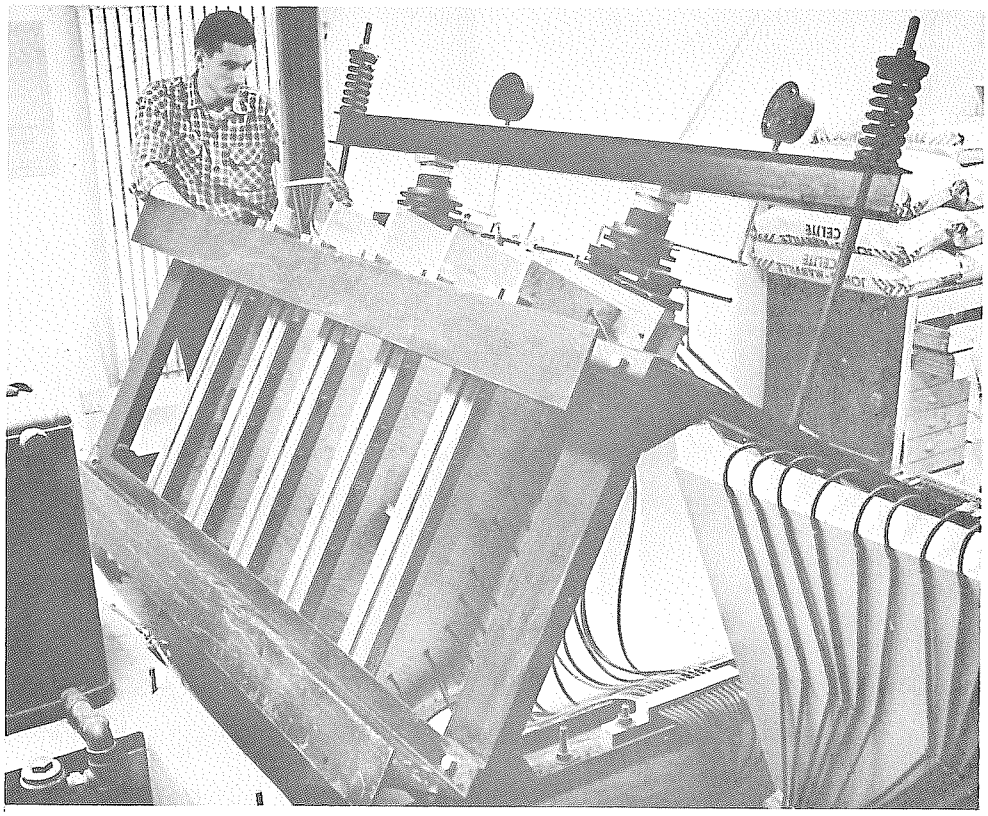

FIGURE 15 - GENERAL VIEW OF REACTION FRAME AND COUNTERWEIGHT

was measured by pressure gages connected to hydraulic load cells. Since the counter-weight load was applied before hydrostatic testing and maintained during testing, the measured strains due to hydrostatic loading were independent of the counter-weight load. The load was distributed to the riding buttress and two independent buttresses by a series of rocker arms.

Instrumentation

The strain measuring program was based on the use of SR4 bonded-wire strain gages, applied to the surface of the model. These were used in large quantity in both rosette and single gage forms, and necessitated some innovations in instrumentation so that large numbers of readings could be made in a short time. This required special details in compensation, switching, and the measuring circuit itself, to increase the speed of readings. The deformation measurements were based on the use of 0.0001 inch dial gages; although in a few confined locations where the use of dial gages was impossible, SR4 clip gages were used.

Gage Locations

The central portion of the arch and buttress dam is symmetrical, and it was symmetrically loaded. Thus, in the model tests, it was decided to concentrate most of the strain gages on the right half of the arch, and include enough check gages on the left half to check the assumed symmetry of structural behavior. Locations of special interest were at the crown of the structure on the intrados and extrados, the contact between the arch and its foundations, the edge of the outstanding leg, and the boundaries of the riding buttress. Gages were installed at all these locations, and in other locations in between in order to establish the distribution of stresses. All gages at the base of the dam were located 20 feet from the contact, in order to remove them to some extent from the region of rapidly

changing stress conditions immediately adjacent to the contact. Another point of interest was the actual distribution of stress through the cross section of the arch at various points. Preliminary study was given to a pressure-sensitive miniature gage that showed some promise, but when this proved unreliable, no further attempt was made to measure internal stresses.

Relative displacement of adjacent parts of the dam were of special interest, chiefly in the design of the water seals, and the dial gage locations were established to measure these relative movements. The array of strain gage locations is shown on Figure 16.

Strain Gages

Two types of gages were used for measuring surface strains on the model: Type AR-1 rosettes, and type A-1 single gages, having 13/16 inch gage lengths. These were chosen after a series of studies of temperature compensation, bonding, and the reliability of rosettes.

Temperature compensation is the most difficult problem encountered when attaching strain gages to plaster models. This is no problem at all when working with metal models and structures, since the slight amount of heat generated by the current passing through the strain gage when it is connected to the test set is readily dissipated through the metal. However, the thermal characteristics of plaster are entirely different, and the heat is stored, rather than dissipated. Ordinarily, a single dummy gage can be used for temperature compensation of a number of live strain gages. However, when working with plaster, the heat passing nearly continuously through the dummy gage raises it temperature in comparison to that of the live gage which is heated only when read, causing the gage readings to drift. A number of schemes were tried to obviate this difficulty. Compensatory heating circuits were devised so that live gages, instead of being heated

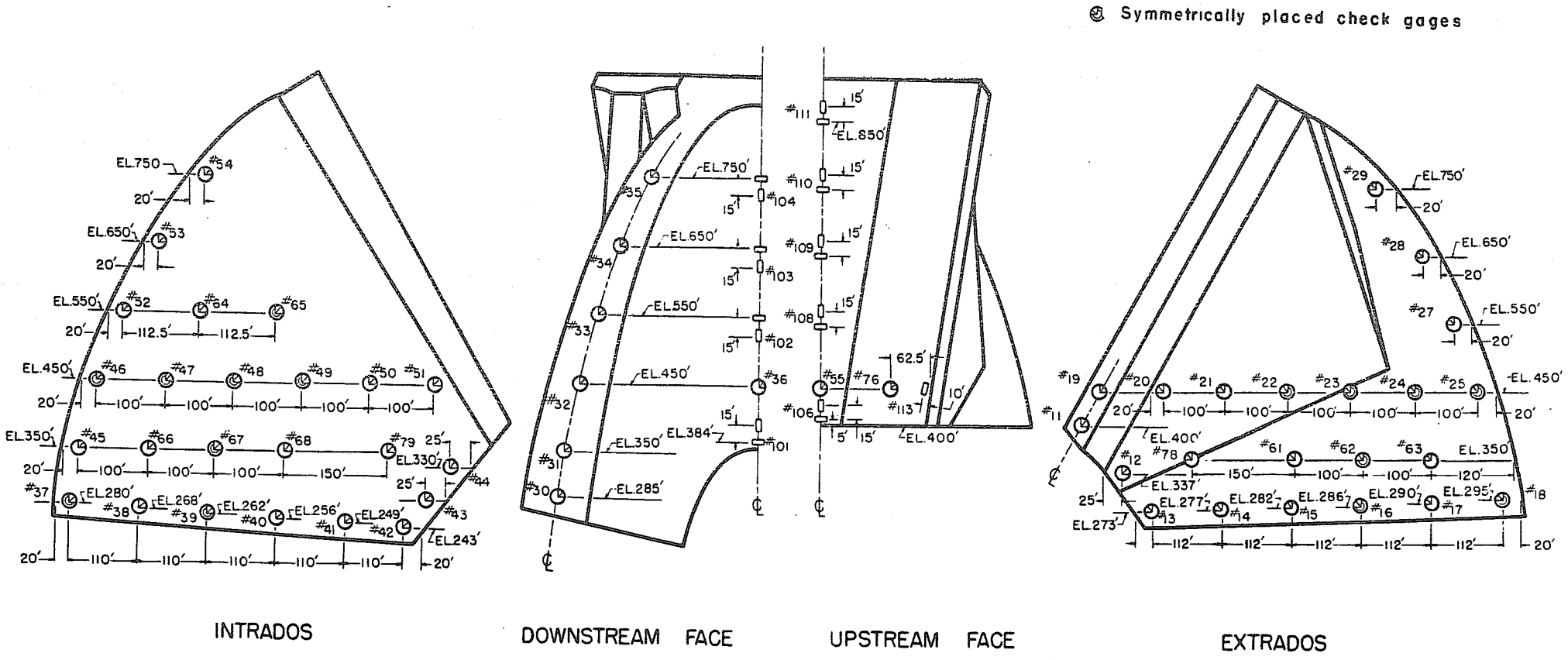


FIGURE 16 - STRAIN GAGE LOCATION

only when being read, were heated continuously with an auxiliary circuit so that temperature flow was constant in both live and dummy gage. This scheme was tried with both wire gages and foil gages. The scheme proved complex, and did not accomplish its desired purpose. Most of the drift was eliminated by a modification in bridge voltage. By adding a series resistor to the power supply circuit, the bridge voltages was reduced from 8 volts to 2-1/2 volts. The drift was found to be completely eliminated by switching dummy gages along with the active gages. Since it was impractical to provide a dummy gage for each active gage, a switching system was used that allowed for the repeated use of 24 dummy gages, arranged so that each dummy was used in turn with every 24th live gage. This afforded ample time for the slight amount of heat developed in each dummy gage to be dissipated between readings.

The strain gages were bonded to the surface of the plaster by Armstrong's epoxy cement, Type A.

Question had been raised whether strain gage rosettes might not be too stiff for plaster, and thereby modify through their own stiffness, the local state of strain. A test block was arranged, as shown in Figure 17, in which single A-1 gages were cemented along the extensions of the gage lines of a Type AR-1 rosette. Plotting the strains through the single gages and rosettes showed no evidence of local distortion due to the presence of the rosette, and the rosettes, which are much more convenient for use than single gages, were selected for basic instrumentation.

A total of 65 rosettes and 20 single gages was attached to the model, giving a total of 215 gages to be read. Twenty-four single gages were attached to plaster cylinders for use as dummies.

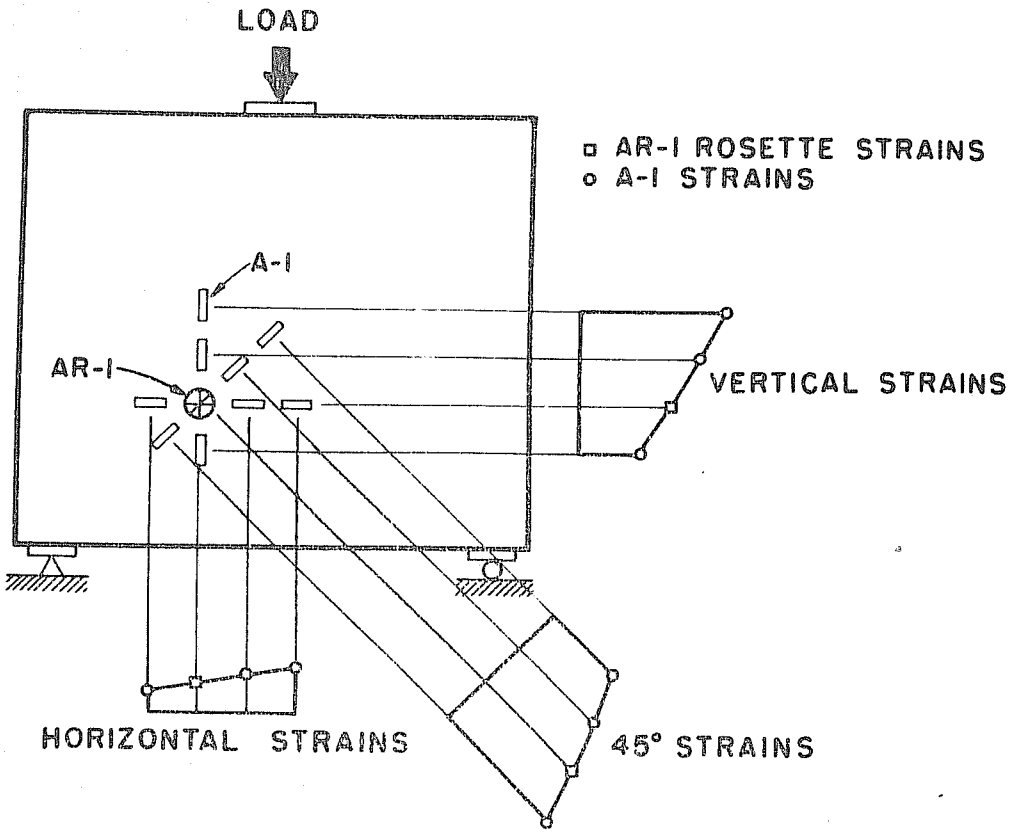


FIGURE 17 - TEST FOR ACTION OF STRAIN GAGE ROSETTES

Test Set, Switching, and Compensation

Instrumentation for reading the strain gages was based on the use of the Datran electronic resistance bridge indicator (RBI), shown in Figure 19. When connected to any strain gage, this bridge automatically balances itself to the resistance of the strain gage, and indicates strain in micro-inches on a numerical display, when the strain gage factor is adjusted on its face. Since the RBI automatically balances to the strain gage input, it was necessary to interpose a switching unit between the strain gages and the RBI. The switchboard, shown diagramatically in Figure 18 and also pictorially in Figure 19, was borrowed intact from

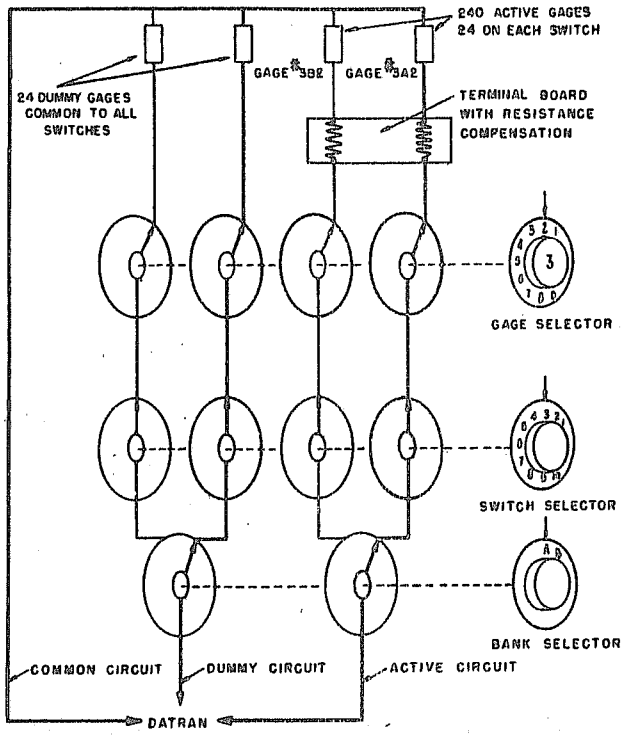


FIGURE 18 - SWITCHING CIRCUITS

a previous project.[10] The basic unit for this switchboard was the Leeds and Northrup 4-pole, 12 position, silver contact selector switch. Each switch was hooked up to 24 live gages and 24 dummy gages in two banks of 12 gages each. Connection to any individual pair of live and dummy gages was made through the use of the bank selector and switch selector. Thus, by operating the switches sequentially, each dummy gage was only used once every 24 readings.

Balancing of the RBI is accomplished by means of a servo motor than can traverse the 2, 000 micro-inch per inch range in 4 seconds.

Variations in initial resistance of individual strain gages caused many of their initial strain readings to fall outside the 2000 micro-inch per inch range of the RBI. Hence, a compensating board was interposed

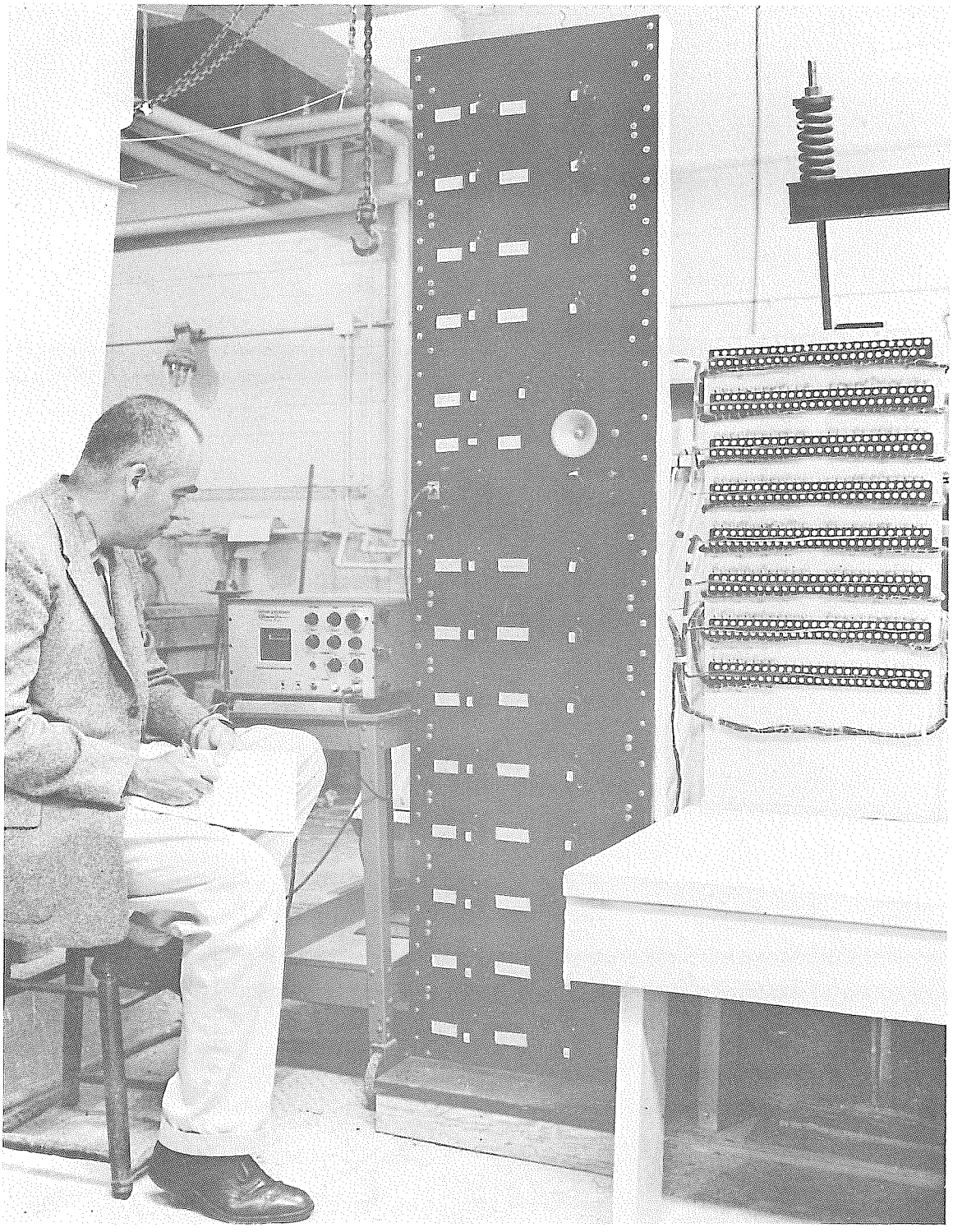

FIGURE 19 - ARRANGEMENT OF STRAIN GAGE RECORDING EQUIPMENT

between the switchbox and the RBI, on which manganin wire resistors were inserted in series with each strain gage, and adjusted until each individual live strain gage read 1,000 micro-inches per inch, the mid-point of the indicator scale. Thus, with each strain gage individually balanced to a common point, the slight unbalance due to test loads could be balanced by the RBI in a minimum time, greatly speeding up the operation. With this setup, on several occasion, 150 strain gages were read in 10 minutes. The small change in gage resistance made by the compensating resistor was corrected by a change in gage factor.

A Clary automatic printer was added to the instrumentation so that the strain indication as well as the meter number and other numerical information could be printed out on an adding machine tape. While this was convenient in some parts of the test, most of the data were recorded by hand in ruled columns in notebooks, where it was much easier to compare corresponding strain gage readings for several tests.

In addition to the live gages on the model and the dummy gages, two gages were cemented to an Invar steel bar, to check any possible drift in the RBI itself during a test.

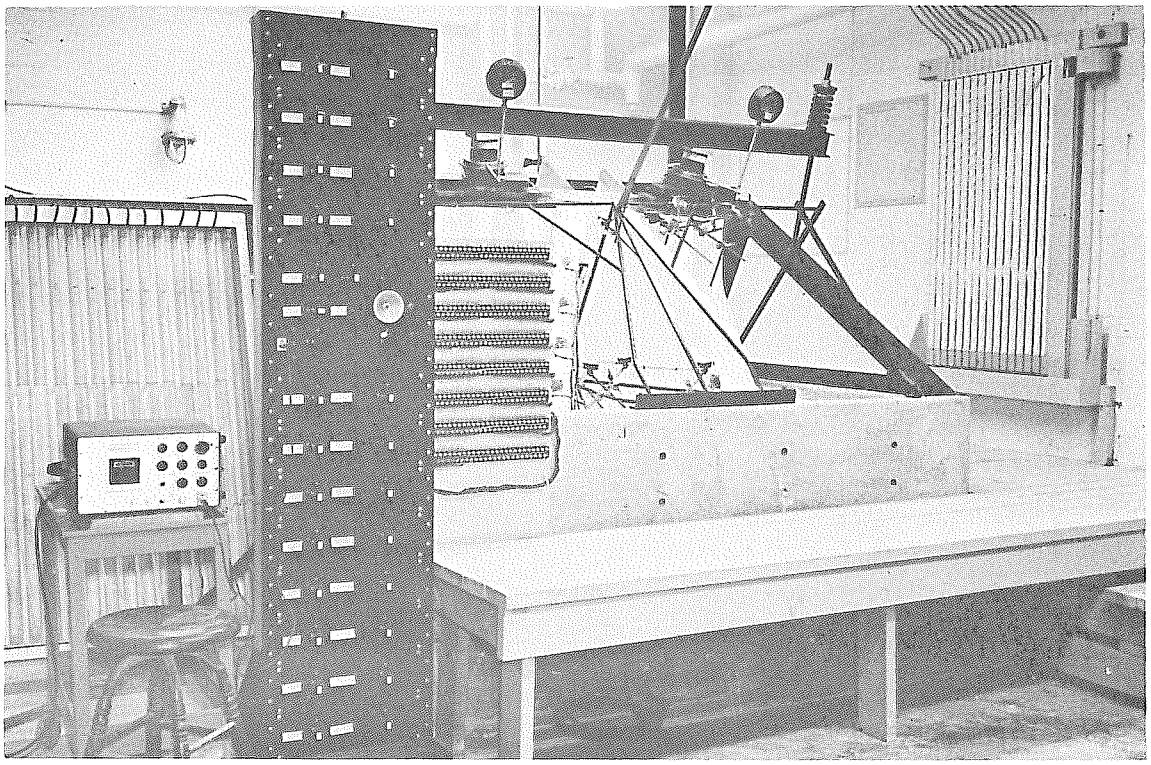

FIGURE 20 - GENERAL VIEW OF TESTING AREA

## DETERMINATION OF STRESSES DUE TO HYDROSTATIC LOADING

### Test Procedures

As described in Appendix A, tests conducted on the plaster-celite model material indicated that its mechanical properties were a function of its water content. A uniform condition of zero free moisture content was used as the control for the moisture content of all parts of the model. Careful control of the room humidity was not strictly necessary, since preliminary tests on the model material indicated that normal variation in laboratory humidity did not affect the mechanical properties of the plaster. Nonetheless, the humidity in the test chamber was maintained at a relative humidity of 50% $\pm$ 5%.

Since model strains due to load were small, any temperature changes within the model during testing could cause large errors in the measured strains. For this reason, most of the testing was done when temperature conditions had come to equilibrium, in as short a time as possible, and using the minimum number of people. No casual visitors were allowed when testing was in progress, to avoid convected and radiated heat from these individuals.

The general layout of the testing area is shown in Figure 21. All adjustments of load and reading of instruments could be accomplished without approaching the model, thus reducing to a minimum any disturbance of the readings by vibration or heat transfer.

For the hydrostatic loading test, a test cycle was selected on the basis of creep tests conducted on a beam made of the model material. These creep tests, described in Appendix A, indicated that most of the creep occurred within the first 10 minutes after loading. It was also

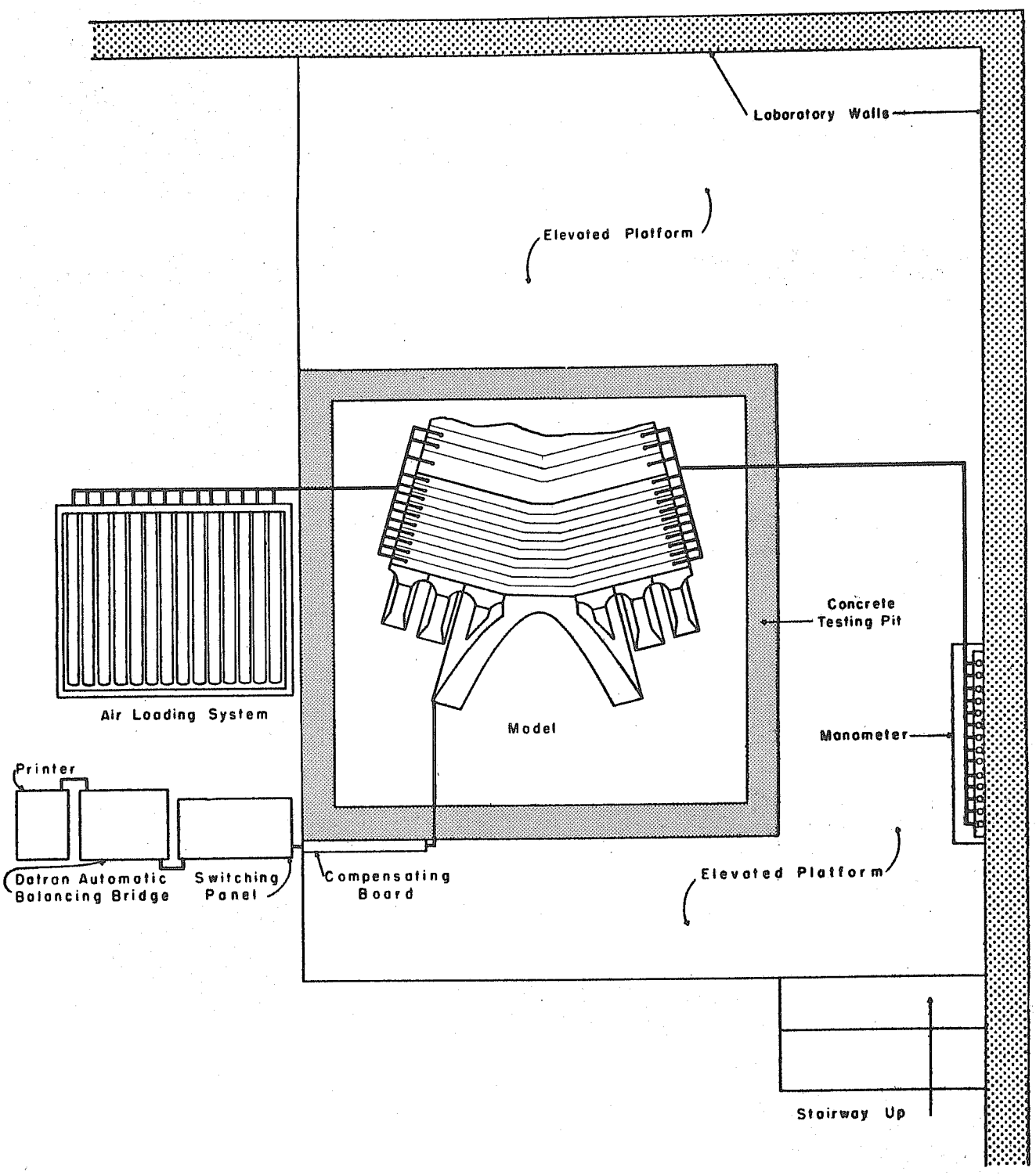


FIGURE 21 - LOADING AND INSTRUMENTATION FOR HYDROSTATIC LOAD TESTS

noted that strains in the model for the first few cycles of loading were not typical of those recorded after a number of cycles. Thus, strains recorded during the first few cycles of loading were neglected in the analysis.

In loading the model, the counterweight load was applied first. This was followed by the application of the water load at the desired intensity, at the same time checking the counterweight load carefully. This ensured that this factor remained constant during the test, so that the recorded strains would be caused only by the addition of the live load.

For testing purposes, the strain gages were separated into four groups with 48 gages in each group. Three tests were run for each group, making a total of 12 tests for each loading condition. The cycle for any one of these tests was as follows:

| | |
|---|---|
| 0 - 5 minutes | Model loaded |
| 5 - 15 minutes | Time allowed for model to creep |
| 15 - 20 minutes | Group of gages read twice |
| 20 - 21 minutes | Model unloaded |
| 21 - 25 minutes | Time allowed for model to rebound |
| 25 - 30 minutes | Group of gages read twice |

The data obtained by the use of the above testing cycle appeared to be completely free of errors due to creep. Because of the short time of 15 minutes between loaded readings and unloaded readings, the possibility of introducing any temperature strains was minimized. All three tests for any one loading condition agreed with each other within the accuracy of testing, $\pm$ 1 micro-inch. The final value of strain was taken as the average of the three tests.

Strains were recorded at a number of stress levels, in order to determine the linearity of strain response of the model to the loads imposed

on it. Figure 22 shows the strains at a number of gages plotted against the intensity of loading. This condition was typical of all strain gage readings, indicating complete linearity of strain to load.

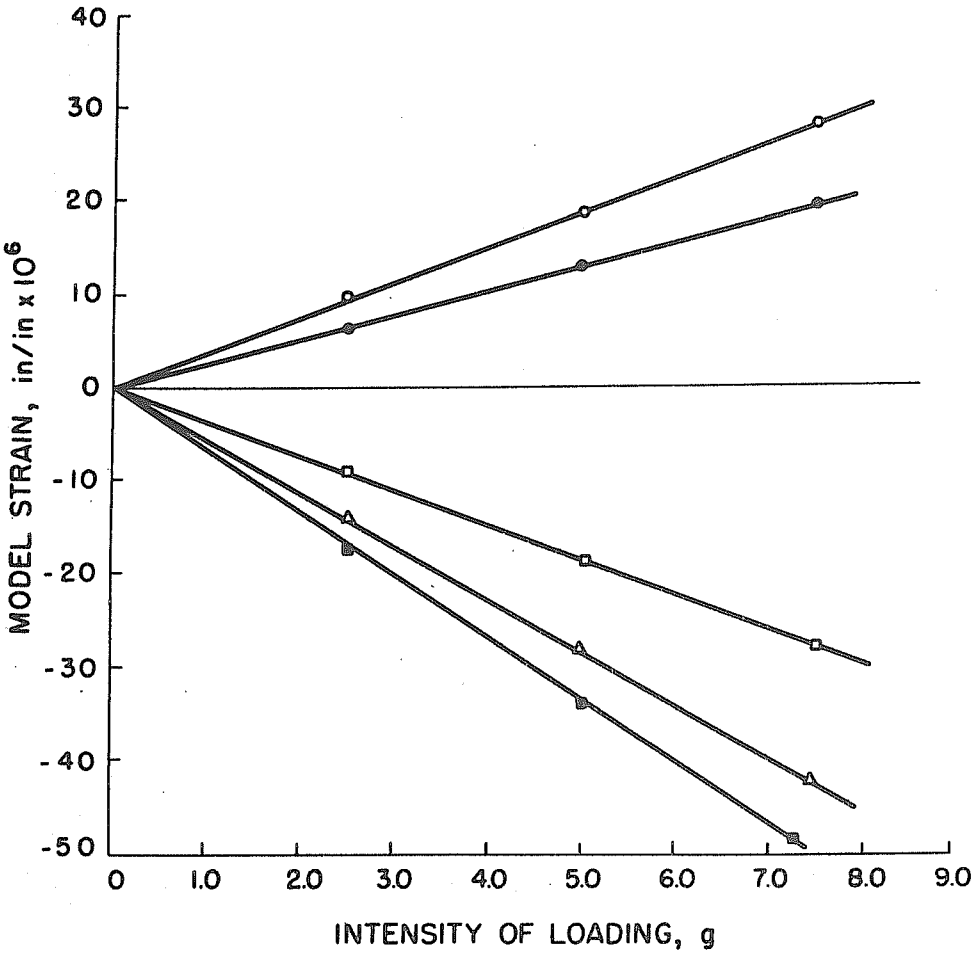


FIGURE 22 - LINEARITY OF RESPONSE OF MODEL TO INTENSITY OF LOAD

## Model Similitude

Stress and force relationships between the model m and the prototype p involve consideration of size, elastic modulus, and intensity of loading. The model must be constructed to an exact scale so that it is geometrically similar to the prototype. Within the range of stresses studied, the model material must have a stress-strain relationship

similar to that of the prototype material. Loads applied to the model must be in some proportion to loads applied to the prototype. No other variables need be considered if both model and prototype are made of isotropic materials having equal Poisson's ratio and loaded within the elastic range.

For a geometrically similar model, the ratio of model length $L_m$ to prototype length $L_p$ is defined as

$$\lambda = \frac{L_m}{L_p} \tag{1}$$

The ratio of the density of model loading $\gamma_m$ to the density of prototype loading $\gamma_p$ is defined as

$$g = \frac{\gamma_m}{\gamma_p} \tag{2}$$

Thus, for a live load test in which a dam loaded with water is simulated by a model dam loaded with mercury, g equals 13.6. Similarly, for a test in which a dead load test of a model dam made of plaster weighing 40 pounds per cubic foot is set up to represent a prototype dam made of mass concrete weighing 155 pounds per cubic foot, the value of g is 0.26.

Expressed in these units, force then becomes $F = \gamma L^3$ and stress $\sigma$, which is force per unit area, becomes

$$\sigma = \frac{F}{L^2} = \frac{\gamma L^3}{L^2} = \gamma L \tag{3}$$

Thus, the relationship of stresses between model and prototype can be shown to be

$$\frac{\sigma_m}{\sigma_p} = \frac{\gamma_m L_m}{\gamma_p L_p} = g\lambda \tag{4}$$

Similitude factors for strain e can be derived starting with the elastic stress-strain relationship:

$$e = \frac{\sigma}{E} \tag{5}$$

where E = modulus of elasticity.

Since Hooke's law holds within the elastic range for both model and prototype, the ratio of prototype strain to model strain can be found by

$$\frac{e_p}{e_m} = \frac{\sigma_p}{E_p} \cdot \frac{E_m}{\sigma_m} = \frac{1}{g\lambda} \cdot \frac{E_m}{E_p} \tag{6}$$

and

$$e_p = \frac{1}{g\lambda} \cdot \frac{E_m}{E_p} \; e_m \tag{7}$$

Model stress is determined from model strain. If $\mu$ is Poisson's ratio, the strain in the x direction is related to the measured strains by the following equation expressing Hooke's law

$$\sigma_x = \frac{E}{1-\mu^2} \left(e_x + \mu e_y\right) \tag{8}$$

Now if equation (7) is substituted in equation (8), the relationship between prototype stress and model strains is found to be

$$\sigma_{xp} = \frac{E_p}{1-\mu^2} \cdot \frac{1}{g\lambda} \cdot \frac{E_m}{E_p} \left(e_{xm} + \mu e_{ym}\right) \tag{9}$$

or

$$\sigma_{xp} = \frac{1}{g\lambda} \cdot \frac{E_m}{1-\mu^2} \left(e_x + \mu e_y\right)_m \tag{10}$$

Gross deformation in the model $\Delta_m$ and in the prototype $\Delta_p$ are found by rewriting equation (5) and substituting equation (7)

$$e = \frac{\Delta}{L} \tag{5}$$

$$e_p = \frac{1}{g\lambda} \cdot \frac{E_m}{E_p} \; e_m \tag{7}$$

$$\frac{\Delta_p}{L_p} = \frac{1}{g\lambda} \cdot \frac{E_m}{E_p} \cdot \frac{\Delta_m}{L_m} \tag{11}$$

and

$$\Delta_p = \frac{1}{g\lambda^2} \cdot \frac{E_m}{E_p} \Delta_m \tag{12}$$

Similitude factors were computed for data reduction using the following elastic constants:

| | | |
|---|---|---|
| Elastic modulus for concrete | $E_p$ | 4,000,000 psi |
| Elastic modulus for plaster | $E_m$ | 240,000 psi |
| Poisson's ratio | $\mu$ | 0.24 |
| Scale factor | $\lambda$ | 1:200 |
| Load factor, for stress/strain | $g$ | 7.5 |
| Load factor, for deflections | $g$ | 5.0 |

Thus, for strains,

$$e_p = \frac{1}{g\lambda} \frac{E_m}{E_p} e_m = \frac{200}{7.5} \cdot \frac{240,000}{4,000,000} e_m = 1.6 e_m$$

or, the actual strains in the dam would be 1.6 times as large as those measured in the model.

Similarly, for stress,

$$\sigma_{xp} = \frac{E_m}{g\lambda(1-\mu^2)} (e_{xm} + \mu e_{ym})$$

$$= \frac{240,000 \times 200}{7.5(1-.24^2)} (e_{xm} + \mu e_{ym})$$

$$= 6.80 \times 10^6 (e_{xm} + \mu_{ym})$$

The prototype stresses in psi were 6.8 times the corrected model strains measured in microinches per inch.

For deflections,

$$\Delta_p = \frac{1}{g\lambda^2} \cdot \frac{E_m}{E_p} \Delta_m = \frac{200^2}{5.0} \cdot \frac{240{,}000}{4{,}000{,}000} \Delta_m = 480 \Delta_m$$

Using dial gages reading to the nearest 0.0001 inch, actual deflections in inches were 0.048 times the indicated model deflections in 0.0001-inch units.

Reduction of Data

The data obtained from the test were in the form of strain indications in a particular direction for a definite state of loading. The results desired were the principal stresses and their direction, as well as the vertical and horizontal normal and shearing stresses. Transition from data to desired results was made using the computation sheet, shown in Figure 23, in which successively the raw strain data were corrected for cross sensitivity of the gages, the principal stresses and their magnitude in prototype dimension were determined, and the vertical and horizontal normal stresses and shears were computed. All computations were made with slide rule and desk computers and could be accomplished accurately and rapidly. Furthermore, the computation form facilitated checking of the computations. As might be expected, standardizing the computations to a set series of routine operations reduced the time lag between raw strain observations and computed principal stresses to a minimum. In the sections that follow, the relationships underlying the computation routines are described.

Correction for Cross-Sensitivity of Strain Gages

The bonded wire strain gage responds with a resistance change to strains parallel to its longitudinal axis. In addition, since a certain fraction of the wire is bonded perpendicular to the main axis of the strain gage, because of the strain gage configuration, the gage will also respond to some

| 12 | 13 | 14 | 15 | 16 | 17 | 18 |
|---|---|---|---|---|---|---|
| ⑤−⑩ = $e_2$ | ⑧ ÷ 2 = θ | K(⑪ + ⑫μ) = $\sigma_1$ | K(⑫ + ⑪μ) = $\sigma_2$ | K(② + ④μ) = $\sigma_x$ | K(④ + ②μ) = $\sigma_y$ | $\frac{⑯ - ⑰}{2}$ TAN 2θ = $\tau_{xy}$ |
| +20.5 | -37.4° | -104 | +108 | -26 | +30 | 103 |
| +24.7 | -37.6° | -427 | +59 | -242 | -120 | 232 |
| +19.6 | -41.6° | -322 | +50 | -174 | -114 | 252 |
| +21.0 | -42.4° | -466 | +25 | -242 | -196 | 253 |
| +20.2 | -42.9° | -440 | +26 | -224 | -190 | 228 |
| -50.3 | +44.2° | +18 | -320 | -143 | -152 | 165 |
| -33.1 | +29.8° | 0 | -215 | -46 | -161 | 94 |

## CORRECTION FOR CROSS SENSITIVITY

$e_0 = R_0 - 1/b\, R_{90}$

$e_{45} = (b+1/b)R_{45} - 1/b\,(R_0 + R_{90})$

$e_{90} = R_{90} - 1/b\, R_0$

$b = \frac{1}{65} = 1.5\,\%$

## PRINCIPAL STRAINS

$$\text{TAN } 2\theta = \frac{\frac{e_0 + e_{90}}{2} - e_{45}}{\frac{e_0 - e_{90}}{2}}$$

$$\left\{ \begin{matrix} e_1 \\ e_2 \end{matrix} \right\} = \frac{e_0 + e_{90}}{2} \pm \frac{e_0 - e_{90}}{2} \text{ SEC } 2\theta$$

## DIRECTIONS

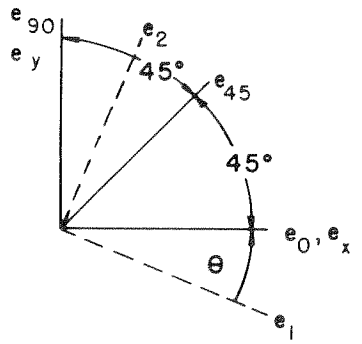


## PROTOTYPE PRINCIPAL STRESSES

$\sigma_1 = K(e_1 + \mu e_2)$

$\sigma_2 = K(e_2 + \mu e_1)$

$K = \frac{1}{g\lambda} \times \frac{E_m}{1-\mu_m^2} = 6.80$

$E_m$ = 240,000 psi

$\mu_m$ = 0.24

$g$ = 7.5

$\lambda$ = 1/200

**OROVILLE DAM STUDIES**
**UNIVERSITY OF CALIFORNIA**
**BERKELEY, CALIFORNIA**

HYDROSTATIC LOADING

| 1 | 2 | 3 | 4 | 5 | 6 | 7 | 8 | 9 | 10 |
|---|---|---|---|---|---|---|---|---|---|
| GAGE NO. | $R_0$ | $R_{45}$ | $R_{90}$ | $\frac{e_0+e_{90}}{2}$ | $\frac{e_0-e_{90}}{2}$ | $\frac{(5)-(3)}{(6)} =$ TAN 2θ | 2θ | SEC 2θ | (6)x(9) |
| | $e_0$ | $e_{45}$ | $e_{90}$ | | | | | | |
| 19 | - 5 | - 19 | + 5.5 | +0.25 | - 5.35 | - 3.68 | - 74.7° | + 3.79 | - 20.3 |
| | - 5.1 | - 19.4 | + 5.6 | | | | | | |
| 20 | - 33 | - 64.8 | - 10 | - 21.15 | - 11.65 | - 3.81 | - 75.3° | + 3.94 | - 45.9 |
| | - 32.8 | - 65.5 | - 9.5 | | | | | | |
| 21 | - 20.3 | - 51 | - 12 | - 15.9 | - 4.2 | - 8.40 | - 83.2° | + 8.45 | - 35.5 |
| | - 20.1 | - 51.2 | - 11.7 | | | | | | |
| 22 | - 34.3 | - 72 | - 22 | - 25.75 | - 4.25 | - 11.0 | - 84.8° | + 11.0 | - 46.8 |
| | - 30.0 | - 72.6 | - 21.5 | | | | | | |
| 23 | - 27.8 | - 67.8 | - 21.3 | - 24.2 | - 3.3 | - 13.4 | - 85.8° | + 13.4 | - 44.4 |
| | - 27.5 | - 68.4 | - 20.9 | | | | | | |
| 24 | - 16.5 | - 49.8 | - 18.3 | - 17.2 | + 0.9 | + 36.8 | + 88.45° | + 36.8 | + 33.1 |
| | - 16.3 | - 50.3 | - 18.1 | | | | | | |
| 25 | - 1.5 | - 30 | - 23 | - 12.1 | + 10.9 | + 1.64 | + 56.6° | + 1.92 | + 21.0 |
| | - 1.2 | - 30.2 | - 23 | | | | | | |

FIGURE 23 - STRAI

extent to strains at right angles to the principal axis of the strain gage. This response is termed "cross-sensitivity", and although it is often neglected, with an error of not greater than 3% in exploratory testing, it must be taken into account when precision in testing is desired. The ratio of the total longitudinal length of wire to the total lateral length of wire used in the gage is defined as b. If R is the apparent strain read by the instrument, based on the gage factor supplied with the strain gage, then the true strain e for all axes of the rosette are

$$e_0 = R_0 - \frac{1}{b} R_{90} \tag{13}$$

$$e_{45} = \frac{b}{b-1} R_{45} - \frac{1}{b}(R_0 + R_{90}) \tag{14}$$

$$e_{90} = R_{90} - \frac{1}{b} R_0 \tag{15}$$

Thus, for the particular strain gages used in these rosettes the correction amounted to about 2% of the normal strain, as can be seen on the computation form.

Calculation of Principal Strains

Having corrected the individual indicated surface strains for the cross sensitivity of the strain gages, the principal strains and their directions on the surface of the model were calculated using the well-known equations of elasticity. Following the notation of Figure 24,

$$e_1 = \frac{e_0 + e_{90}}{2} + \frac{e_0 - e_{90}}{2} \sec 2\theta \tag{16}$$

$$e_2 = \frac{e_0 + e_{90}}{2} - \frac{e_0 - e_{90}}{2} \sec 2\theta \qquad (17)$$

$$\tan 2\theta = \frac{\frac{e_0 + e_{90}}{2} - e_{45}}{\frac{e_0 - e_{90}}{2}} \qquad (18)$$

The strain gage rosettes were installed so that the 0° and 90° leg were always horizontal and vertical, and the 45° leg lay in the general direction of the expected maximum principal stress. Thus, the rosettes were oriented in two ways: one as shown in Figure 24, and one the mirror

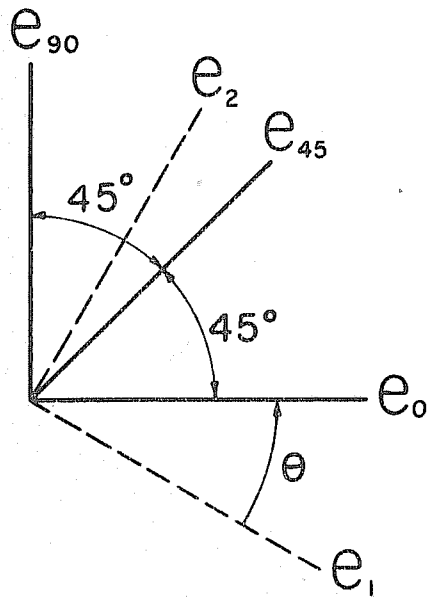


FIGURE 24 - ORIENTATION OF PRINCIPAL STRESSES

image of this. The determination of the direction of principal stress was made automatically, according to the algebraic sign of the computation. As developed here, the angle $\theta$ is measured from the first principal stress to the horizontal axis. Hence, in laying out the angle of the first principal stress, it is laid out as the negative of the angle $\theta$ computed from the table, and on axes determined by the actual strain gage orientation.

Principal Stresses

Having determined the principal model strains, the principal prototype stresses were computed directly using

$$\sigma_1 = K(e_1 + \mu e_2) \tag{19}$$

$$\sigma_2 = K(e_2 + \mu e_1) \tag{20}$$

where

$$K = \frac{1}{g\lambda} \cdot \frac{E_m}{1-\mu^2} \tag{21}$$

Vertical and Horizontal Stresses and Shears

The surface stresses in the vertical and horizontal planes were computed from the vertical and horizontal strains, corrected for cross-sensitivity, using the same similitude factor $K$, defined above, to make the transition from model to prototype scale and properties.

$$\sigma_0 = K(e_0 + \mu e_{90}) \tag{22}$$

$$\sigma_{90} = K(e_{90} + \mu e_0) \tag{23}$$

$$\tau_{0,90} = \frac{\sigma_0 - \sigma_{90}}{2} \tan 2\theta \tag{24}$$

## Normal Pressure Corrections

The great majority of strain gage rosettes was attached to the model at a free surface with no normal pressure against it. A small number of strain gages was applied to the upstream face at locations where the gage readings were affected by the pressure applied to the model. For these latter cases, a correction had to be applied for the effect of the normal stress.

Generalized Hooke's law can be written

$$e_x = \frac{1}{E}\left(\sigma_x - \mu\sigma_y - \mu\sigma_z\right) \tag{25}$$

and similarly for $e_y$ and $e_z$. When the above three equations are combined, the general expression for stress in three dimensions can be derived as

$$\sigma_x = \frac{E}{(1-2\mu)(1+\mu)}\left[(1-\mu)e_x + \mu(e_y+e_z)\right] \tag{26}$$

This expression can also be written in the following form:

$$\sigma_x = \frac{E}{1-\mu^2}(e_x+\mu e_y) + \frac{\mu}{1-\mu}\sigma_z \tag{27}$$

This expresses the stress on one axis in terms of strains on two axes and stress on a third axis. At a free surface, $\sigma_z = 0$, and equation (27) can be written as

$$\sigma_x = \frac{E}{1-\mu^2}(e_x+\mu e_y) \tag{28}$$

This last expression is the usual expression for determining the stress at a free surface from two normal strains at that surface. This was used throughout in determining stress from the strain meter measurements. For the few cases where a normal pressure $p$ existed at the surface, a correction $\frac{\mu}{1-\mu}\cdot p$ was added algebraically to the stress previously

determined from equations (19) and (20).

Live Load Stresses

The principal stresses caused by the full hydrostatic loading alone are shown on Figure 25. Stresses shown on this and all subsequent drawings are in psi at the prototype scale. The directions of the maximum principal stress on the outstanding legs of the main arch are nearly parallel to the direction of the applied load, except near the downstream edge of the arch, where they tend to follow the direction of the boundary. The maximum principal stress in the intrados is 395 psi compression, and a maximum tension of 130 psi is found at the base adjacent to the plug. In the actual dam, if constructed with a joint between the dam and the plug, this tension would disappear. On the extrados side, maximum compressions of 465 psi are found near the juncture of the riding buttress and the main arch. Maximum tension is likewise found along the base next to the plug, and is of the order of 225 psi. Along the downstream face of the outstanding leg of the arch, the maximum principal compressive stresses tend to follow the general line of arch, with some slight angular displacements. The magnitude of the principal stress increases fairly uniformly from top to bottom. The horizontal-vertical configuration of the principal stresses at the crown of the arch is to be expected from the symmetrical configuration of the dam and the symmetrical loading. However, in this case this orthogonal configuration was dictated by the type of strain gage group employed, which comprised single gages placed vertically and horizontally only. Compression at the upstream face and tension at the downstream face are found along the center line of the arch, in all cases. The vertical tension at the upstream face of the dam

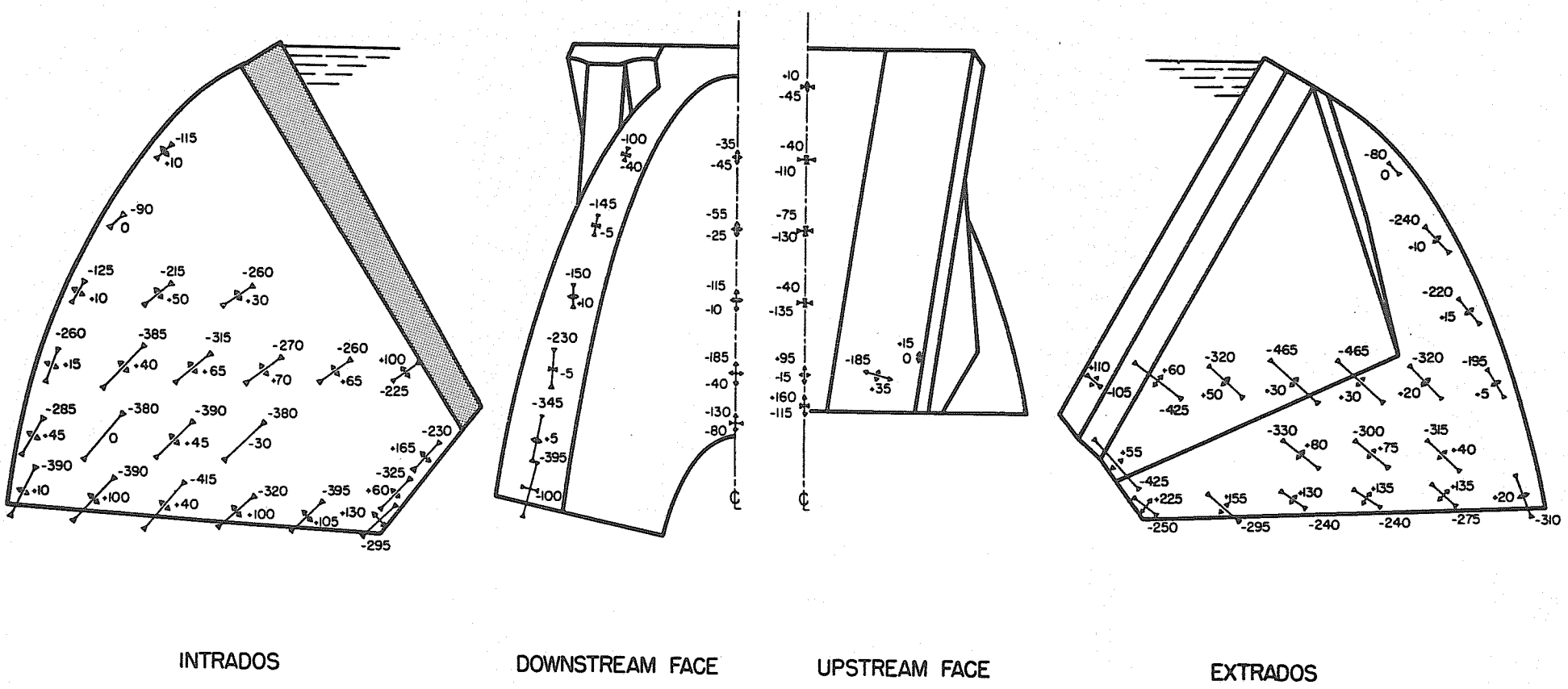


FIGURE 25 - DISTRIBUTION OF PRINCIPAL STRESSES DUE TO WATER LOAD

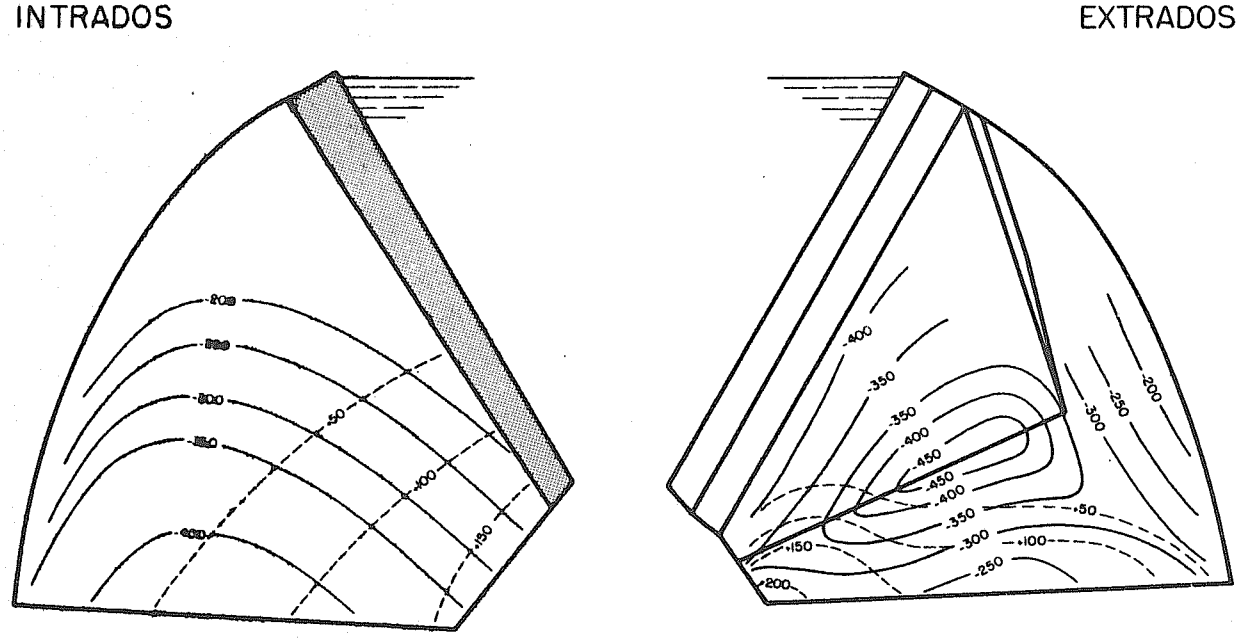


MAGNITUDE OF PRINCIPAL STRESSES

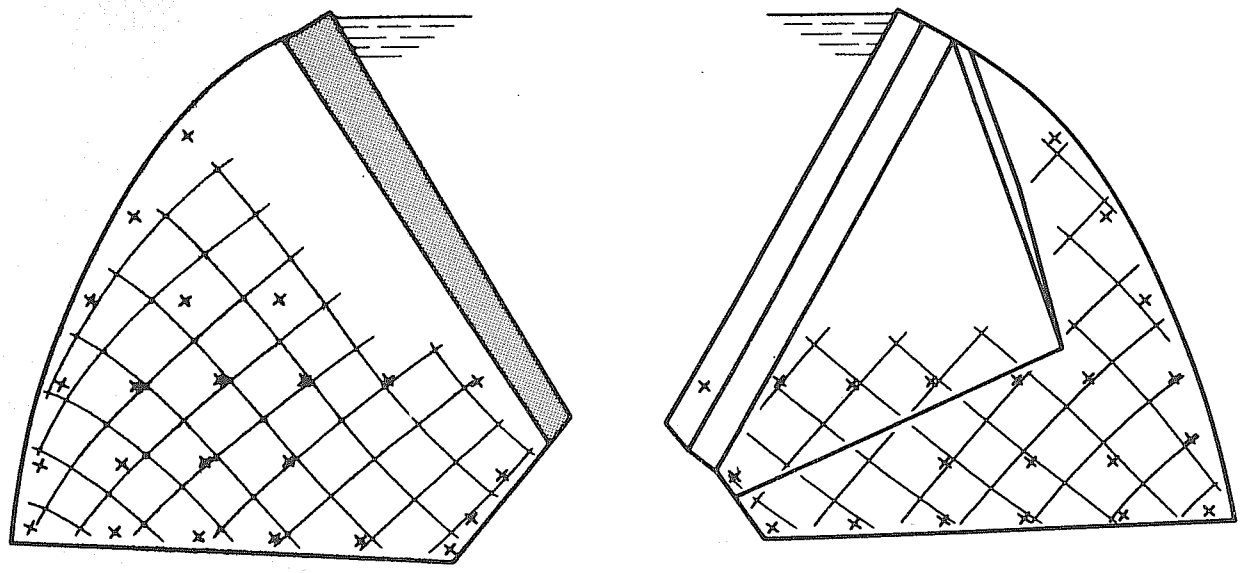

DIRECTION OF PRINCIPAL STRESSES

FIGURE 26 - MAGNITUDE AND DIRECTION OF PRINCIPAL STRESSES DUE TO WATER LOAD

near the location of the plug, again is probably due to bonding the dam to the plug.

The direction and magnitude of the principal stresses along the legs of the arch can be studied more easily in Figure 26, which is made from and interprets the data from the principal stress drawing shown previously. At the top of the figure, the magnitudes of the principal stresses are shown as stress contours, using a full line for compressive stresses and a dotted line for tensile stresses. At the bottom of the figure, the directions of the principal stresses are shown as an orthogonal net. The close association of the maximum principal compressive stresses is interesting. For the intrados, tensile stresses seem to be influenced mostly by the arch-plug boundary, while for the extrados, the arch-foundation joint also seems important.

Deflections due to Live Load

Because of the articulated nature of the arch and buttress dam, considerable interest was expressed in the relative displacements of the various units, as this entered directly into the design of joint seals. While there is no trouble, mathematically, in relating displacements of the model to the full scale deflections of the prototype, there is considerable difficulty in loading the model to correspond to the loading of the prototype, as far as deflection is concerned. The reason for this is that the load of the dam and the reservoir on the foundation rock causes strain within the foundation at great depth and over a large area. The surface deflections are the integrated effects of all the unit strains through a considerable volume of foundation material. Hence, to determine true deflections of the dam, a model much larger than that used for stress determination should be used. However, it is believed that the

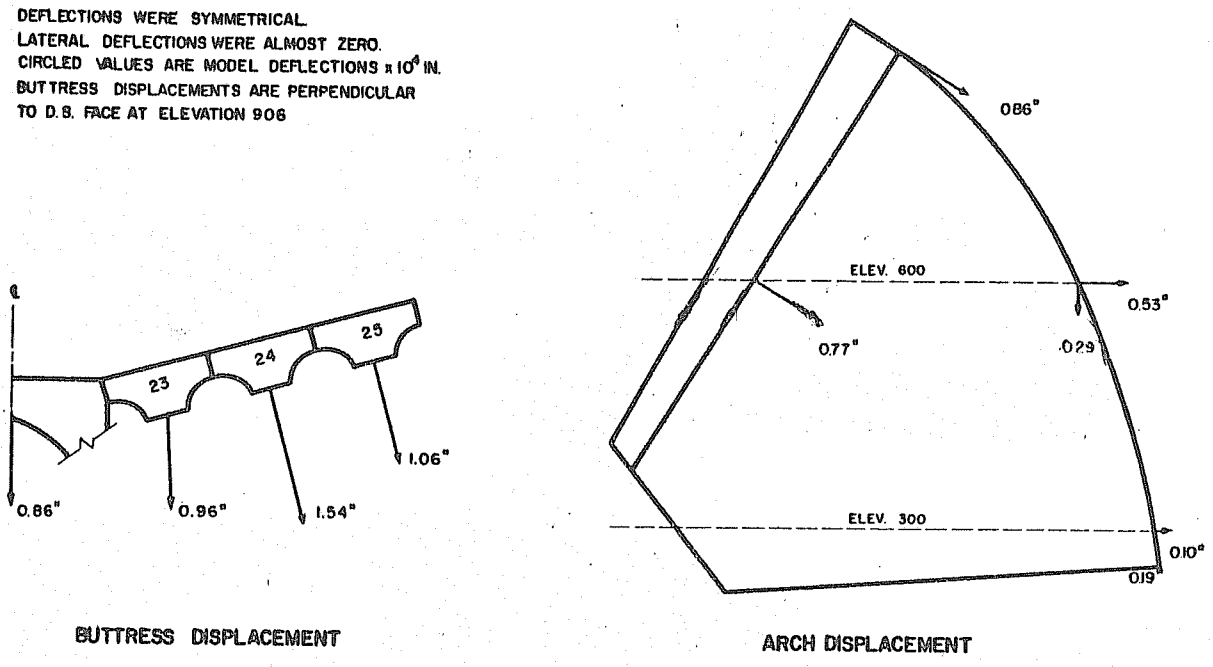


FIGURE 27 - DISPLACEMENTS DUE TO WATER LOAD

order of magnitude of the relative displacements of some of the structures can be determined with validity, since the more complete loading described above would affect the details more or less equally.

With these limitations in mind, deflections were measured at several points on the main arch and at the top of several buttresses in order to find their relative displacements. The results of these measurements are plotted on Figure 27. The arch displacement, and the displacements of buttresses 23 and 24 can be assumed representative. However, no interpretation should be made of the measured displacement of buttress 25, since it lacks the effect of the foundation loading of buttress 26.

It is seen that there will be a relative movement in the prototype of 0.1 inch between arch and riding buttress, and almost 0.6 inch between the stiff riding buttress, and the first full buttress.

# DETERMINATION OF STRESSES DUE TO DEAD LOAD

## Dead Load Tests

A number of possibilities were considered for determining the dead load stresses of the dam. Four experimental methods had been used by previous investigators: the centrifugal method, the immersion method, the applied load method, and the inversion method. A new method which has been termed the method of integration was devised and used for the Oroville Dam model test.

## Method of Applied Loads

The method of applied gravity loads dates from the very beginnings of model dam testing, having been used by Wilson and Gore[11] in their classic experiments in Great Britain reported in 1908. This is the method in use today at the ISMES Laboratories in Bergamo, Italy.[12] In this system, the effect of gravity loading in model dams is simulated by applying loads at a number of points in the structure in proportion to the weight of the material that each point controls. If the contact points are far enough apart so that stress concentrations from point loads disappear in the region in which strain gages are attached, this method can give usable results. Although this method held some attraction, difficulties in loading caused by the complicated shape of the arch and buttress dam were anticipated, and consideration of this method was set aside.

## Method of Inversion

The method of inversion has been used[13] for the determination of dead load stresses in model dams. In this method, a model of the structure is fabricated and fitted with strain gages. Zero strain readings are taken of the model in its upright position. The model is then inverted, giving a change

of loading twice that of gravity, and a second set of strain readings is taken. Strains in the model can be directly related to stresses in the prototype through use of similitude factors. Sensitivity of this test can be increased by decreasing the modulus of elasticity of the model material and by increasing its density.

A considerable amount of preliminary work was done to investigate the possibilities of the method of inversion for the arch and buttress dam. A special heavyweight plaster-barite mixture was devised, having a modulus of elasticity of 120,000 psi, and a density of 100 pounds per cubic foot. Using a 1:200 scale model, this should have given maximum strains of about 35 micro-inches per inch upon inversion of the model. This in turn would have given the distribution of stresses in the model due to gravity loads with an error of about 3 percent. However, upon making detailed designs of the experiment for the case of the arch and buttress dam, it was found that when this three-dimensional model was inverted, appreciable deflection developed in the foundation. This in turn applied rotations to the base of the arch, and thereby induced strains in the arch of a magnitude even greater than those to be expected from the gravity load itself. Consequently, further consideration of this method was abandoned.

Method of Immersion

Biot has shown[14] the analogy between the two-dimensional state of stress resulting from body-force loading such as the earth's gravitational pull on a structure, and the two-dimensional state of stress resulting from boundary loads. In this method, an accurately cut section of the gravity dam, together with part of its foundation, is inverted and lowered into a pool of mercury whose upper surface just touches the ground surface. Stresses in

various points in the slice are then related to corresponding stresses in the prototype dam by the use of Biot's equations which take into account the scale factor, and the relative densities of the immersing fluid and the material of the dam. This method has been used in the National Civil Engineering Laboratory in Lisbon[13] for finding the stress distribution in a slice of a gravity or of a buttress dam. Similar analogy has not been made for the three-dimensional state of stress. Since this was the case for the Oroville arch and buttress dam, no further consideration was given to this method.

Centrifugal Method

The principal of the centrifugal method for the experimental determination of dead load stresses is the substitution of centrifugal forces for gravitational forces by rotating the model in a centrifuge.[15] This method has been used with considerable success in the Engineering Materials Laboratory by Professor H. D. Eberhart in a two-dimensional photoelastic model of the cross sections of several gravity-type dams. The model was made of a sheet of photoelastic material and rotated at high speeds at elevated temperatures ($200^{\circ}$ F.) for several hours until it reached thermal equilibrium. Temperatures were then gradually reduced, while maintaining constant rotation, until room temperature was reached. When the model was removed, it had frozen within it a stress pattern resulting from the equivalent of an increased gravitational field which could then be analyzed by photoelastic methods.

In another experiment, Dr. A. J. Durelli,[16] Supervisor of the Stress Analysis Section of the Armour Research Foundation, Illinois Institute of Technology, went a little further toward the three-dimensional analysis. His experiment was concerned with the distribution of dead load stresses in a single buttress of a massive head buttress dam. In his experiment, a

model was cast using a photoelastic material of a single buttress together with part of the foundation. As soon as this casting had solidified, it was transferred to a centrifuge and rotated rapidly while curing progressed. At the end of the curing period, the model was removed with the stresses frozen within it. The model was then cut into two-dimensional slices, polished, and the stresses at various planes of the model determined photoelastically.

Both of these tests gave excellent solutions for the given, essentially two-dimensional, problem. However, extension of this to a model of the Oroville arch and buttress was not recommended because of certain serious limitations. The most serious was that for most plastic materials, Poisson's ratio is widely different from that of the dam. This means that three-dimensional models made of plastics would not be deformed in all respects like the prototype,, and that consequently the stresses would not be distributed in a plastic model like in the prototype. A second but less stringent limitation was that unlike gravity, centrifugal force is not constant throughout the model, but varies as the square of the radius from the center of rotation. Only by rotating a fairly small model on a long arm can the variation in the centrifugal field be held within feasible limits. A third limitation was that of size. Both centrifuges mentioned above were designed to handle fairly small models. Difficulties were anticipated in testing a model with the complexity of shape of the arch and buttress dam for Oroville in sizes that could be handled by centrifuges. For larger plaster models, the problem of recording indications from surface strain gages on a model rotating at high speed in a centrifuge is difficult. It was known that there were several very large centrifuges operating in this country on projects involving defense work, but inquiry was not made of their availability for testing of

a dam model. After this preliminary study, this method, too, was set aside.

Method of Integration

The four methods for dead load testing described previously-applied loads, inversion, immersion, and centrifuging-had one important common defect. Any test in which a completely constructed model is suddenly endowed in its entirety with weight does not in the slightest degree reflect the incremental manner in which weight is added to the prototype structure, and in which the structure gains its strength, and leads to erroneous conclusions as to the development of dead load stresses in the dam as construction proceeds. Field tests have shown the importance of the construction program in determining the distribution of stresses in a concrete dam.[13] This defect was particularly bothersome for the Oroville Dam model test, because questions had been raised as to the behavior of this structure at intermediate stages of construction. Hence, a method was devised by which the stresses could be determined not only in the complete structure, but also at various partial stages of completion following any given construction program. This method has been termed the "method of integration".

Since the dam is constructed in horizontal lifts, a model constructed in the same manner is stressed in its lower levels by material placed at higher elevations in a similar manner, and only that part of the structure that is present can take part in resisting the action of the imposed loads. If a similar method of construction were to be followed in the model, an awkward and time-consuming procedure would result. For each lift to be studied, molds would be assembled, plaster poured and dried, gages

attached, the model tested, and then the process would be repeated for as many times as the model were subdivided. Moreover, the response of the gages to the weight of model materials would be very slight, and hence the accuracy of the method would be low.

Exactly the same results could be secured with much greater convenience by reversing the process: starting with a complete model, with all gages in place, and finding the effect of removing material in successive layers. The advantages are obvious: the existing model with all its instrumentation attached can be used at the close of the live load testing period; there is no need to wait for curing of successive layers of plaster; the material will be homogeneous because it will be placed at once. The one drawback mentioned above, that of the response of the gages to small changes of loads due to the low weight of the model materials, is eliminated by a small change in testing procedure.

As finally developed, in the method of integration for the determination of dead load stresses, the model is cut down by increments of 100 feet in prototype elevation, leaving a horizontal surface representing the top of the lift. On this surface, a uniform load is applied, of a magnitude great enough to cause a well-defined response in all the strain gages on the model. By using similitude factors, this is then related to the effect on the prototype dam of adding one foot of concrete at that elevation.

Thus, for every gage location there is available a record showing the stresses induced by adding a foot of concrete at successive elevations. This is a continuous function which can be integrated graphically or numerically to indicate the effect of successive stages of construction,

including the dead load stresses in the complete dam. Thus, critical stages in the construction when dead load stresses are a maximum which exceed the stress state in the complete dam will be indicated by study of the graph of stress versus height of dam.

Similitude Factors

The general considerations that apply to the derivation of the similitude factors used in the method of integration for determining dead load stresses in dams are shown on Figure 28. As shown, the dam is to be constructed in horizontal lifts to a final elevation H. At an intermediate stage of construction, it will have reached elevation h. In testing, the model dam is cut down by stages to some elevation y. The similitude problem is to find the effect of the increment of height dy on the strains and stresses at location $x_o$, $y_o$.

From equations (3) and (5), we can write

$$\frac{\sigma_m}{\sigma_p} = \frac{\gamma_m L_m}{\gamma_p L_p} = \frac{E_m e_m}{E_p e_p} \tag{29}$$

Consider a uniform stress of $W_{ym}$ to be applied to the model at elevation y. If the dam is correspondingly increased in height at elevation y by the increment dy, then this will apply a stress $\gamma_p dy$ at y.

Since both model and prototype are geometrically similar, and have linear elastic properties, the ratio of the stress applied to the model to the stress applied to the prototype will be

$$\frac{W_{ym}}{\gamma_p dy} = \frac{E_m}{E_p} \cdot \frac{e_{ym}}{de_{yp}} \tag{30}$$

Thus, the incremental strain in the prototype caused by the incremental loading $\gamma_p\, dy$ at y will be

$$de_{yp} = \frac{E_m}{E_p} \cdot \frac{\gamma_p}{W_{ym}}\, e_{ym}\, dy \qquad (31)$$

If follows that the increment of stress in the prototype due to this incremental loading is

$$d\sigma_{yp} = E_p\, de_{yp} = E_m \frac{\gamma_p}{W_{ym}} \cdot e_{ym}\, dy \qquad (32)$$

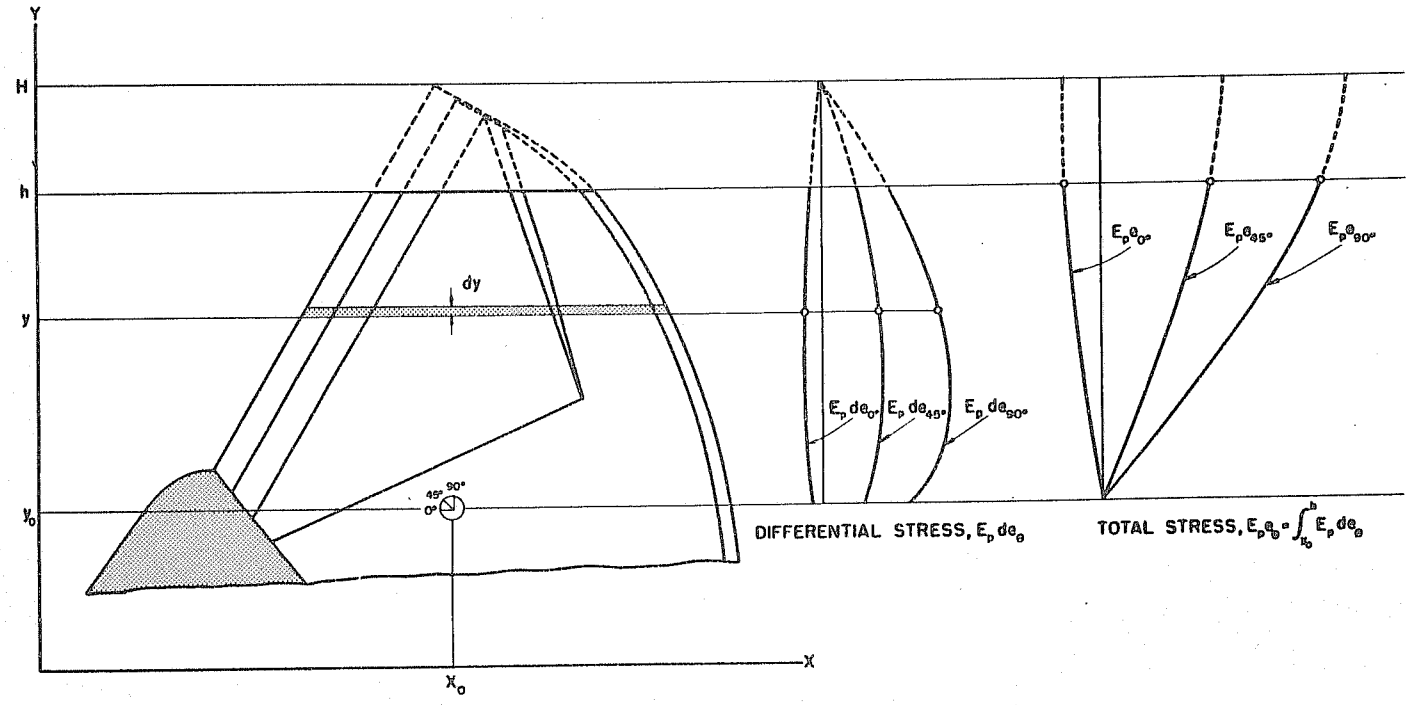


FIGURE 28 - NOTATION FOR METHOD OF INTEGRATION FOR DEAD LOAD STRESSES

Thus the stress in the prototype due to the dead load when the dam is constructed to elevation h is the integrated effect of all the

elemental loadings at y up to elevation h, or

$$\sigma_{hp} = \int_{y_o}^{h} d\sigma_{yp} = E_m \gamma_p \int_{y_o}^{h} \frac{e_{ym}}{W_{ym}} dy \qquad (33)$$

and similarly for dead load stress of the complete dam

$$\sigma_{Hp} = E_m \gamma_p \int_{y_o}^{H} \frac{e_{ym}}{W_{ym}} dy \qquad (34)$$

It will be noted that the model loading factor $W_{ym}$ is taken within the integral because it may vary with each elevation tested, and is thus a function of y.

In a typical test, the model was loaded uniformly with 1500 pounds of lead bricks applied to an area of 250 square inches. Thus, the increment of stress in the prototype corresponding to adding an increment of one foot of concrete to the dam was

$$d\sigma = \frac{E_m \gamma_p}{W_{ym}} e_{ym}\, dy = \frac{240{,}000 \times 150 \times 1}{\frac{1{,}500 \times 144}{250}} e_{ym}$$

$$d\sigma = .044\, e_{ym}$$

where strains are measured in micro-inches per inch.

In testing a model, the model is cut down to definite elevations y convenient for analysis, and loaded heavily enough to give a well defined response. Using the similitude factors contained in equation (32), curves of differential stress versus loading at any elevation y can be plotted, as shown on Figure 28.

The initial value of the curves cannot be determined experimentally, because of physical limitations, and it is necessary to compute the stresses at the gage elevation due to the effect of loading at that elevation. By

Hooke's law

$$d\sigma_{90} = \frac{E_p}{1-\mu^2}\left(de_{90}+\mu\, de_0\right) \tag{35}$$

But $d\sigma_{90}$ is the applied load, equal to the density of the concrete of 158 pounds per cubic foot or =1.10 psi per foot of concrete. If $\mu$ is equal to 0.24, equation (35) reduces to

$$E_p\, de_{90} = -1.04 - 0.24\, E_p\, de_0 \tag{36}$$

Since the direction of this stress is known,

$$E_p\, de_{90} + E_p\, de_0 = 2E_p\, de_{45} \tag{37}$$

For any rosette, equations (36) and (37) must be satisfied and all three strains must be consistent with the strains developed at adjacent points y .

With the differential stress function completely defined, the stress at $y_o$ due to construction to height h can be found by graphical or numerical integration of the curves representing equation (33).

The principal stresses for any stage of construction can then be calculated in the usual fashion from the stresses along the individual directions shown on the curves for $E_p e_\theta$.

Test Procedures

In the gravity loading test, a uniformly distributed load was applied to a series of horizontal surfaces. This uniform load was approximated with lead bricks. At each elevation to be tested, the area of the exposed surface was measured, and divided by a planimeter into a number of equal smaller areas. The center of gravity of each of these small areas was then found, and the position for each lead brick carefully drawn, so that the weights were equally distributed. Between 50 and 70 lead bricks, each weighing

26 pounds, were used for each load test. Thus the model supported nearly a ton of dead weight at various stages of the testing. The cut model with its dead weight in place is shown in Figure 29. When a number of tiers of lead weights had to be used, sheets of paper were interposed between layers to increase the stability of the mass.

The test cycle for gravity loading was similar to that for hydrostatic loading. A uniform load was applied on 6 different horizontal sections, cut at the even 100 foot elevations throughout the height of the model. Three identical tests were conducted at each elevation. A representative test cycle for these tests was as follows:

| | |
|---|---|
| 0 - 30 minutes | Model loaded |
| 30 - 40 minutes | Model allowed to creep |
| 40 - 50 minutes | Gages read twice |
| 50 - 52 minutes | Model unloaded |
| 52 - 60 minutes | Model allowed to rebound |
| 60 - 70 minutes | Gages read twice |

Since the model progressively reduced in height during testing, the number of gages read for any test elevation was likewise reduced. Therefore, the time necessary to read the gages differed at each test elevation. It was found that the model strains were sensitive to the exact placement of the uniform load, but an average of three tests tended to eliminate this error.

Dead Load Stresses

Figure 30 shows the direction and magnitude of the principal dead load stresses for the completed structure. It can be seen that for the intrados, the principal compressive stresses increase gradually from top to bottom and that the directions are parallel to the boundaries upstream

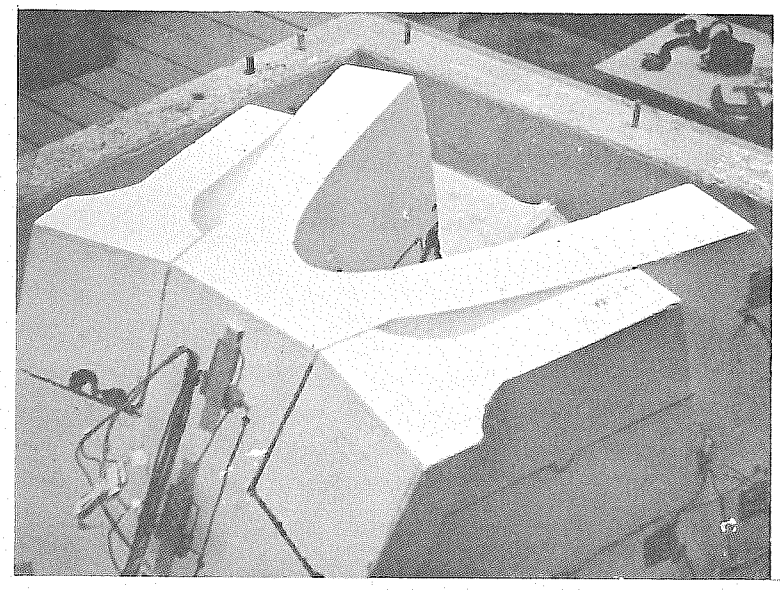

A - CUT MODEL READY FOR LOADING. LOCATION OF LEAD BRICKS MARKED.

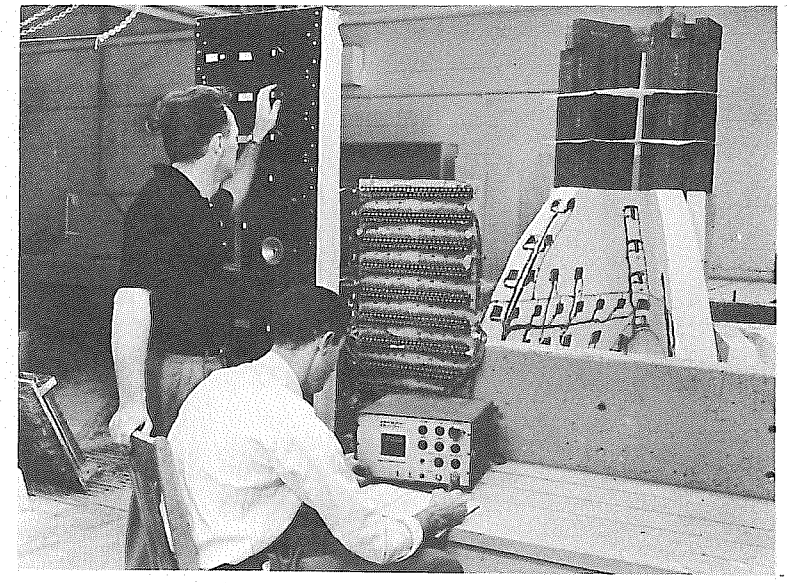

B - STRAINS BEING RECORDED ON MODEL LOADED WITH ONE TON OF LEAD BRICKS

FIGURE 29 - SET UP FOR DEAD LOAD TEST BY METHOD OF INTEGRATION

and downstream, varying gradually from the upstream to the downstream face. For the extrados, the discontinuity of the riding buttress is evidenced in higher compressive stresses near its lower boundary. Along the outstanding edge of the arch, the maximum compressive stresses increase from top to bottom. The considerable variation of the direction of these maximum principal stresses from the center line of the outstanding leg can be explained in part by a twisting, shearing action at this boundary. Fairly high tensile stresses are found near the boundary of the arch and plug for both the extrados and intrados, indicating that bonding these two structures together in the model served to develop considerable tension at the interface.

At the center line of the arch, fairly high compressive stresses are found everywhere on the intrados. However, for the extrados, while the vertical stresses are compressive and of somewhat less magnitude than for the intrados, fairly high horizontal tensile stresses are found to exist. The maximum tensile stress at the center line of 180 psi is found at elevation 650.

Magnitudes and directions of the dead load stresses for the completed dam are developed further in Figure 31. This shows that the maximum compressive stresses in the intrados are associated with the foundation, while those for the extrados are found at the lower boundary of the riding buttress. The maximum tensile stresses for the intrados are found near the lower boundary of the arch-plug connection. Maximum tensile stresses for the extrados, however, are found near the downstream end of the arch leg, and as will be shown later, are truly construction stresses. The gradual change in inclination of these principal stresses from the downstream face

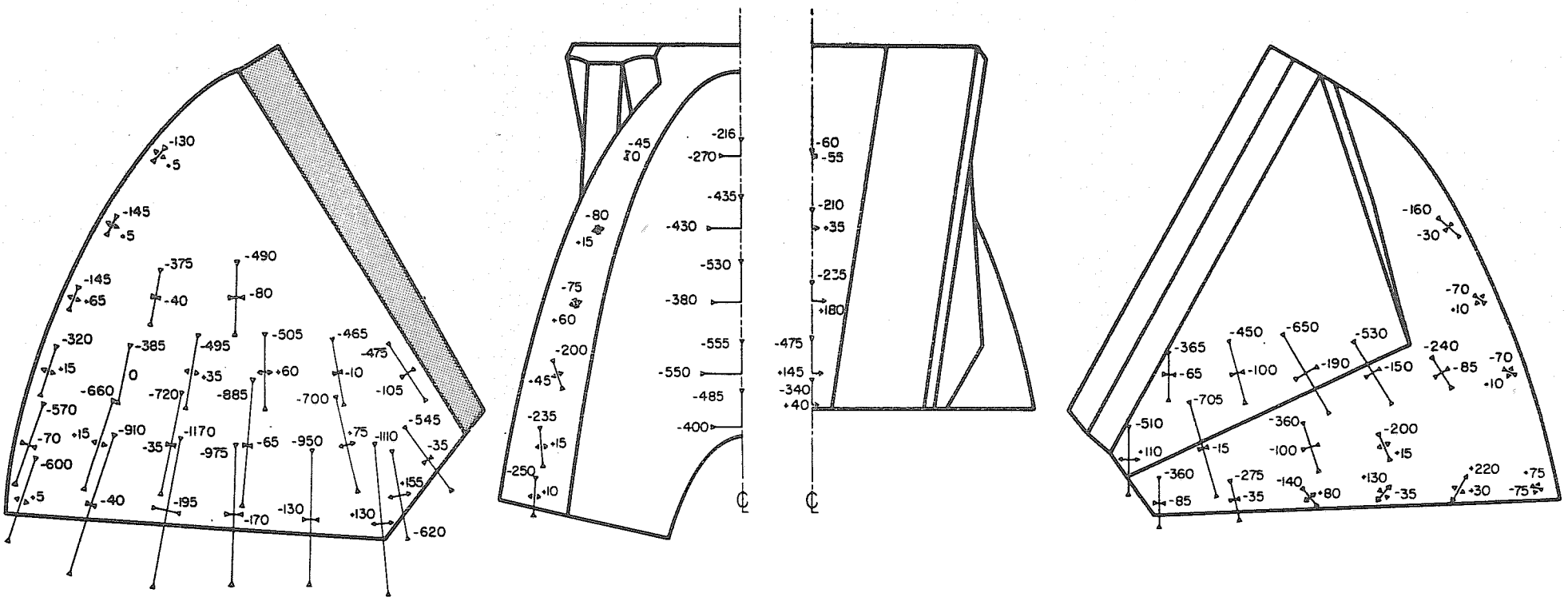


FIGURE 30 - DISTRIBUTION OF PRINCIPAL STRESSES DUE TO DEAD LOAD

INTRADOS

EXTRADOS

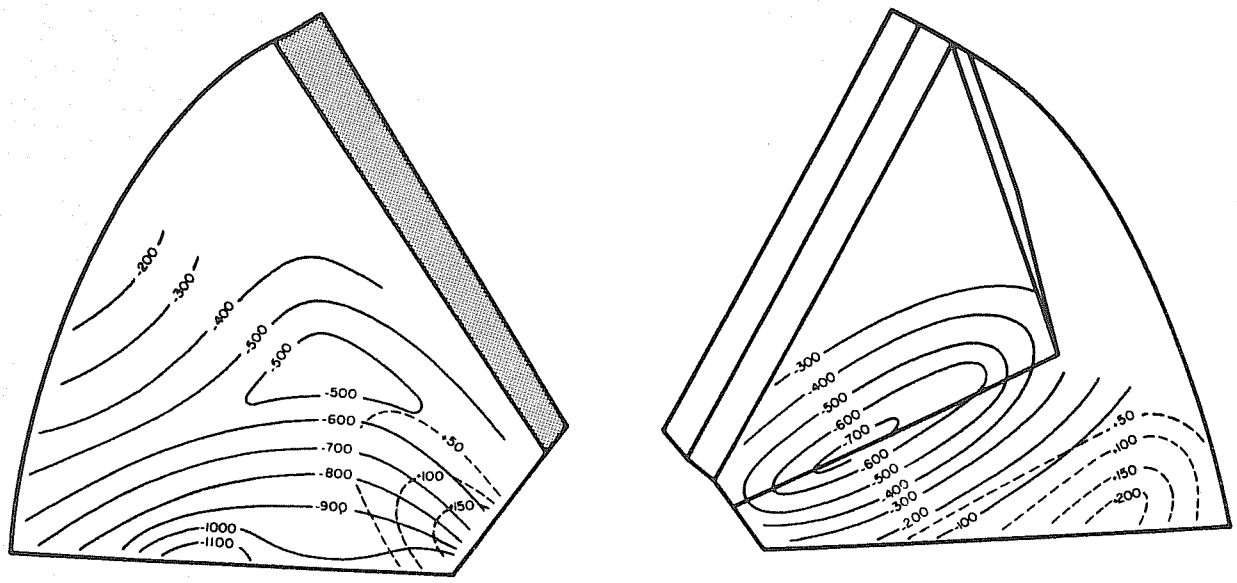


MAGNITUDE OF PRINCIPAL STRESSES

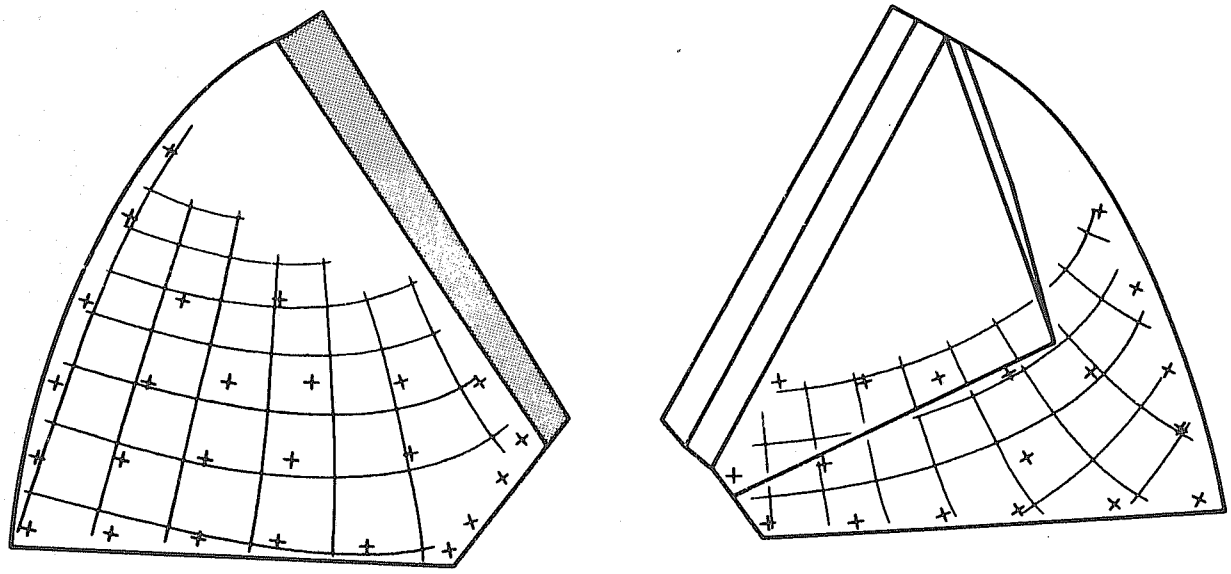

DIRECTION OF PRINCIPAL STRESSES

FIGURE 31 - MAGNITUDE AND DIRECTION OF PRINCIPAL STRESSES DUE TO DEAD LOAD

to the upstream face is well shown in the stress trajectories drawn for the intrados. For the extrados, however, the directions of maximum principal stresses do not parallel the boundaries, but intersect nearly every boundary at 45°.

Considerable speculation was raised as to the behavior of the main arch during construction. A glance at the downstream view of the dam shows the convergence of the sides of the arch as construction proceeds upwards, to the point where they overhang the base. In Figure 32 some light is shed on the gradual development of the principal stresses for the intrados and extrados at the base as construction proceeds upwards. In this figure, the intrados of the dam is shown at the left and the extrados at the right. Near the bottom foundation line, circles show the locations for which principal stresses were computed. Directly above each circle, and at elevations corresponding to the top elevation of the concrete at any particular time, the drawing shows the magnitude and direction of the principal stresses when concrete had reached that elevation. For instance, for the farthest downstream location at the intrados, the maximum compressive principal stress was 135 psi when the dam was concreted to elevation 400, 520 psi when construction had reached 700, and 600 psi when the dam was completed. It can be noted that the directions of the principal stress for the intrados change very little during the construction of the dam, and that the magnitudes increase gradually as construction progresses. However, for the extrados, there is considerable change in the direction of the principal stresses as construction proceeds.

A slightly different view of the gradual development of the vertical stress at the intrados and extrados is given in Figure 33. Here, superposed on an outline drawing of the intrados and extrados, are curves indicating the

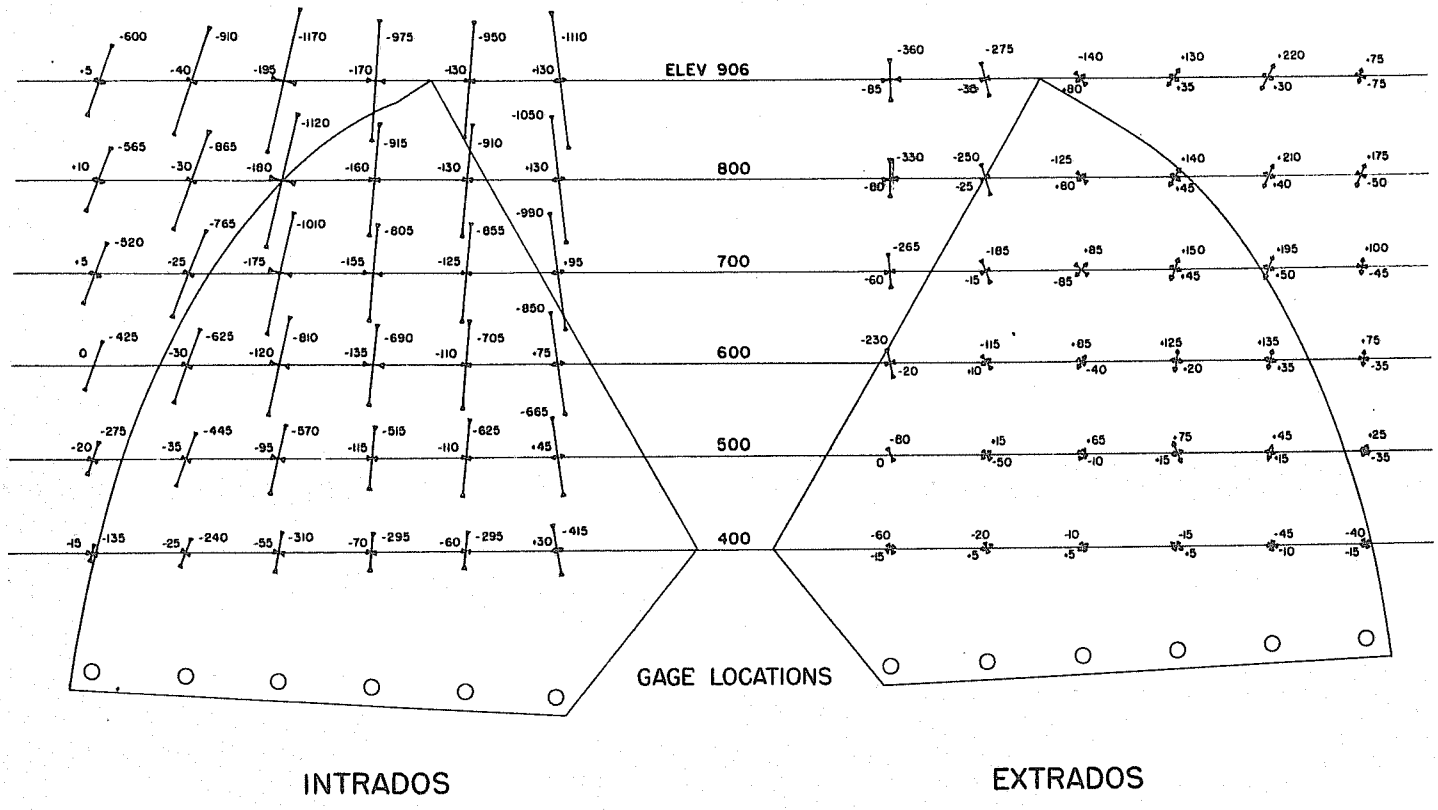


FIGURE 32 - PRINCIPAL STRESSES AT BASE DUE TO DEAD LOAD AT VARIOUS STAGES OF CONSTRUCTION

magnitude and sense of the vertical stress at any stage of construction, for various locations at elevation 450 and along the base. Thus, the extreme left-hand curve at the bottom of the figure indicates the gradual increase of compressive vertical stress at the downstream end of the intrados from 0 to 400 psi, as construction of the dam proceeds from the base to elevation 906. At all locations at the base of the intrados, the vertical stress is compressive. The figure also indicates that the compression increases fairly rapidly until construction reaches about elevation 700, and after that the increase is very slight. However, for the extrados, the curves indicate that the vertical stress is compressive at the upstream locations, tensile

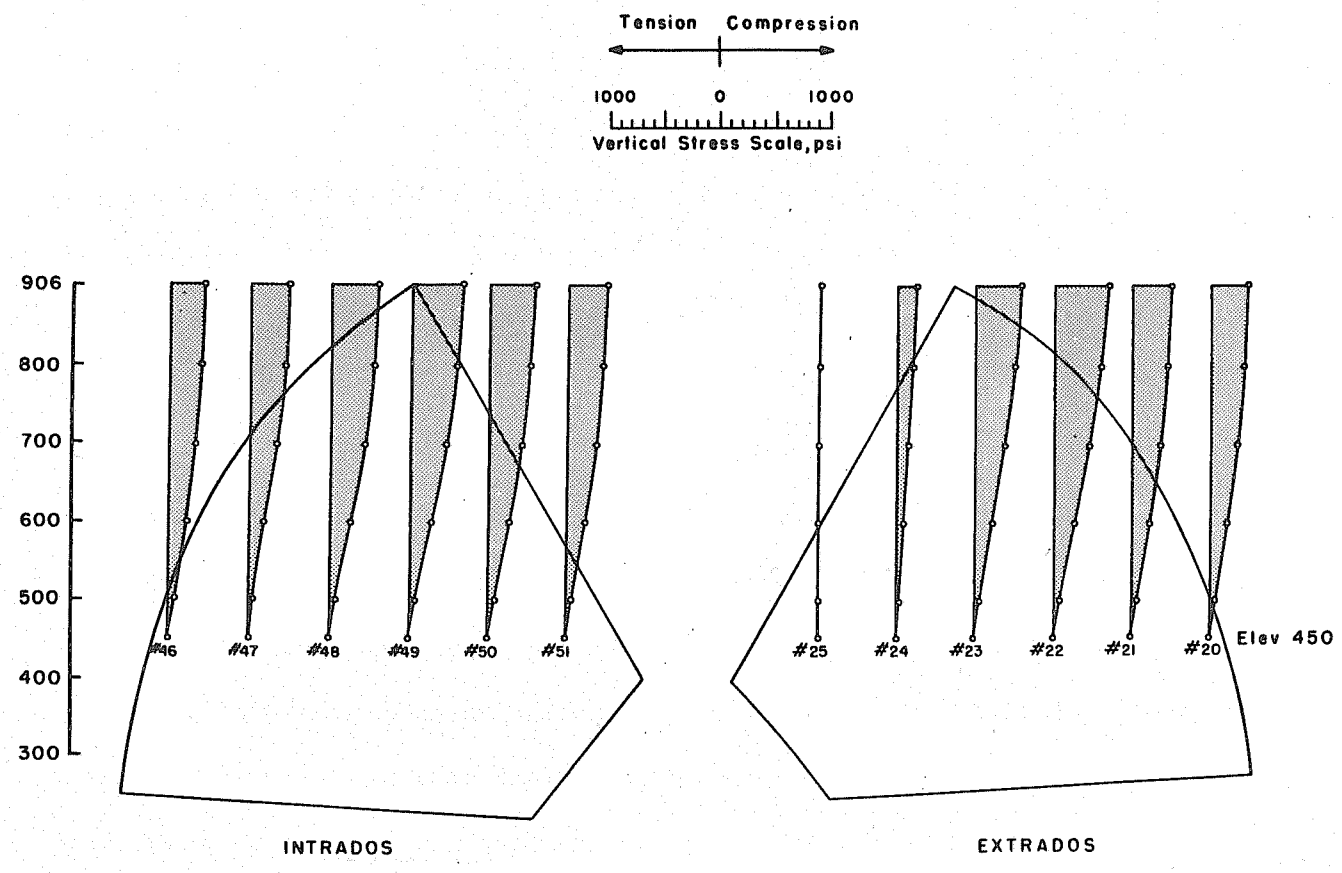


A - VERTICAL STRESS AT ELEVATION 450

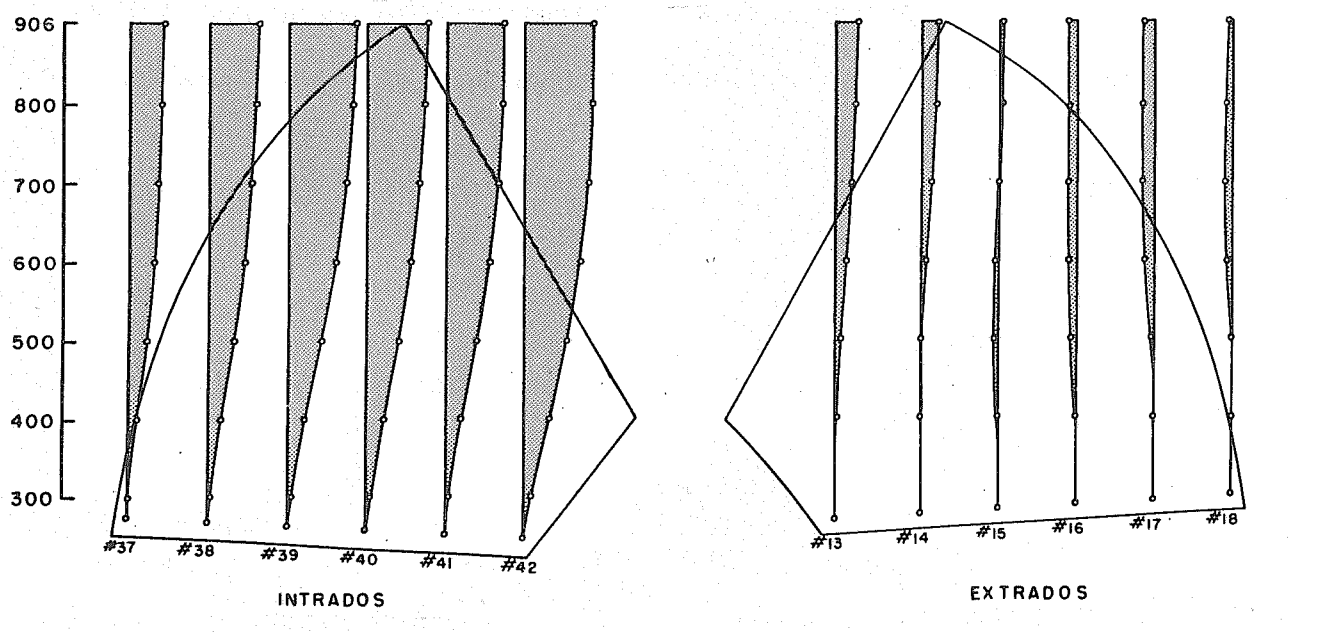


B - VERTICAL STRESS AT BASE

FIGURE 33 - VERTICAL DEAD LOAD STRESSES AT VARIOUS STAGES OF CONSTRUCTION

stresses are found in the completed dam. Hence, the stresses shown in Figure 34 are those for the completed dam. This figure is a three-dimensional space plot of the observed stresses at the base of the dam. Near the downstream end, considerable tensile stress exists, penetrating for a very short distance inside the dam. In an attempt to evaluate the stability of this section, it was assumed that wherever tensile stresses existed, concrete could crack all the way back to zero stress. It was further assumed, that if the concrete did crack, that the moment and thrust that caused the stresses shown in Figure 34A would remain, without redistribution to the remainder of the structure, which is conservative for the base. Thus, Figure 34B is derived, on which the extent of the cracked section is shown shaded. Since for every cross-section the resultant falls within the base of the dam, it can thus be concluded that the arch is everywhere stable. This is not to be construed to mean that the method of construction in horizontal layers is best for this type of dam: another method involving sloped pours might very well result in considerably lessened tensile stress during construction.

## DETERMINATION OF STRESSES DUE TO COMBINED LOADS

### Computation of Stresses due to Combined Loads

To find the stresses in the dam due to the combined effects of dead load and water load, the strains at every gage location were determined at the prototype scale on each strain gage axis and added algebraically. The dead load strains were already at the prototype scale. Strains for the water load had been determined previously at the model scale, and were amplified to the prototype scale by multiplying by the similitude factor
The principal strains and principal stresses were then computed from the combined prototype strains.

### Combined Live and Dead Load Stresses

The principal stresses due to the combination of water load and dead load are shown plotted in Figure 35. As might be expected, for the intrados, where both the live and dead load stresses were in practically the same direction and were all compressive, combination of live and dead load stresses leads to high principal stresses, the maximum being 1490 psi compression near the center of the base. The tensions found separately under live and dead load were considerably reduced, the maximum tension being of the order of 45 psi near the foundation-plug junction. Considerable tensile stresses are still found at the extrados along the foundation line, and at nearly 45° to the horizontal. This serves to indicate the very high shears that exist in this location. Some tension is still found at the center line on the upstream face at and below elevation 650.

Magnitudes and directions of the principal stresses are shown in Figure 36. The regions of maximum compressive stress are clearly shown to be along the base for the intrados, and at the lower boundary of

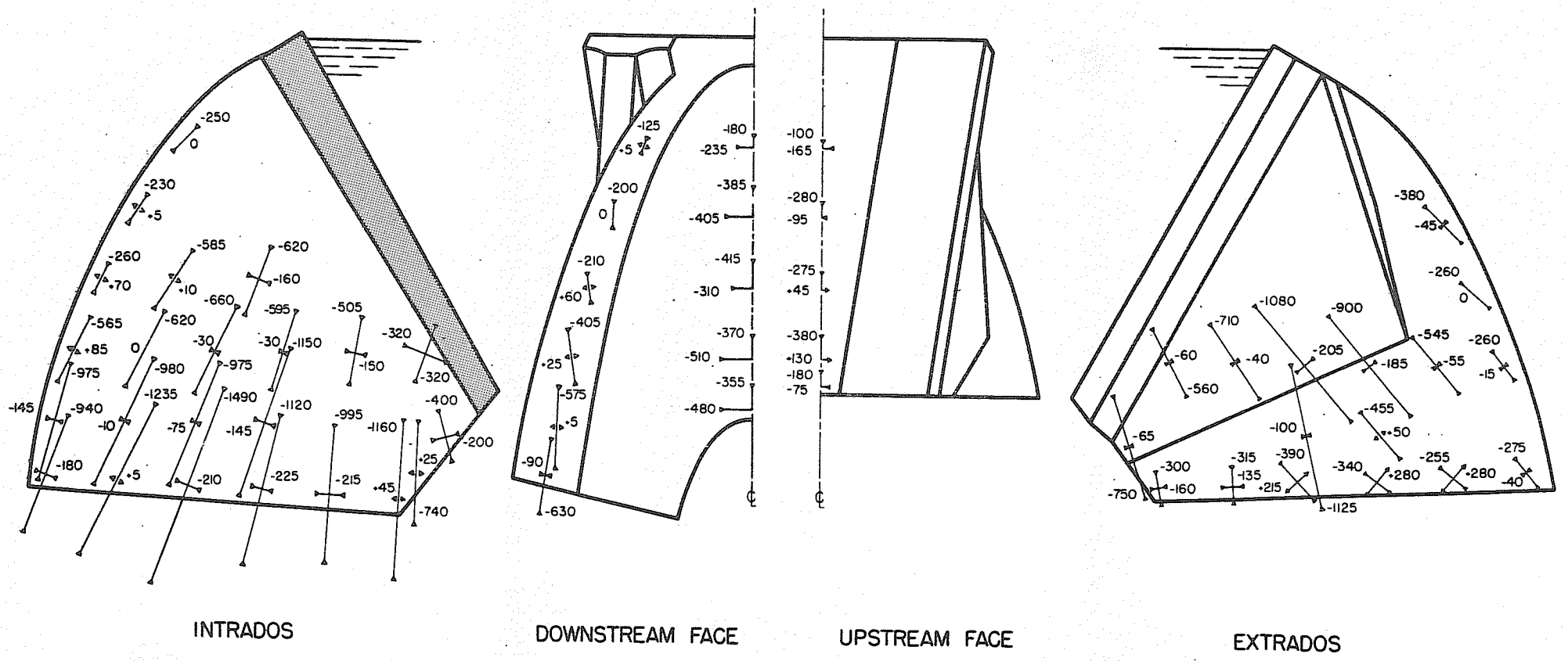


FIGURE 35 - DISTRIBUTION OF PRINCIPAL STRESSES DUE TO LIVE AND DEAD LOADS COMBINED

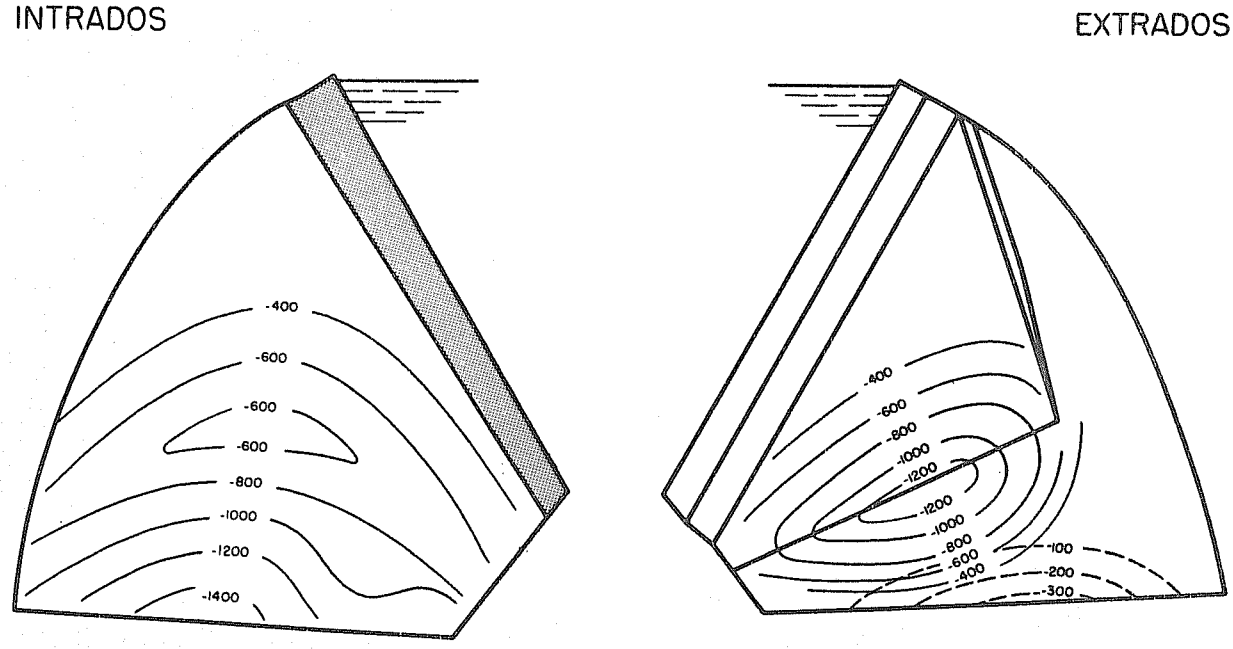


MAGNITUDE OF PRINCIPAL STRESSES

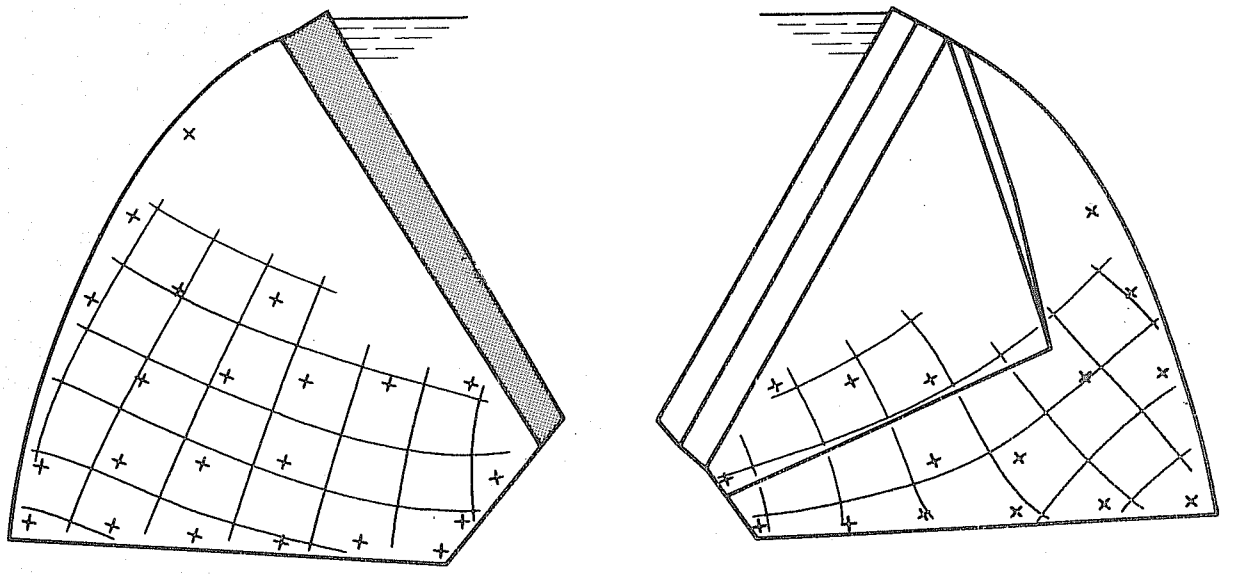

DIRECTION OF PRINCIPAL STRESSES

FIGURE 36 - MAGNITUDE AND DIRECTION OF PRINCIPAL STRESSES DUE TO LIVE AND DEAD LOADS COMBINED

the buttress for the extrados. Tension great enough to crack concrete is shown at the downstream end of the extrados along the foundation. Again, the regular array of the isostatic lines is clearly shown.

# DISCUSSION

## Validity of Results

In experimental analysis, the question of the reliability of the results is most complicated. At every step of the investigation, there is the possibility of failing to duplicate, to some degree, some peculiarity of the prototype. This consideration is in addition to the problem of maintaining accuracy in the actual measurements themselves. The problem of what can be used as a standard of comparison for the results is almost as vexatious.

Most investigations have compared the results of the experimental investigation with those obtained by some analytical procedure, with the idea that the truth may lie somewhere in the neighborhood of the two results if they are at all comparable. If the results from the experimental analysis differ sharply from those made by some analysis, based for instance on the theory of elasticity, which then is the more nearly correct?

If some absolute truth can be used as the basis of comparison, then the validity of the results rests on more solid ground. Such an absolute basis is found in a check of the statics of the experiment.

To summarize, a comparison of experimental with theoretical results is a comparison of assumptions; a static check is an absolute test of technique. In the Oroville Dam model tests, both comparisons have been made: comparison with elastic theory, and a statics check.

## Comparison of Experimental and Theoretical Results

The basis of the analytical procedures used by the designers to evaluate the stresses in the central arch of the dam is a method of inclined arches.[17] Briefly described, the method consists of sampling the behavior

of the volume by six curved inclined arches, starting normal to the upstream face at the even 100 foot elevations, and curving downward in accordance with the contribution of the gravity load in each arch. In each curved section thus described, a parabolic arch is used to carry the thrust of the water load combined with the gravity load to the foundation. In effect, the analysis presumes that each elemental arch follows a line of principal stress: thus the direction of principal stress is fixed by the direction assumed for the arch. Moreover, for this analysis the second principal stress is assumed zero.

Figure 37A shows, as dotted vectors, the magnitude of the principal stresses under combined dead plus water loads computed at the base of the dam by this theoretical analysis. Since measurements on the model were made a finite distance above the base, the principal compressive stresses determined experimentally are plotted as the full-line vectors just above the base. A study of the relative inclination of these vectors indicates that considerably more shear is transferred across the base at the downstream end of the extrados in the model than was anticipated in the theoretical analysis. For the extrados, the magnitudes of the stresses are comparable. However, for the intrados, while the directions of the principal stresses are comparable, the distribution of stress is quite different. This can be followed more easily on Figure 37B.

On Figure 37B, the magnitudes of the principal compressive stresses determined experimentally and by the theoretical analysis have been plotted, without regard to direction. The close comparison of these stresses for the extrados is striking. And while the distribution of the principal stresses for the intrados is quite different for the two methods of analysis, it can be seen by judging all four curves together, that the resultant compressive

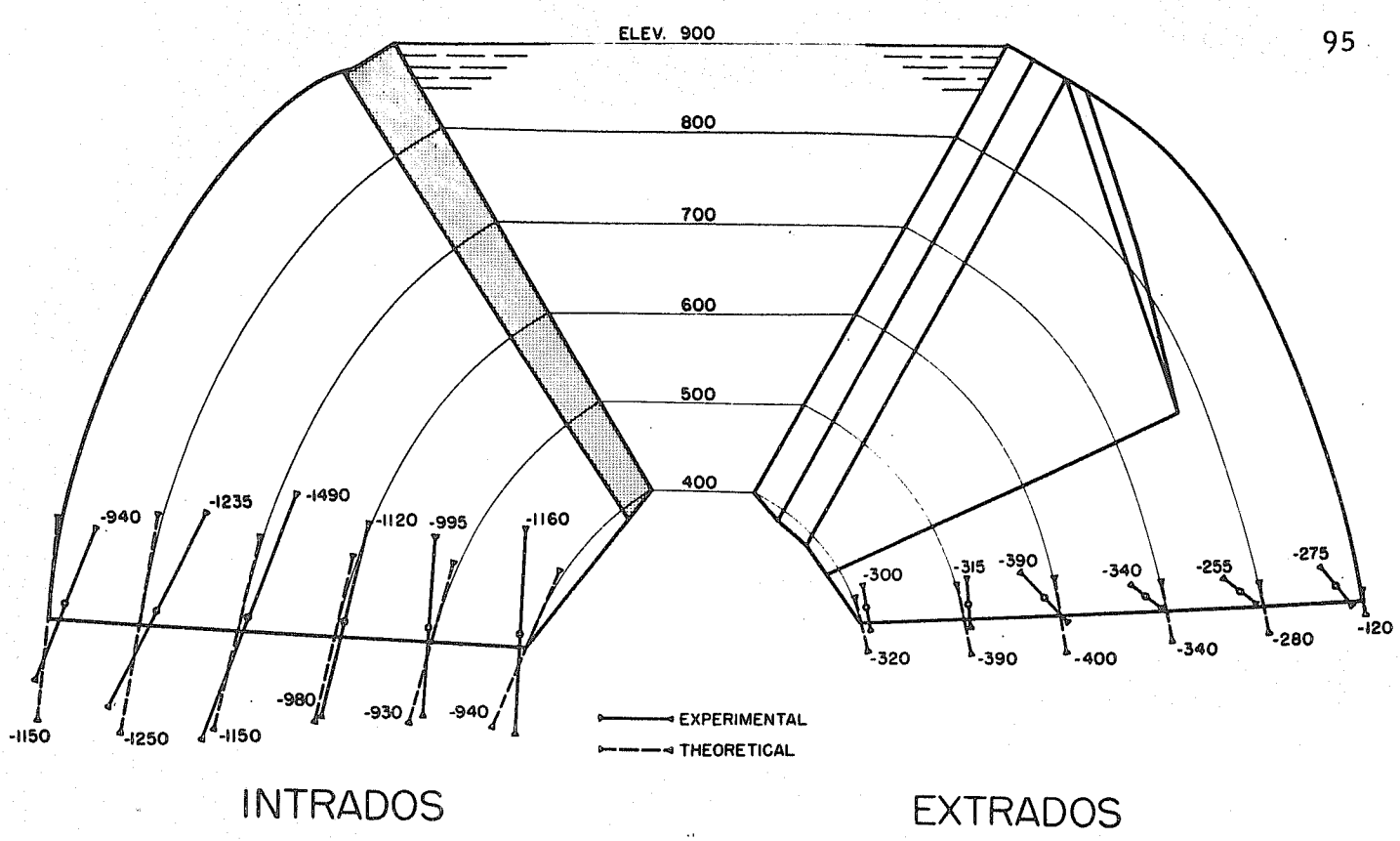


A - PRINCIPAL STRESSES AT BASE OF DAM

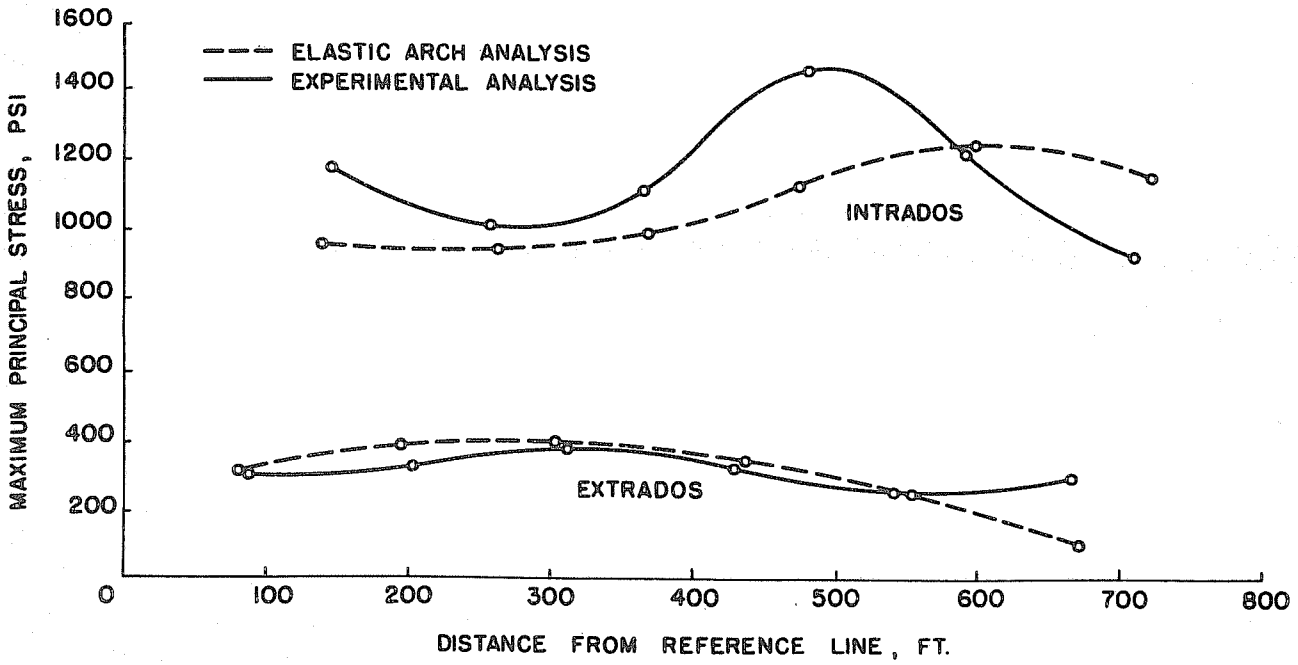


B - MAGNITUDE OF FIRST PRINCIPAL STRESS

FIGURE 37 - COMPARISON OF STRESSES DETERMINED BY ELASTIC ARCH AND EXPERIMENTAL ANALYSES

forces at the base by the two methods will be comparable within a few percent.

However, this apparent agreement is only superficial, since the comparison does not take into account the tensile stresses that were found in the model. By the very nature of the theoretical analysis, based on independent inclined arches, no tensile stresses were presumed to exist normal to the plane of the arch. Referring to Figure 35, it can be seen that a region of tensile stress high enough to crack concrete, is found at the base of the model in the downstream portion of the extrados. This points up one of the weaknesses of the numerical analysis: the nature of the solution is almost dictated by the assumptions made in the analysis. Conversely, the strength of the experimental analysis is that the model will behave naturally, reflecting in its behavior whatever program of construction or loading is applied to it.

Statics Check

The philosophy of a statics check is simple: at a chosen section, the resultant force imposed on the model must be balanced by the resultant of the stresses measured in the model. In choosing the section for making this balance, precautions must be observed so that the forces can be well defined. Thus, the statics check was not made at the base, because here the amount of load taken across the open joint between the plug and arch in the actual dam was open to question. The section chosen for the check was a horizontal section at elevation 450, fifty feet above the plug. Here a complete array of gages was attached, so that the distribtuion of stress could be defined accurately.

The surface of the dam, on which stress have been computed, lies in general at angles to the horizontal surface and to the main up-and-

downstream axis of the dam. It is easiest to use the horizontal plane for a reference for the resultant dead load, and the vertical plane containing the center line of the dam for a reference for the resultant water loads.

Consider the element shown in Figure 38 to represent a portion of the surface on which stresses have been determined. The vertical axis of

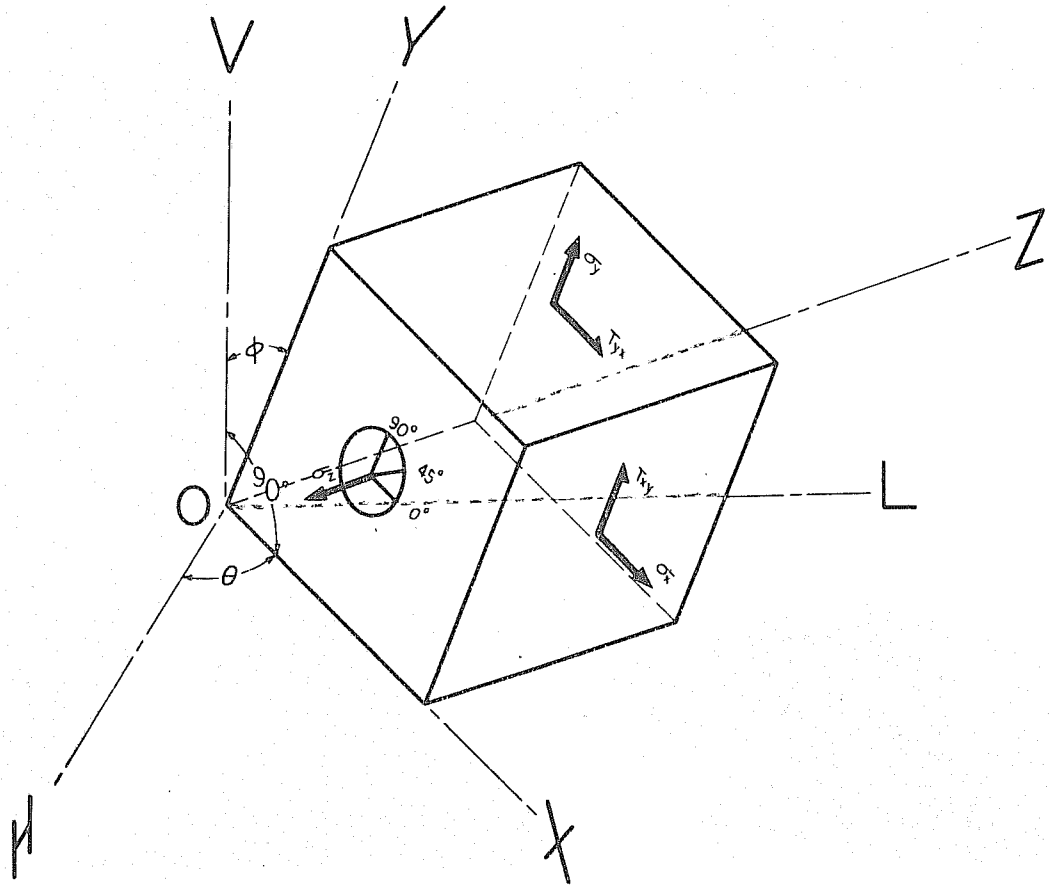


FIGURE 38 - ELEMENT FOR TRANSFORMATION OF SURFACE STRESSES

the dam is denoted V. The H axis is a horizontal axis parallel to the up- and-downstream center line of the dam. The L axis is the orthogonal horizontal axis, parallel to the upstream face of the dam. As an aid to orientation, a strain gage rosette is shown in the surface of the element. The element itself has axes X, Y, and Z. The X-axis lies in the horizontal plane at angle Θ with the H-axis. The element is rotated about the X-axis

by the angle $\phi$. The directions of the stress components $\sigma_x$ and $\sigma_y$ correspond to the directions of the rosette axes $e_0$ and $e_{90}$.

Now if $\sigma_x$, $\sigma_y$, and $\tau_{xy}$ are the measured surface stresses, and $\sigma_z$ is the hydrostatic pressure at the gage point, the stresses $\sigma_v$ and $\tau_{hv}$ on a horizontal section can be calculated using the following equations for the stress transformation:

$$\sigma_v = \sigma_y \cos^2\theta + \sigma_z \sin^2\phi \tag{38}$$

$$\tau_{vh} = \tau_{xy} \cos\phi \cos\theta + (\sigma_y + \sigma_z) \cos\phi \sin\phi \sin\theta \tag{39}$$

Stresses normal and parallel to the horizontal section at elevation 450 for the gravity load and the full water load are shown on Figure 39, plotted above one leg of the arch. At this distance above the base, it can be assumed that the stress distribution through the dam is linear, as shown. It should be noted that the shears are shown parallel to the up-and-downstream axis of the dam, rather than parallel to the general direction of the arch surface. The resultant normal and shear forces were then computed from these distributed stresses for the entire central section of the arch with its two riding buttresses, as shown in Table 1. These values are also shown in Figure 40, plotted below the section at elevation 450, since these are resisting forces.

The resultant of the actual hydrostatic forces applied to the central arch and its two riding buttresses above elevation 450 was calculated directly, and its position and line of action shown in Figure 40. The geometrical

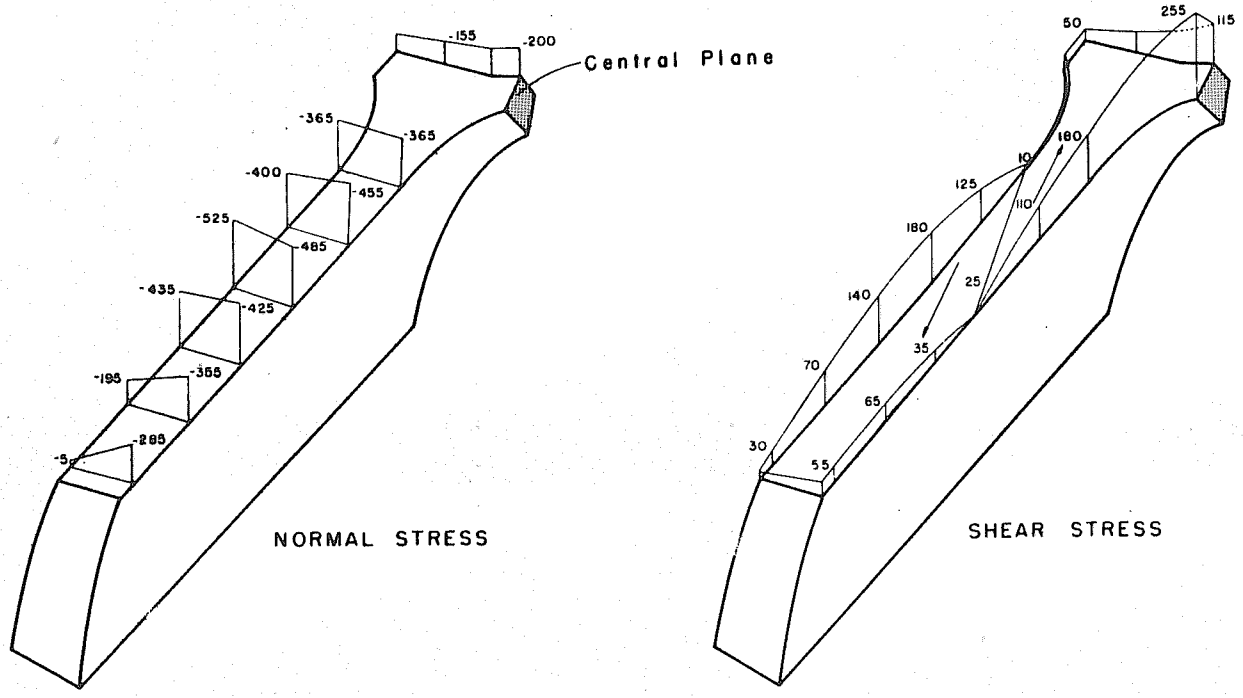


A - GRAVITY LOAD

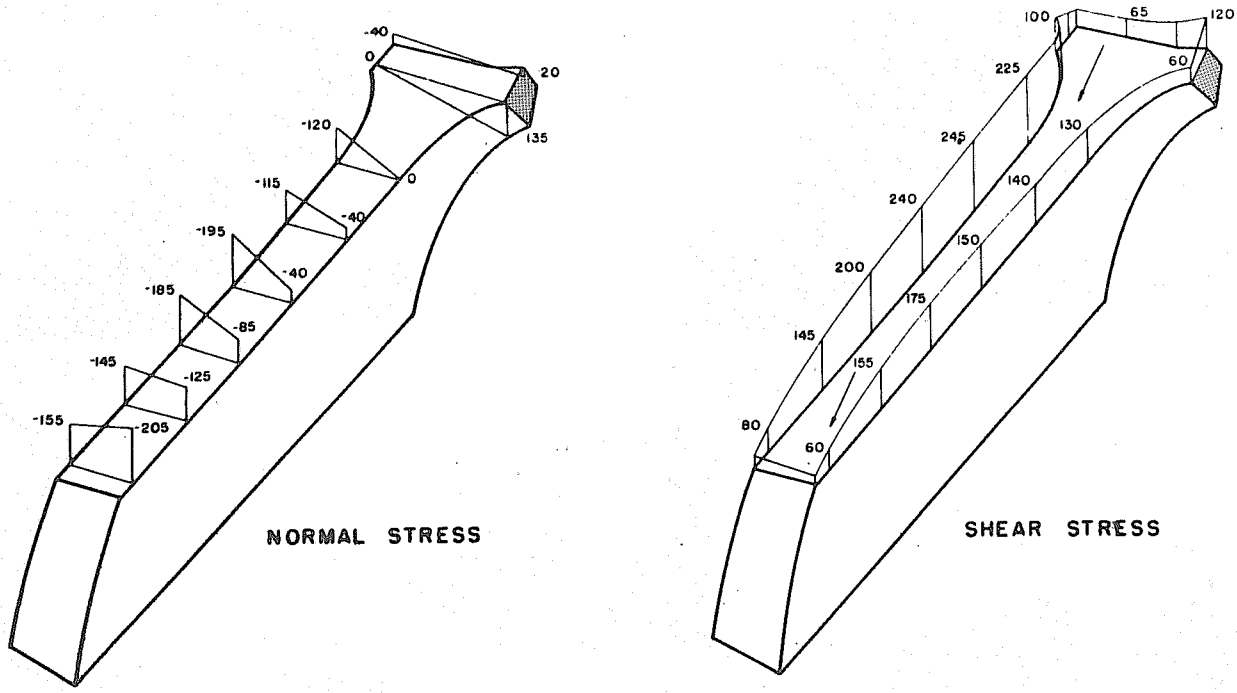


B - HYDROSTATIC LOAD

FIGURE 39 - NORMAL AND SHEAR STRESSES AT ELEVATION 450

properties of the arch and buttress were defined only at the even 50 foot elevations. The area and centroid at each elevation was determined, and integrated graphically to find the position and magnitude of the resultant. The close correspondence of the magnitudes, lines of action, and positions of the resultant applied and resisting forces gives assurance of the validity of the test results. In effect, this balances all the contributions of materials, properties, model loading, instrumentation, and computations against the known forces. At the same time, the unknown effect of foundation and plug-arch interaction is completely out of the picture, and hence it must be concluded that the test technique was of a high order of accuracy.

Table 1 below shows a comparison between the components and resultants of the applied and resisting forces, with the differences computed as percentages of the resultant of all applied forces. For experimental work, the accuracy is gratifyingly high.

TABLE 1

Comparison of Applied and Resisting Forces

| Type of Load | Applied Forces[a] | Resisting Forces[a] | Difference | Percent[b] Difference |
|---|---|---|---|---|
| Vertical Water | .71 | .73 | 0.02 | 0.5 |
| Horizontal Water | 1.18 | 1.31 | 0.13 | 3.4 |
| Gravity | 2.92 | 3.03 | 0.11 | 2.9 |
| Combined Magnitude | 3.82 | 3.98 | 0.16 | 4.2 |
| Direction | 74° | 72° | --- | --- |

a All loads in millions of kips

b Percent of combined applied load

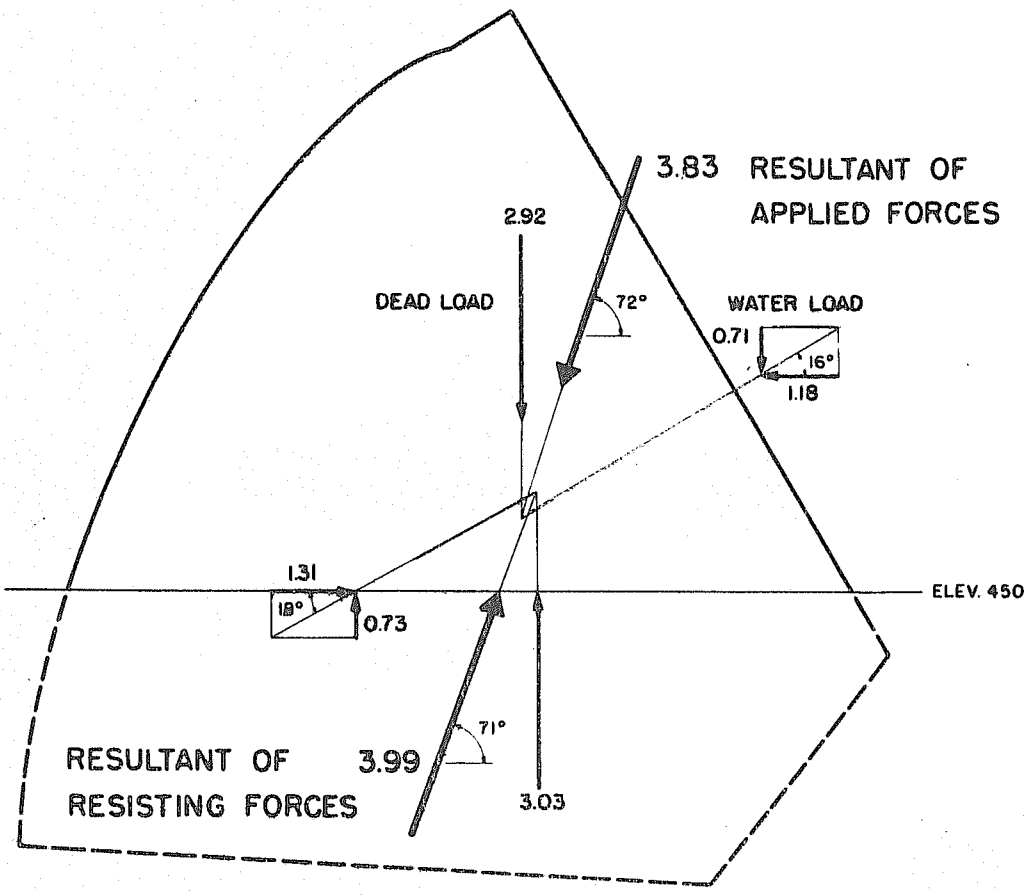


FIGURE 40 - COMPARISON OF RESULTANT OBSERVED RESISTING FORCES WITH RESULTANT COMPUTED LIVE AND DEAD LOADS

## Recommendations

In studying the distribution of the stresses found by the experimental analysis of the conoidal arch, two highly stressed regions become apparent: one at the extrados at the angled intersection of the riding buttress and the flank of the arch, and the other at the base of the dam. At both of these locations, it is believed that the stresses can be reduced to a considerable extent. It must be noted that the high stresses at the intersection of buttress and arch are found only at the angled intersection at the extrados; no such concentration is seen at the intrados. Accordingly, if this design is

developed further, it is recommended that the riding buttress be faired more smoothly, into the arch to avoid the stress concentration evident at this point. It is believed that for the second highly stressed region at the base, improvement can be effected, not by a change in design, but rather by a change in construction procedure. By reference to Figure 33, it can be seen that most of the dead load stress is developed during the first half of the construction of the dam, before the horizontal lifts have reached elevation 600. The compression at the intrados, and the tension at the extrados, are both caused by the inward-leaning flanks of the arch, before sufficient strength has been developed in the crown of the arch to resist this tendency. In order to develop this resistance earlier, construction joints should be laid out to develop as early as possible the strength in the crown of the arch. This can be accomplished by the use of inclined construction joints, so that the dam in effect is constructed of a series of inclined arches, resting one on the other. Thus the second recommendation is to construct the dam with lifts inclined normal to the direction of the upstream face, or $30^{\circ}$ to the horizontal, to reduce dead load stresses at the base.

# APPENDIX

# PROPERTIES OF PLASTER-CELITE MIXTURES

# APPENDIX

# PROPERTIES OF PLASTER-CELITE MIXTURES

## Introduction

Plaster-celite mixtures were studied intensively for use in the Oroville Dam Model Investigation, because the material appeared to satisfy most of the requirements for a model material:

a) It is isotropic and uniformly elastic within the range of stresses developed in the model.

b) Poisson's ratio is equal in magnitude to that of the concrete and rock of the prototype.

c) Its elastic properties do not change with time.

d) Strength and elastic properties can be controlled to fit the requirements of the test.

The process of the setting of plaster seems deceptively simple. Gypsum, the naturally occurring mineral of calcium sulphate, contains two molecules of water. When gypsum is calcined, some of this water of crystallization is driven off. When the calcined gypsum is recombined with water, it is reconstituted into its original rock-like form.

However, as the nature and ramifications of these processes are studied, a number of factors are found that affect the processes and their resulting products. The amount of water initially combined with the plaster affects the consistency of the wet mixture, and the strength and elastic modulus of the hardened mixture. In a secondary effect, strength and elasticity increase as the uncombined water is evaporated from the pores of the hardened mixture. Strength and elasticity are so inter-related, that maximum strain is constant for the complete range of strengths of plaster.

The setting process can be delayed by dilution with water, as well as by the addition of small quantities of electrolytes in the water. The manner in which the calcination is accomplished can have an influence on many of the properties of the plaster.

The significance of many of the variables affecting the physical properties of plaster are made clearer by tracing the steps involved in the complete transition from the raw material gypsum to the reconstituted hardened plaster. Even though these processes have been studied intensively from the time of Lavoisier,[18] there still exists controversy over the meaning of some of the well known phenomena attending the setting of plaster. In the sections that follow, the observations made during the Oroville Dam Model Investigation are explained against the background of current knowledge of the setting of plaster.

The Setting of Plaster

The complete story of the setting of plaster involves consideration of three different phases: the mineral gypsum, the calcined product known as plaster of paris, and the hydrated plaster which has been recrystallized to its original rocklike form. In nature, gypsum is found in its purest form as the mineral selenite, which is typically formed as large transparent platy crystals showing pronounced cleavage planes. Microscopical and X-ray diffraction methods have been utilized to describe the crystals as monoclinic prismatic in form, with 4 or 8 molecules in the unit cell.[19] The crystal lattice is considered as being made up of layers of calcium atoms and sulphate groups separated by sheets of water molecules. The chemical formula is $CaSO_4 \cdot 2H_2O$, commonly referred to as the dihydrate.

When gypsum is heated in the range 97°-190°C for some time, 3/4 of the water of crystallization is driven off, yielding the hemihydrate,

$CaSO_4 \cdot 1/2H_2O$. Two stable forms of the hemihydrate are found, referred to as $\alpha$-hemihydrate and $\beta$-hemihydrate. Both are identical in crystalline form, according to the X-ray powder-diffraction pattern, but have different molecular weights and heats of solution. The $\alpha$-hemihydrate is the more stable, and generally has more favorable properties than the $\beta$-hemihydrate. Pure $\alpha$-hemihydrate can be prepared by heating gypsum in a autoclave in the presence of steam followed by more heating above 100°C with forced circulation to remove uncombined water. On the other hand, $\beta$-hemihydrate can be prepared from powdered gypsum by dehydration in vacuum above 100°C followed by annealing.

At present because of the identity of the X-ray pattern and chemical formulae, the relative amounts of $\alpha$-and $\beta$-hemihydrate in a given sample of calcined gypsum can most easily be determined by a heat of solution test, and even this method is open to considerable error if many impurities are present in the gypsum. Representative physical properties of the two phases of the hemihydrate are shown in Table 2.

The differences found in the many types of commercial plasters available may in large part be explained by the relative amounts of $\alpha$- and $\beta$-hemihydrate evolved by the particular dehydration process used in its manufacture, since the amount of water present in the calcining kettles, in the form of steam, varies with the manufacturer. Thus, for research work involving plaster, the relative proportions of $\alpha$ - and $\beta$ -hemihydrate in the calcined plaster should be defined.

When the plaster and water are first combined in the dilution used for casting, the mixture has a fluidity not much different from that of water. As can be seen from Table 2, the solubility of the hemihydrate, while slight,

TABLE 2

Physical Properties of $CaSO_4 \cdot 1/2H_2O$)

| | Stable $\alpha$-$CaSO_4 \cdot 1/2H_2O$ | Metastable $\beta$-$CaSO_4 \cdot 1/2H_2O$ |
|---|---|---|
| Normal Consistency (cc $H_2O$/100 gm) | 35 | 90 |
| Expansion | .0028 | .0016 |
| Specific Gravity | 2.757 | 2.637 |
| Specific Volume | 52.65 | 55.05 |
| Heat of Hydration, cal/mol | 4100 | 4600 |
| Specific Heat | .230 | .266 |
| Av Tensile Strength, psi[a] | 1000 | 200 |
| Av Compressive Strength, psi[a] | 8000 | 800 |
| Solubility, 20°C, percent | 0.63 | 0.74 |

Note a: Mixed at normal consistency and dried.

is three times that of the dihydrate, which is only 0.20. Thus, as soon as some of the hemihydrate dissolves, the solution is supersaturated with respect to the dehydrate, which precipitates immediately. All the hemihydrate is progressively dissolved and recrystallized out of solution in a very short time. Since all the calcined materials goes through solution before it recrystallizes, its rate of solution and crystallization must be quite high.

When the dihydrate first crystallizes, the individual grains are widely separated in the slurry. As more crystals are precipitated from solution, a tenuous structure begins to form in the slurry and it thickens gradually.

This thickening is so noticeable that some workers have suspected the first product of the hydration of calcined gypsum to be a colloidal gel. As recrystallization proceeds, the mass of crystals becomes so intertwined that it actually can develop resistance against deformation long before hydration is completed. Although there is no definite change of state, the plaster is considered set at this point, because it has definite solidity, and behaves more like a solid than a fluid. Nonetheless, solution and recrystallization is still going on, as evidenced by the copious evolution of heat and hardening of the mass after it has attained solidity.

Since the two processes of solution and crystallization are involved, it can be seen that the fundamental methods by which set can be affected are by methods affecting the rate of solution, and the rate of nucleation. Time of set can be retarded by slowing down solution, and can be accelerated by providing nuclei on which the crystals can grow. And since the amount of water present controls the dilution of the crystals in the slurry, this too is one of the fundamental variables controlling the properties of the plaster.

With the above brief explanation for background, the individual properties of the plaster mixtures discussed in the following sections will be found to be all part of one consistent story of the dynamic processes involved in the setting of plaster mixtures.

Plaster

The plaster used in the model was chosen after making preliminary comparative studies of three types of plaster available in the local market. Although these plasters will not be designated by brand name, they might be described generally as follows:

Type A, an industrial white molding plaster
Type B, an industrial casting plaster
Type C, a slow-setting casting plaster

The chemical analyses for the three plasters are shown in Table 3.

TABLE 3

Physical and Chemical Analyses of Gypsum Plasters

| | Type A | Type B | Type C |
|---|---|---|---|
| Oxides, Percent by weight | | | |
| $SiO_2$ | 0.39 | 1.23 | 1.98 |
| $Al_2O_3$ | 0.04 | 0.28 | 0.41 |
| $Fe_2O_3$ | 0.11 | 0.21 | 0.28 |
| CaO | 38.21 | 37.64 | 40.04 |
| $SO_3$ | 54.37 | 53.61 | 50.11 |
| Loss of ignition at 1850°F | 6.88 | 7.03 | 6.86 |
| Other Volatiles in Loss on Ignition | | | |
| Carbon | 0.25 | 0.14 | 0.49 |
| $CO_2$ (from carbonates) | 0.64 | 0.24 | 0.09 |
| Moisture (200°F) | 0.70 | 1.01 | 0.32 |
| Loss at 440°F on material dried at 200°F | | | |
| Hemihydrate water | 6.27 | 6.96 | ---- |
| Specific Gravity | 2.80 | 2.81 | 2.88 |
| Specific Surface, sq cm/g | 3460 | 3220 | 2940 |
| Surface Mean Diameter, microns | 6.2 | 6.6 | 7.1 |

Only minor differences can be found in the analyses of the plasters. For all practical purposes, these oxide analyses are alike, and representative of gypsum plasters. The calcium sulphate hemihydrate content of the three types is 97% for Type A, 97% for Type B, and 91% for Type C. The extra carbon in Type C is probably due to the admixture used for a retarder. Thus choice of the plaster to be investigated thoroughly for the construction of the model was made by evaluating the plasters according to a number of arbitrary criteria, as shown in Table 4.

TABLE 4

Ratings of Plasters

| Type of Plaster | A | B | C |
|---|---|---|---|
| Bleeding | 1 | 2 | 3 |
| E vs Mixing Time | 1 | 2 | 3 |
| Air Bubbles | 1 | 2 | 3 |
| Time of set, minutes | 22 | 28 | 25 |
| Percent Retarder, $NaH_2PO_4$ | 0.20 | 0.15 | 0 |
| Dry Density, pcf | 43.2-44.8 | 42.8-44.7 | 42.9-44.7 |
| Creep | 5.0-4.0 | 5.4-4.1 | 5.1-4.0 |
| Maximum E x $10^{-3}$, psi | 200-240 | 210-220 | 210-230 |

For the evaluation tests, retarder was added to Plasters A and B, (Type C already contained a retarder which had been added during manufacture), so that set time for all plasters was roughly equal. A constant water-plaster ratio was used for all plasters, but mixtures of two consistencies, represented by flow diameters of 4 and 5 inches, were made by adding the requisite amount of celite. All the variables judged are defined more fully later in the report but can be summarized here. Bleeding was determined as the amount of free water that rose to the top of the cylinder before set. The relationship of the elastic modulus E to mixing time refers to the variability of this property as the mixing time is extended. For some plasters, there was a definite variation; for others, extending the mixing time had very little effect on the resultant elastic modulus. The latter was the more desirable property. The quantity of air bubbles was judged visually in sections of the set plaster.

Although decision to use Type A plaster in the model was made as a result of the ratings shown in Table 4, more extensive experience with plaster indicates that many of the properties that were ascribed to the individual plasters, were in reality a property of technique, and thus in the light of present experience, an entirely different choice might have been made. Some of the factors considered important when the rating was made might now be completely ruled out. Thus, bleeding and the quantity of bubbles might be completely changed by changes in the mixing time. Likewise time of set can be varied at will by the appropriate use of retarders.

However, the effect of time of mixing on the modulus of elasticity seems to be fairly independent of technique, and thus the choice of Type A, for which E was fairly constant over a long time of mixing might still be considered the best plaster for models. At any rate, this was the plaster adopted for the more complete tests that are described in the sections that follow.

Since so many of the properties of plaster seem to depend on the relative amounts of $\alpha$- and $\beta$- hemihydrate present, the relative amount of each phase was determined by finding the heat of solution of the plaster in hydrochloric acid. This was found to be 9.20 calories per gram, which when corrected for the impurities present is equivalent to 10.14 cal per gram, or 1470 cal per mole. Since the heat of solution of $\alpha$-hemihydrate in HCl is 1615 cal per mole, and for $\beta$-hemihydrate is 1110 cal per mole, the amount of $\beta$-hemihydrate in the sample was determined as $\frac{1615 - 1470}{505} =$ 29 percent, and the quantity of $\alpha$-hemihydrate was 71 percent.

A differential thermal analysis was performed on the plaster, giving the thermogram shown in Figure 41. This thermogram shows endothermic reactions of pronounced magnitude at 265°C and 1250°C, and one of slight

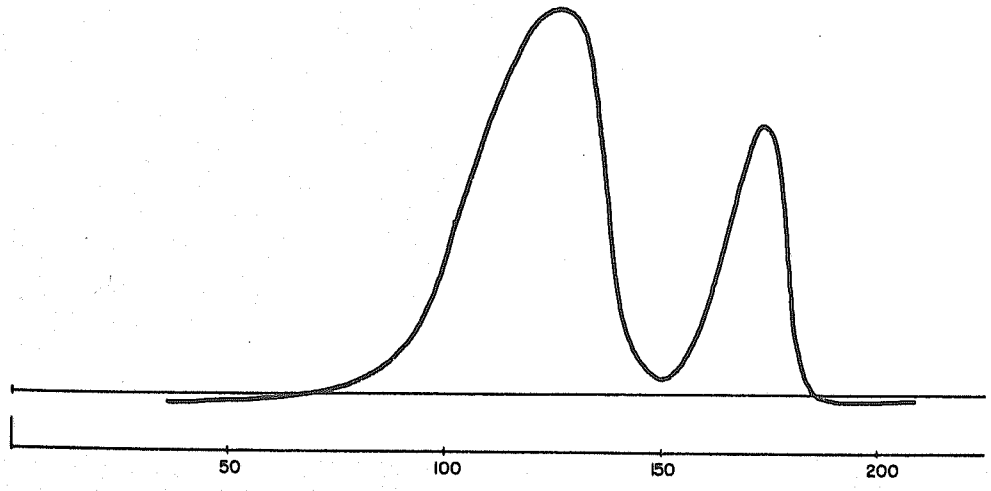


A - LOW TEMPERATURE THERMOGRAM

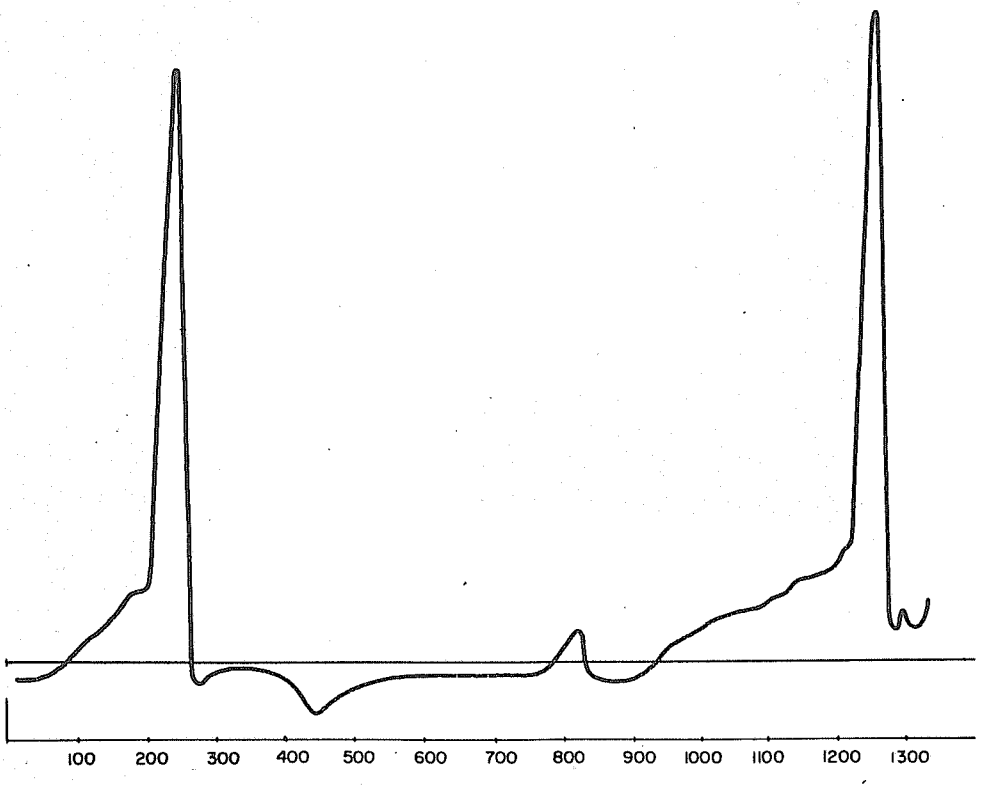


B - HIGH TEMPERATURE THERMOGRAM

FIGURE 41 - THERMOGRAMS OF PLASTER

magnitude at 805°C. One exothermic reaction, of slight magnitude, was indicated at 460°C. Peak points in thermograms represent completion of reactions, and temperatures given are always somewhat higher than the actual temperatures of the substance tested because of the thermal lag caused by the heat required to raise the temperature of the specimen. The endothermic reaction starting at about 220° and peaking at 265°C is characteristic of the loss of the 1/2 molecule of water from the hemihydrate. It will be recalled that in the manufacture of plaster, the calcination temperature is kept below 190°C to avoid dissociation of the hemihydrate. A large endothermic reaction between 1200 and 1250°C is characteristic of the inversion of calcium sulphate from the monoclinic to the rhombohedral form. The endothermic reaction at 805°C is attributed to the dissociation of calcium carbonate, confirming the presence of about 1.5 percent calcium carbonate indicated by the chemical analysis.

The exothermic reaction at 460°C is attributed to the burning of an organic mixture of a carbonaceous nature. It will be recalled that the chemical analysis indicated 0.25 percent carbon, which could represent about 0.5 percent admixture such as sodium keratin by weight of plaster.

These reactions, at temperatures well beyond any encountered in the usual history of the plaster, indicate the relative purity of the plaster used, and indicate also one variable that plagues the experimenter: the tendency for a manufacturer to include a retarder in the plaster, especially a plaster made for sale during the summer months.

Celite

Celite is a trade name for a particular form of calcined diatomaceous earth manufactured by the Johns-Manville Company. However, it has been

mentioned in American technical literature[21] for so long that it has gained popular acceptance as a principal ingredient of model plaster, and it will be so used in this report. Diatomaceous earth, sometimes called infusorial earth, Fuller's earth, and in Europe Kieselguhr, is derived from extensive fossil deposits of diatoms, which are microscopic marine unicellar plants belonging to the Algae family. They are found in a bewildering variety of forms, over 15,000 species of diatoms having been described. Since the siliceous wall of the diatom is practically imperishable, it persists after the death of the individual, so that where diatoms occur abundantly, there is practically an unceasing rain of their minute skeletons onto the bottom of the sea or lake that forms their habitat, leading in time to extensive deposits of diatomaceous earth. The celites investigated for use in the model were all derived from a deposit near Lompoc, California. Being marine deposited, the beds vary in the nature and the amount of impurities. Generally the silica content varies between 70 and 95 percent, the impurities being predominantly clay and clay minerals.

The predominant physical characterisitcs of diatomaceous earth, stemming from the nature of the diatom, are low density (about 2.2), very high specific surface when ground (20,000 to 30,000 sq cm per gram when measured by air permeability methods), ease of grinding, and high sorption.

The predominant physico-chemical characteristic of diatomites is the amorphous structure of the silica. The X-ray diffraction patterns for diatomites show them to be non-crystalline, such patterns that are obtained representing the characteristics of the occluded impurities.

The principal producer of diatomaceous earth products in the United States is the Johns-Manville Company. Of the many grades of diatomaceous

earth available from this company, five were selected for detailed study for possible use in the model plaster. Physical and chemical properties of these five grades are given in Table 5.

TABLE 5

Physical and Chemical Analyses of Diatomaceous Earths

| Oxides, Percent by Weight | Type 1 | Type 2 | Type 3 | Type 4 | Type 5 |
|---|---|---|---|---|---|
| $SiO_2$ | 93.14 | 92.02 | 89.59 | 82.28 | 94.33 |
| $Fe_2O_3$ | 1.72 | 0.10 | 0.08 | 2.66 | 0.21 |
| $Al_2O_3$ | 2.41 | 4.95 | 6.06 | 3.30 | 2.43 |
| CaO | 0.18 | 0.42 | 0.00 | 0.12 | 0.00 |
| MgO | 0.21 | 1.30 | 1.22 | 0.86 | 0.13 |
| Carbon | 0.21 | --- | --- | 0.17 | 0.02 |
| $CO_2$ | 0.00 | 0.09 | 0.02 | 0.10 | 0.01 |
| Total Loss on Ignition @ 1850°F | 1.28 | 0.92 | 0.79 | 7.57 | 0.36 |
| Specific Gravity | 1.93 | 2.14 | 2.26 | 2.03 | 2.21 |
| Specific Surface, sq cm per g | 25,800 | 16,700 | 19,900 | 26,600 | 16,700 |
| Surface mean diameter, microns | 1.2 | 1.7 | 1.3 | 1.1 | 1.6 |

After a number of preliminary trial mixes, the Type 5 diatomaceous earth, referred to hereafter in this report as "celite", was chosen for use in the model, and a number of other tests were run on celite for more complete definition of its properties. It will be noted in Table 5, that the loss on ignition is only 0.36 percent, of which only 0.03 percent is contained as carbon and carbon dioxide. The balance of 0.33 percent is present only as adsorbed moisture, indicating a characteristically low adsorption, and that the material is a calcined product. The silica content between 94 and 95 percent

is indicative of the highest grade of purity. The principal impurities are oxides of aluminum, which would have negligible effect on the performance of this diatomite in any application.

The results of a differential thermal analysis indicate that celite is amorphous, and contains no compounds or impurities producing endo- or exothermic reactions upon thermal treatment to 1100°C. In the presence of a predominant amount of amorphous material such as diatomaceous silica, the X-ray diffraction patterns obtained show only the impurities present. It appears that the major crystalline compound in the celite used is crystobalite, with a small amount of montmorillinite. The crystobalite is not necessarily an impurity, but may represent a considerable portion of the original amorphous silica crystallized by the high-temperature calcination.

Independence of Celite and Plaster

A number of powerful analytical research tools were utilized in an attempt to ascertain whether there was any interaction between the celite and the plaster in the hardened mixture. These included X-ray diffraction methods, differential thermal analyses, gravimetric thermal analyses, and petrographic examination of thin sections. Identical conclusions were reached from all these examination. Neither the microscopical examination of the thin sections or mounts of the plasters in immersion oils nor study of the X-ray diffraction and differential thermal records revealed evidence of chemical reaction of the calcium sulphate phases in the diatomaceous material constituting the celite. The original structure of the diatom skeletons constituting the essential part of the celite was preserved perfectly in the celite-gypsum plaster. Even the very delicate, mesh-like forms were clearly evident at a magnification of about 360 diameters. In addition, the thermal analysis

revealed that there was no one temperature associated with the dissociation of the dihydrate into the hemihydrate, but that this occurred over a considerable range of temperature, from about 125°F. to 140°F.

From this it can be concluded that the roles of the celite and the gypsum plaster are independent in the celite-plaster mixture. The plaster is the strength giving element; the celite provides the high surface area necessary to retain water for the solution and recrystallization of the plaster in the strength desired.

## Test Procedures

Before describing the interrelationships of materials and mix procedures with the wet and dry properties of plaster mixtures, it is necessary to describe a limited number of special test procedures which were used to measure these properties. Some are adaptations of procedures of long standing; others are new and were devised for the current series of tests. The tests chosen for description at this time include those to measure properties common to all tests: consistency, strength, and elasticity.

## Consistency

The consistency of a plaster mixture is a measure of the ease with which it flows into and completely fills a form. It was determined that a fairly fluid mixture was needed to take an accurate impression of the form. Following the general thinking embodied in the flow cone, a consistometer was devised for the accurate measurement of consistency. As shown in Figure 42, this consists of a brass cone having a 1/2 inch diameter opening with a vertex angle of 52° set 3 inches above a horizontal clean glass surface. When level full, this cone holds exactly 50 cc. If overfilled, it can be screeded level by one stroke of a broad spatula.

In use, the consistometer is set on a clean glass surface as shown in Figure 43. The hole is blocked with the operator's finger, and a sample of the plaster mixture is poured level full into the cone. The finger is removed and the wet plaster flows rapidly down onto the plate and outward forming a circular pat. The size of the pat depends only on the viscosity and the density of the mixture, since volume has been held constant. When working with one class of materials, such as a plaster-celite mixture, viscosity is the only variable, and hence the consistometer is an accurate and very convenient method for measuring viscosity.

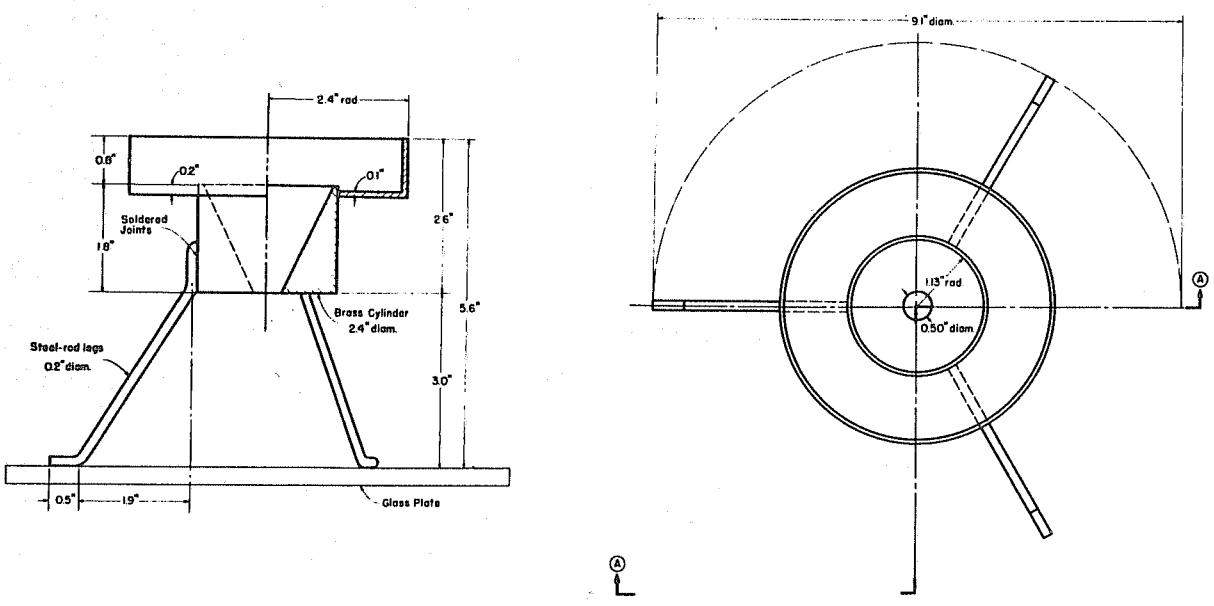


FIGURE 42 - DETAILS OF CONSISTOMETER

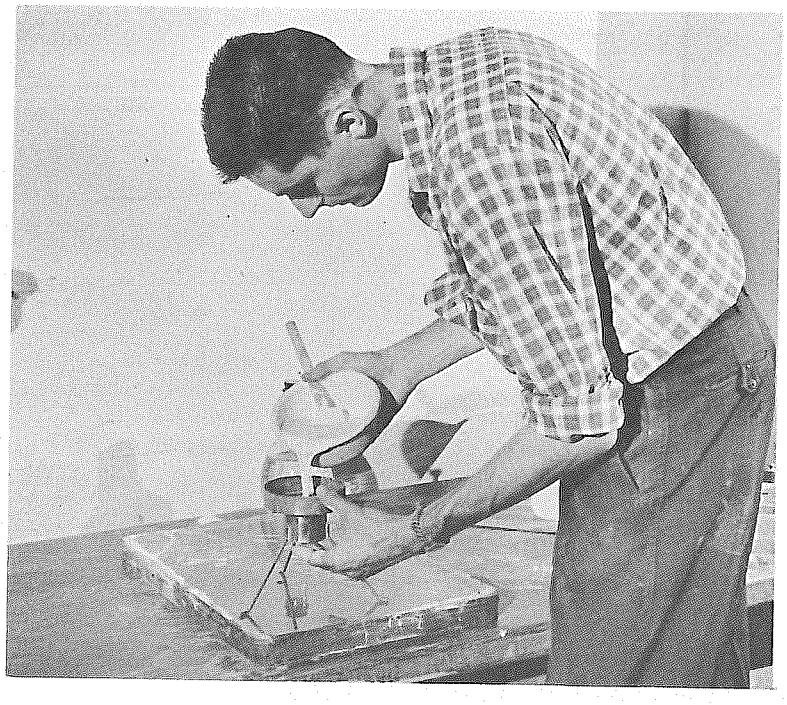

A - POURING PLASTER MIXTURE INTO CONSISTOMETER

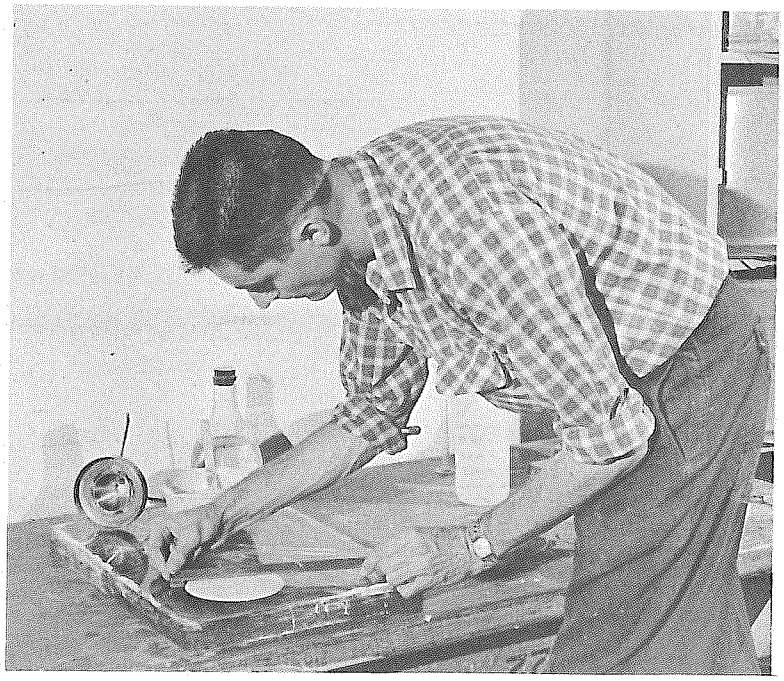

B - MEASURING DIAMETER OF PLASTER PAT

FIGURE 43 - MEASURING CONSISTENCY OF PLASTER WITH CONSISTOMETER

The average diameter of the circular pat is measured, and referred to as the flow diameter. The more fluid the mix, the larger the flow diameter. With a little use, an operator referring to a given flow diameter, evokes in his mind an image of a definite consistency of material much the same as the picture a concrete operator visualizes when he refers to a particular slump.

Modulus of Elasticity and Compressive Strength

The modulus of elasticity and the compressive strength of hardened plaster mixtures were determined on 3 inch diameter by 6 inch high cylinders, cast in cardboard molds. After casting, the cylinders were stored in the molds one day, at 70° F. and 50 percent relative humidity. After 24 hours, the plaster cylinders were stripped and dried for 3 days in an oven with rapid circulation of air at 95°F.

The ends of the cylinders were prepared for testing by grinding flat against a sandpaper disc, using a jig to maintain the surface at right angles to the axis of the cylinder. It was found by experience that any capping of the cylinder using hydrostone or other plaster material gave spurious indications of strength, since some of the water from the capping plaster penetrated the dried plaster of the cylinder, weakening the boundary.

While there was some difference in detail for particular tests, the typical elasticity-strength test was run as follows: the compressometer shown in Figure 44 was fitted onto the cylinder. The cylinder was then loaded at a rate of 600 lbs. per minute to a compressometer reading of 0.0035- inch, corresponding to a strain of just under 600 micro-inches per inch. The load was then removed and the compressometer reset to zero. Three cycles of load were then applied at a loading rate of 600 lbs. per

minute, each time noting the loads at a compressometer reading of 0.0035-inch. At the conclusion of the loading cycles, the compressometer was removed and the cylinder loaded at a rate of 2,000 lbs. per minute to failure. As shown in Figure 45, the stress-strain diagram for hardened plaster was a straight line within the range anticipated for use on the model.

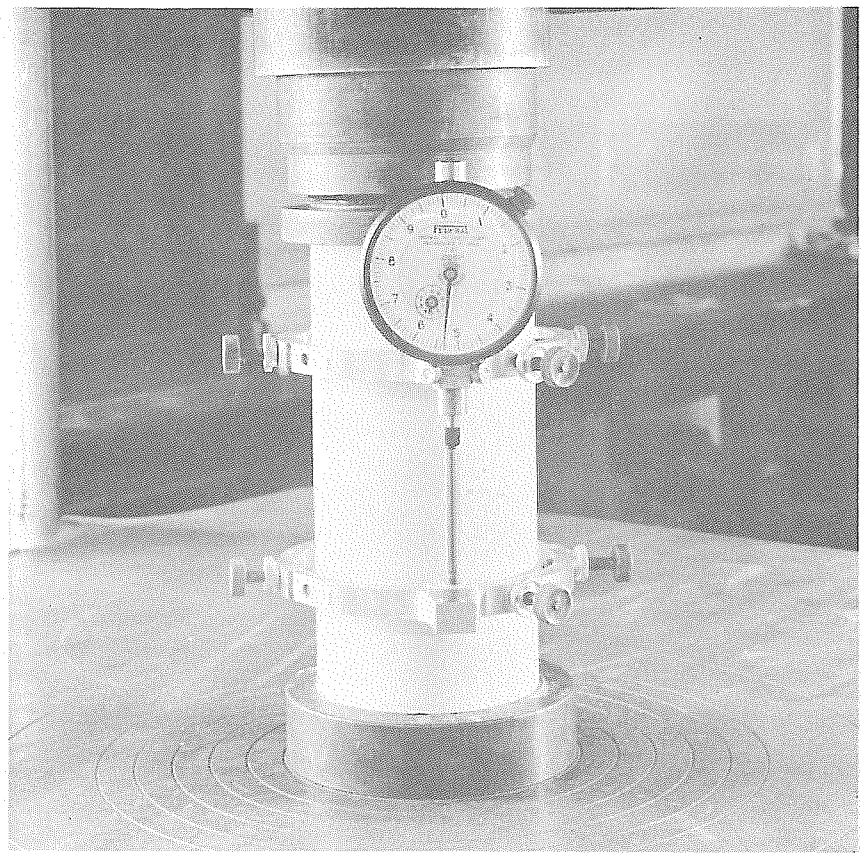

FIGURE 44 - LIGHTWEIGHT ALUMINUM COMPRESSOMETER FOR 3- BY 4-INCH PLASTER CYLINDERS

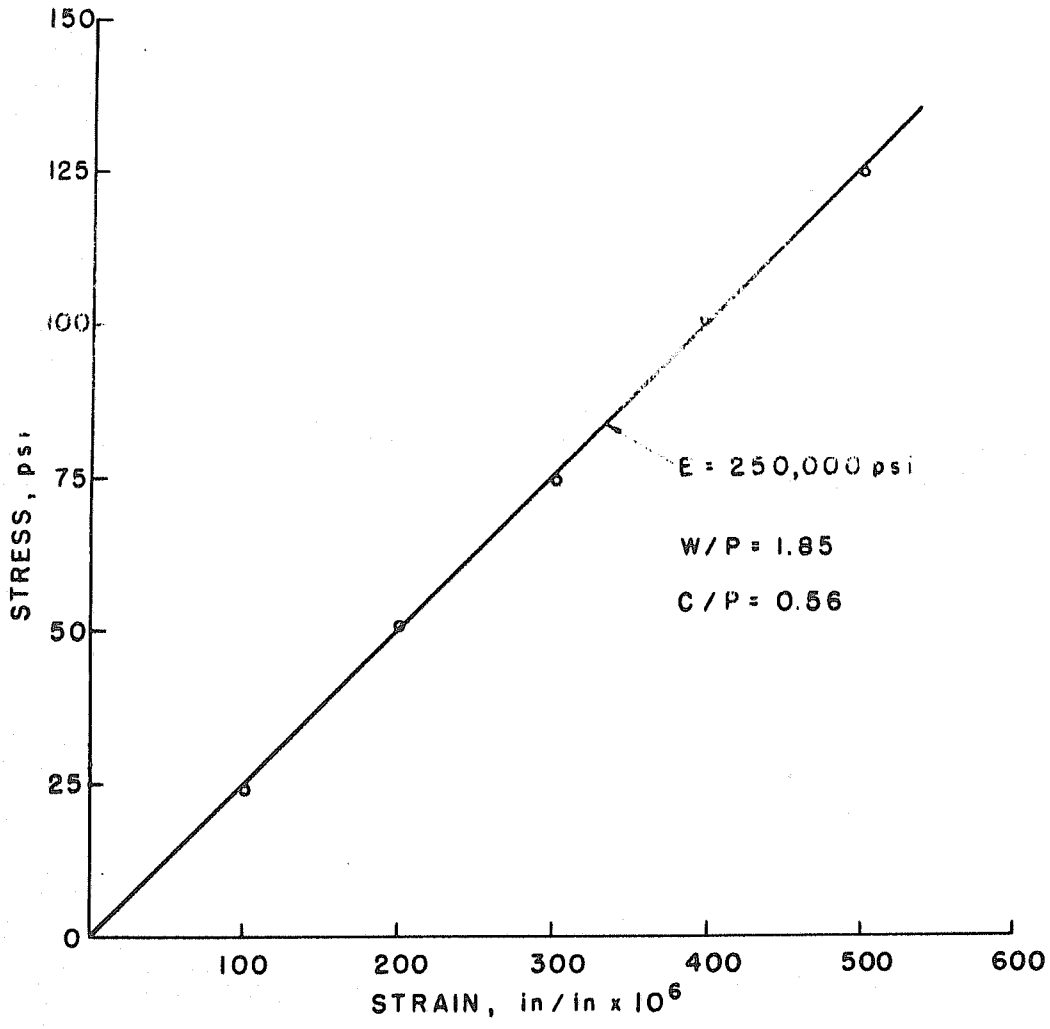


FIGURE 45 - TYPICAL STRESS-STRAIN DIAGRAM FOR PLASTER

Flexural Modulus of Elasticity

Since the model was to be subjected to considerable moment as well as direct load, tests were undertaken to compare the modulus of elasticity determined by direct compression tests on cylinders with that determined by flexural tests of beams. The beams were 3 x 4 x 40 inch in dimension, spanning 36 inches, and loaded at the third points, as shown in Figure 46. The cylinders were the usual 3 inch by 6 inch cylinders cast in cardboard molds.

Two series of tests were run. Three separate determinations of modulus of elasticity were made on each beam. As in the usual beam test, modulus of elasticity was determined by measuring the maximum deflection of the beam. At the same time, measurements were made of the strain of the extreme fibers in tension and compression by means of SR4 strain gages.

At the completion of the bending tests, the central third of the beam was sawed out, the ends squared off, and loaded in direct longitudinal compression. Results of all three tests, shown in Figure 47, agree within 2 percent of the average.

It was found further that the modulus of elasticity in compression as determined from the cylinders agreed with the average of the flexural modulus tests. From these tests, it was concluded that the plaster-celite material was homogeneous and isotropic, and that the simpler compression tests on 3 inch by 6 inch cylinders could be relied on fully to evaluate the modulus of elas-

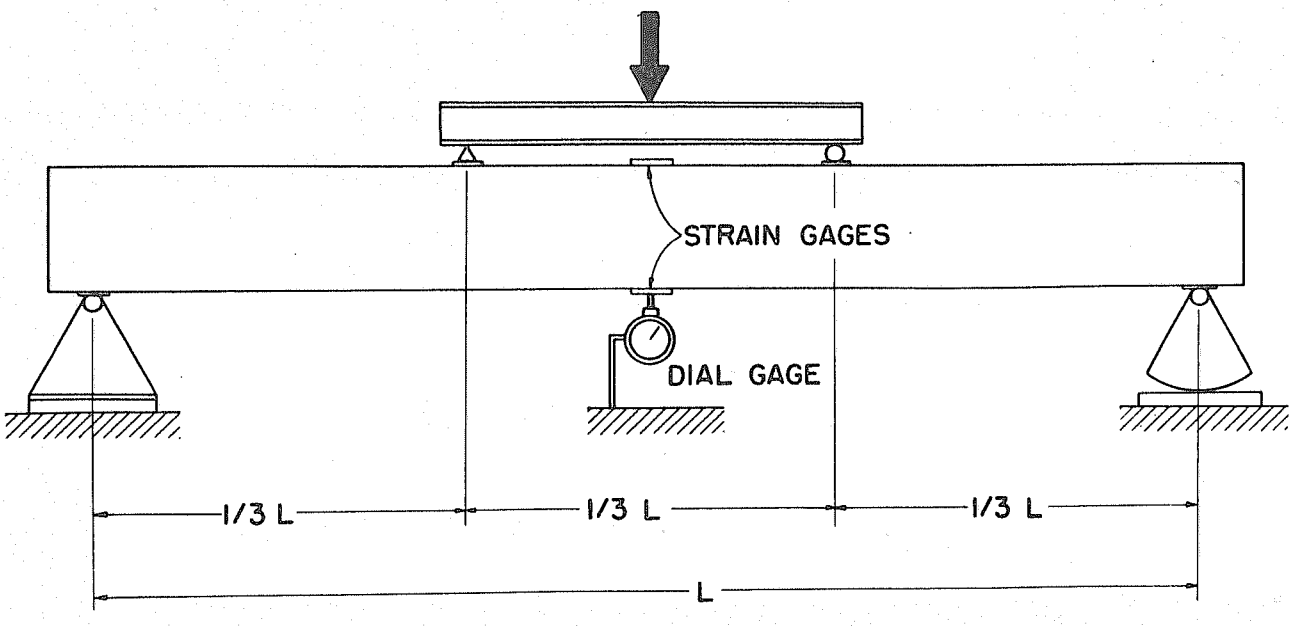


FIGURE 46 - SET UP FOR DETERMINING FLEXURAL MODULUS OF ELASTICITY

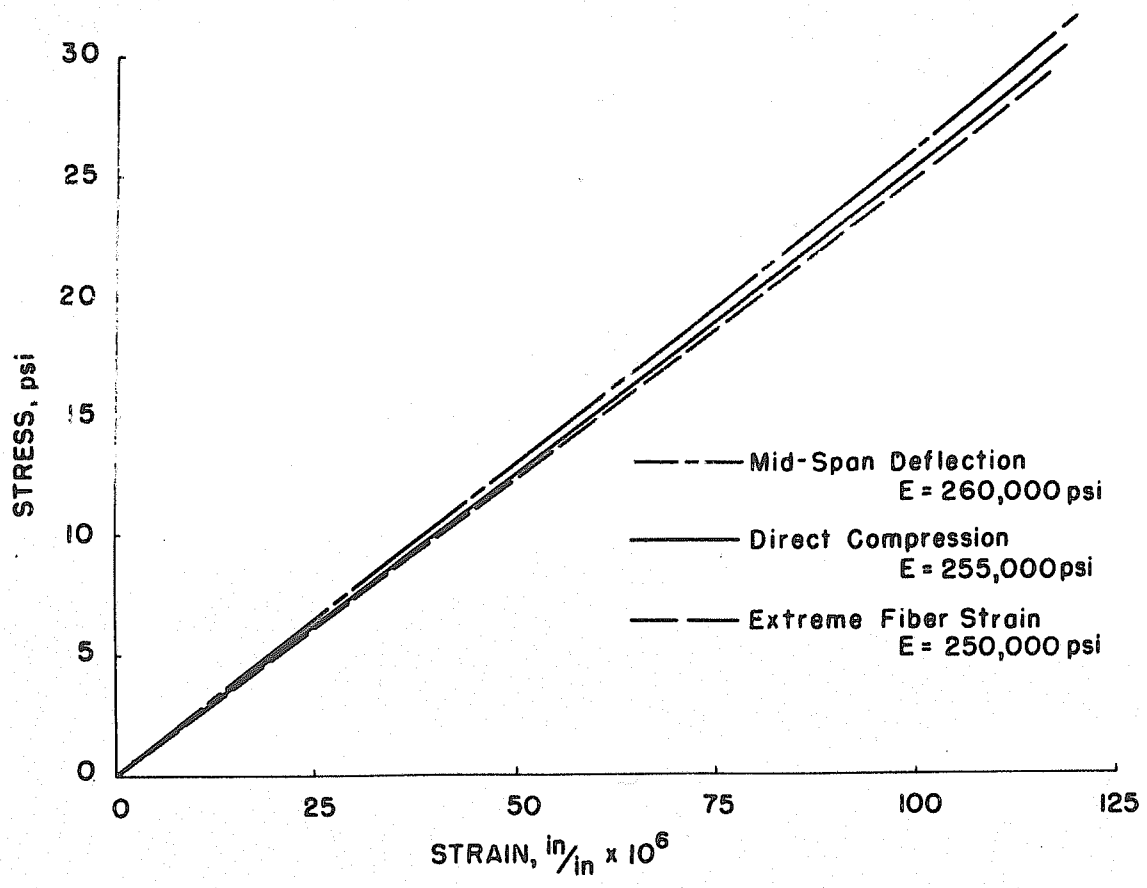


FIGURE 47 - STRESS-STRAIN DIAGRAMS FOR THREE TYPES OF TEST FOR MODULUS OF ELASTICITY

Sonic Modulus of Elasticity

For unusually shaped objects, and for cylinders in which the elastic properties are changing rapidly, sonic tests for modulus of elasticity proved invaluable. The modulus of elasticity of an object is related to its resonant frequency by

$$E = KWn^2$$

where

E = modulus of elasticity, psi
n = resonant frequency, cycles per second
W = weight of object, pounds
K = geometric constant:
For 3 x 12 inch cylinder, K = 0.116
For 4 x 20 x 30 inch slab, K=0.0118

The resonant frequency of an object can be determined by the use of a signal generator and a pickup. The setup for a slab is shown in Figure 48. The slab is shown mounted on rubber shock mountings near the four corners. Position of these was not critical, as large changes in position on the shock mounts did not affect the resonant frequency. The object is excited at different frequencies by the speaker, which is energized by the signal generator. The pickup is attached to a sensitive volt meter which measures the output of a microphone attached to the object. Although the frequency of the signal can be read from a dial on the signal generator, the frequency counter is much easier to read and interpolate, and this was used in all tests. The frequency at which the pickup records maximum response is the resonant frequency.

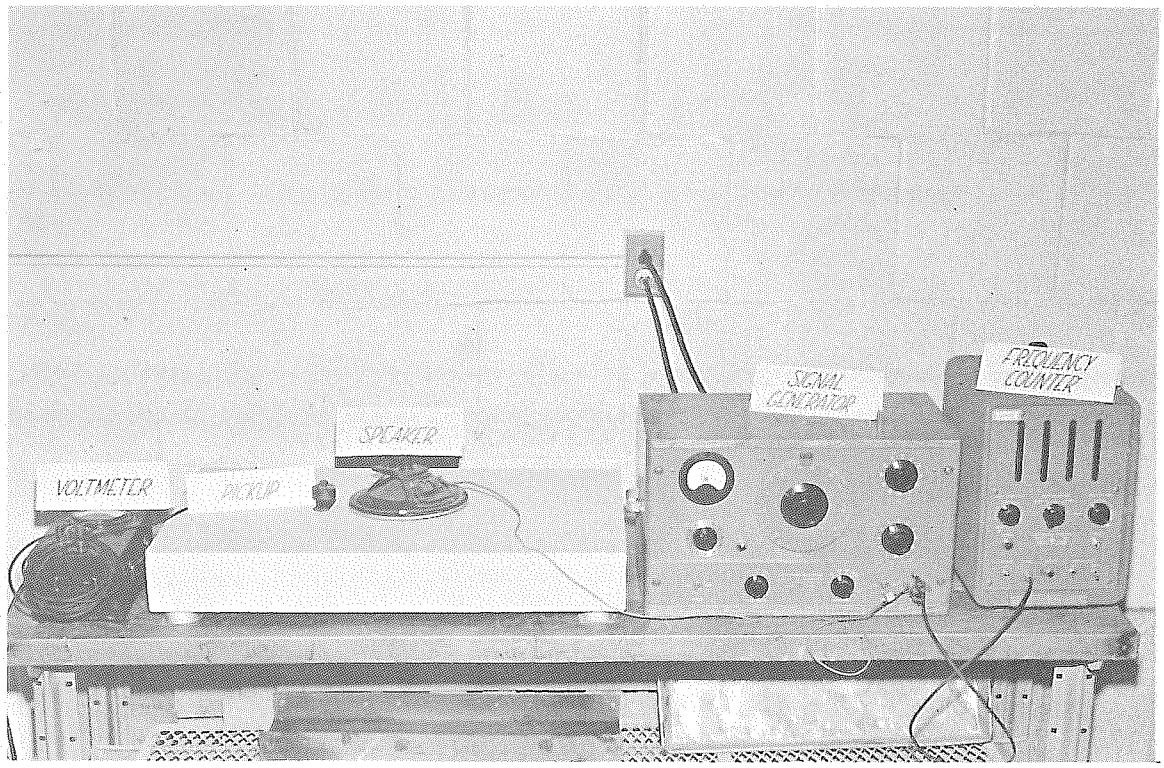


FIGURE 48 - APPARATUS FOR DETERMINING MODULUS OF ELASTICITY OF A PLASTER SLAB

A somewhat similar setup was used for the 3 x 12 inch cylinders, except that the cylinder rested on two wires, the speaker was supported over the cylinder, and the pickup was attached by rubber bands. Six cylinders of different mix proportions were tested for both sonic and compressive modulus. The values obtained in all six tests are given in Table 6.

TABLE 6

| Mix | $E_{static}$ | $E_{sonic}$ |
|---|---|---|
| 57E36' | 1,080,000 | 1,080,000 |
| 57E39' | 494,000 | 491,000 |
| 57E41' | 339,000 | 333,000 |
| 57E44' | 172,000 | 173,000 |
| 57E52' | 143,000 | 149,000 |
| 57E55' | 98,500 | 99,000 |

The above data indicate a very close correspondence of the modulus of elasticity of the plaster-celite mixtures from the two types of tests. It can be concluded that for conditions where the modulus of elasticity is changing rapidly, as in the very early ages of a plaster mixture, the sonic modulus method, which takes but seconds to perform, is an invaluable research tool.

Furthermore, as indicated from the photograph, the sonic modulus method, which is not destructive, was used to check the uniformity of the modulus of elasticity of each slab entering into the construction of the second model dam foundation.

The Water-Plaster Ratio and Its Effect on Modulus of Elasticity

Choice of scale and instrumentation for model tests is dependent primarily on the modulus of elasticity of the model material, which is the measure of its deformability. Hence the modulus of elasticity was the fundamental property to be defined in the material investigation: the other properties were significant, but were secondary in importance. In the section that follows, the factors affecting elasticity are explored, followed by sections describing the interrelated properties affecting structural behavior of the hardened plaster, and the properties affecting the pouring of the plaster in the molds.

The modulus of elasticity of hardened plaster depends primarily on the ratio of the quantities of water and plaster initially combined in the mixture. As shown at the left in Figure 49, the elasticity of plaster

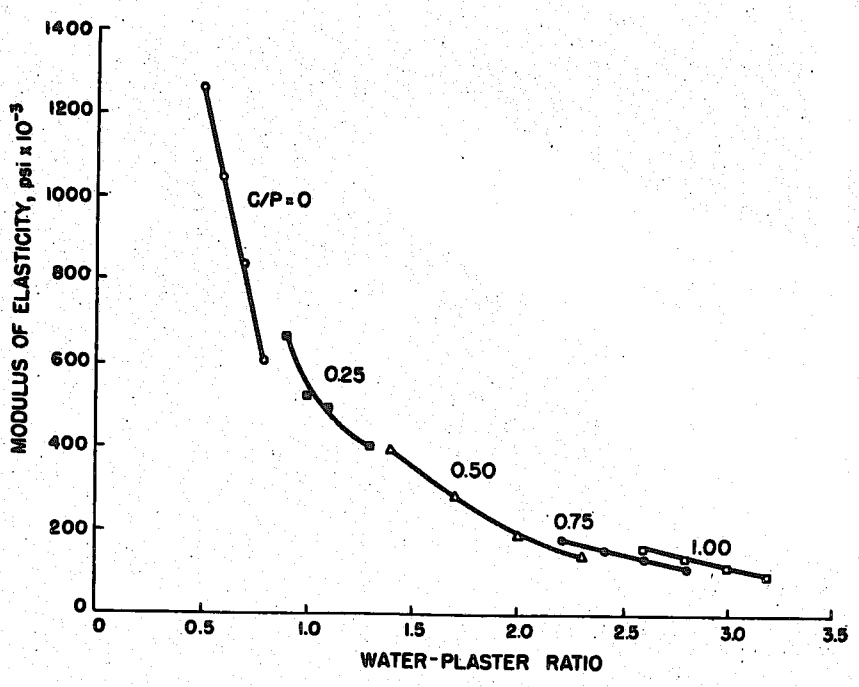


FIGURE 49 - EFFECT OF WATER-PLASTER RATIO ON ELASTICITY OF VARIOUS CELITE-PLASTER MIXTURES

mixtures can be doubled by decreasing the water-plaster ratio (W/P) from 0.8 to 0.5. However, there are definite limits within which this ratio may be varied. For the mixture with W/P of 0.5, the flow diameter was 3 inches and the consistency was so stiff that trouble was anticipated in filling molds. At the lower end of the line, for the mixture with W/P of 0.8 and a flow diameter of 5 inches, so much water was added to the plaster that it segregated readily, and pure water rose rapidly to the top of the mold. Evidently, the desirable consistency would have some intermediate W/P. Bearing in mind that mixtures with moduli of elasticity of 480,000, 240,000 and 120,000 psi were desired for various parts of the model, it can be seen that this mixture would yield plaster with too high an elastic modulus for any part of the model.

Since the elasticity can be decreased easily by addition of water, an agent was needed to maintain the water in contact with the plaster, such as an inert filler having a large specific surface. The material chosen was fine celite, a calcined diatomaceous earth. When celite was added in the amount of 25 percent by weight of the plaster, a new range of elastic moduli from 400,000 to 700,000 was found as W/P varied from 1.3 to 0.9. As in the first case, the flow diameters varied likewise from 3 to 5 inches. For a desirable flow diameter of 4-1/2 inches, the modulus of elasticity was 500,000 psi.

By continuing to add definite amounts of celite to the plaster and combining with water, the complete series of five curves was developed, each representing a complete range of consistencies from soupy to stiff mixes. By connecting up only the points having the desirable consistency represented by a flow diameter of 4.5 inches, Figure 50 is produced which relates the

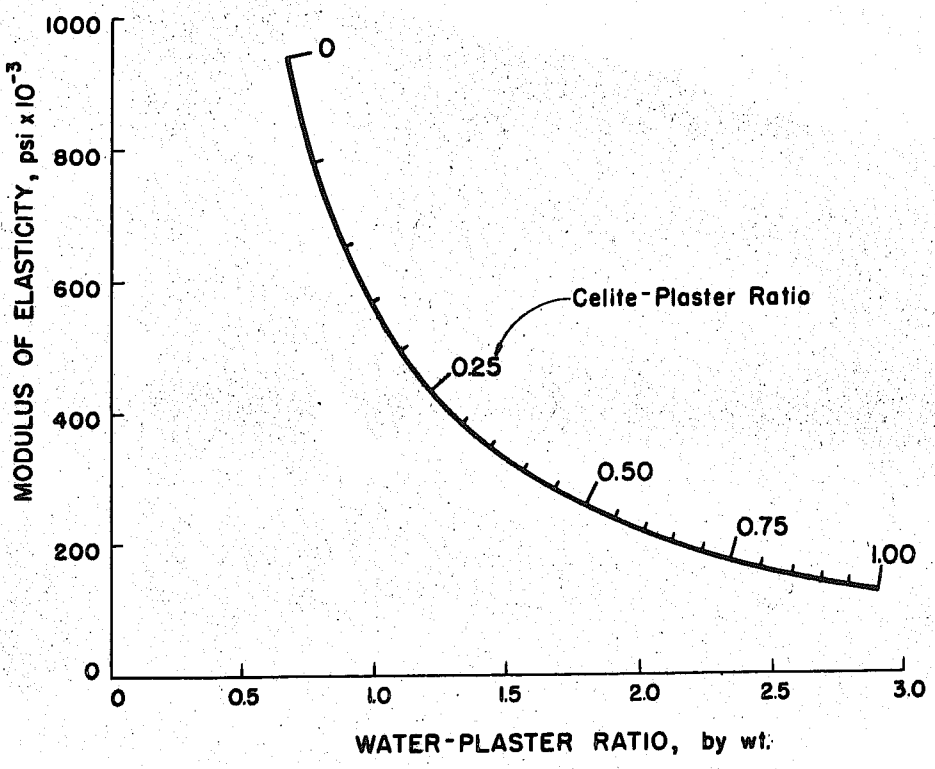


FIGURE 50 - VARIATION OF ELASTICITY WITH WATER-PLASTER AND CELITE-PLASTER RATIOS FOR PLASTER OF CONSTANT CONSISTENCY

modulus of elasticity of the plaster mix to both W/P and the celite-plaster ratio, C/P. Thus, if a material is desired having a modulus of elasticity of say 420,000 psi, a glance at the graph shows that C/P should be 0.24 and W/P should be 1.20. It should be cautioned, however, that the above data are representative of only the one plaster used in the tests. When using other plasters, a corresponding array of tests should be performed in order to derive a W/P-elasticity curve. Similar curves can be drawn for different consistencies, representing stiffer or soupier mixes.

## The Water-Plaster Ratio and Its Effect on Strength

The series of curves shown on Figure 49 relating the modulus of elasticity to the water-plaster ratio for various values of the celite-plaster ratio has its counterpart in Figure 51, where the effect of the same variables on the ultimate compressive strength of the cylinders is examined.

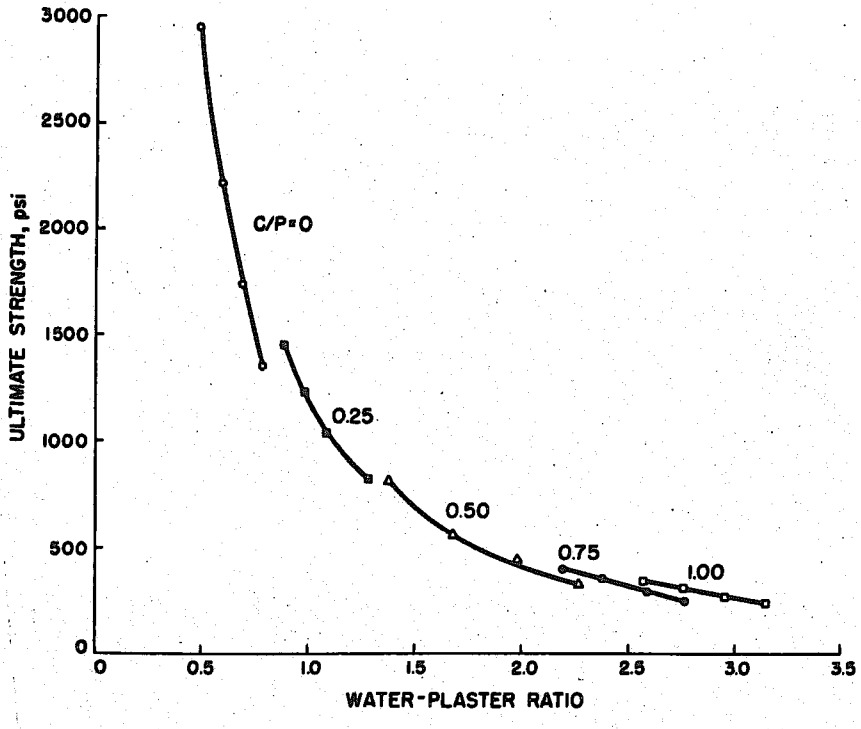


FIGURE 51 - EFFECT OF WATER-PLASTER RATIO ON COMPRESSIVE STRENGTH

The similarity of the two figures is marked. In Figure 52, the compressive strength values from Figure 51 are plotted against the values of modulus of elasticity from Figure 49. It can be seen that strength and modulus of elasticity are linearly proportional: the modulus of elasticity is 450 times the compressive strength of the hardened plaster mixture for the complete range of elastic moduli from 100,000 to 900,000 psi, for the plaster used

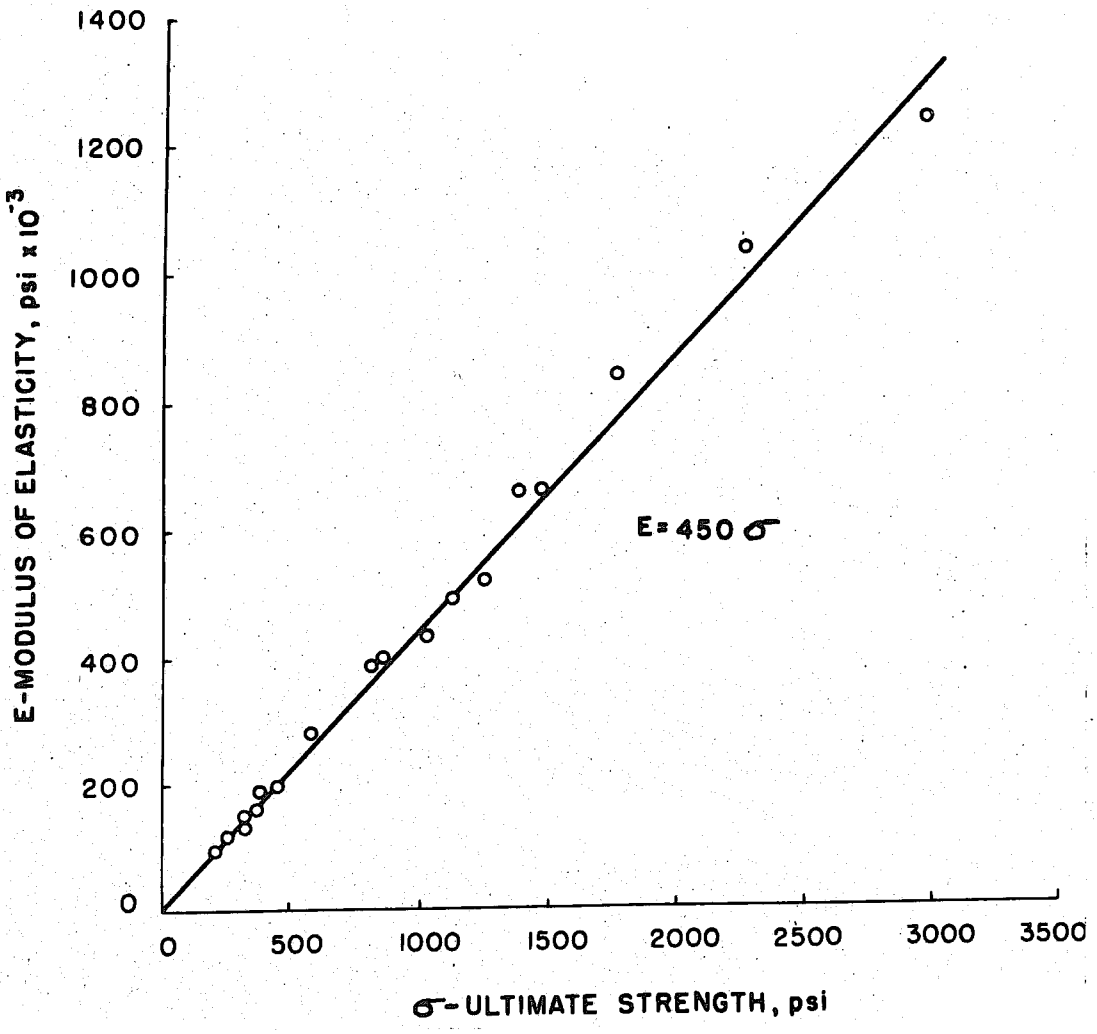


FIGURE 52 - RELATION BETWEEN ELASTIC MODULUS AND STRENGTH OF PLASTER

in these tests. Hence the remarks made about the effects of the water-plaster ratio and the celite-plaster ratio on the modulus of elasticity in the previous sections apply with equal vigor to ultimate strength.

Tensile Strength

A few preliminary tests indicated that the tensile strength of plaster mixtures was a substantially higher proportion of the compressive strength than that of concrete mixtures. Since tensile strength was not a property of primary importance in this particular model, only a few tests were conducted for this property.

Test specimens were standard briquets such as those formerly used for determining the tensile strength of cement mortars, stripped at 24 hours, and dried three days in an oven at 95°F. Results of the tests are shown on Table 7. For the three mixtures shown, the tensile strength averaged 1/5 to 1/6 the compressive strength of the plaster. No doubt this value could be considerably improved with the addition of fibrous fillers, as is often done in commercial practice.

TABLE 7

Relation Between Tensile and Compressive Strength of Plasters

| Test No. | 57E97 | 58E8 | 57E98 |
|---|---|---|---|
| $f_t$ - tensile strength of briquets, psi | 78 | 92 | 205 |
| $E_c$ - modulus of elasticity of cylinders, psi | 166,000 | 230,000 | 551,000 |
| $f_c$ - computed compressive strength, psi | 370 | 510 | 1220 |
| $f_t/f_c$ | 0.21 | 0.18 | 0.17 |

Poisson's Ratio

Three methods were considered for determining the very minute lateral deformations associated with the longitudinal compression of the plaster-celite cylinders. Dial gages were immediately ruled out, as the total lateral deformation is of the order of only 0.0005 inches or only 5 least readings of the best dial gages. An interferometer, which was capable of measuring lateral deformations by counting the interference bands of light waves, was tried but found to be unreliable for this particular material. It is possible that local crushing of the soft plaster-celite at the gage contacts accounts for most of this inaccuracy. The successful method was to attach pairs of SR4 strain gages to measure longitudinal and lateral strains, as shown in Figure 53. Several cylinders of different mix proportions were tested using the SR4 setup. The values of Poisson's ratio ranged from 0.22 to 0.25. An average value of 0.24 was used in the elastic analyses of the model strains.

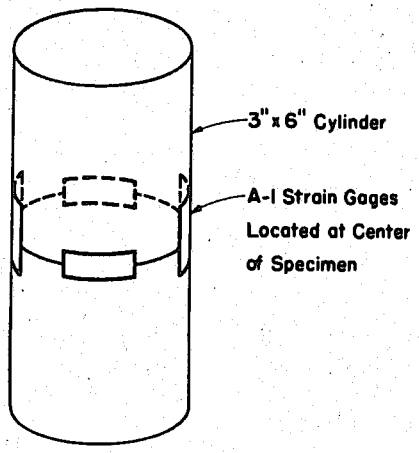


FIGURE 53 - MEASUREMENT OF POISSON'S RATIO USING SR4 GAGES

Maximum Strain

In preceding sections, it was shown that for plasters having a wide range of strength and elastic modulus, a constant proportionality was found between elastic modulus and compressive strength, and another nearly constant proportionality found between ultimate compressive and ultimate tensile strength of plaster. This leads directly to two values of maximum strain that can be used to judge how close any part of a plaster model is to failure, no matter what its strength may be. Since $E = 450\,\sigma'$ where $\sigma'$ is the compressive strength at failure, it follows that

$$\epsilon' = \frac{\sigma'}{E} = \frac{1}{450} = .002220$$

That is, compressive strain at failure will be no less than 2220 microinches per inch. As shown in Figure 54, this is a conservative assumption based on straight-line deformation to failure. Since tensile strength is 1/5 to 1/6 compressive strength, it can likewise be assumed that tensile strain at failure for any celite-plaster mixture will be no less than 2220/6 or

370 microinches per inch. Since in model testing, strains are customarily measured at the most highly stressed portions of the model structure, it is simple to judge how close the model is to failure by keeping in mind the two maximum strains as the model is being loaded, and maintaining the load within a safe limit that does not exceed the maximum strain.

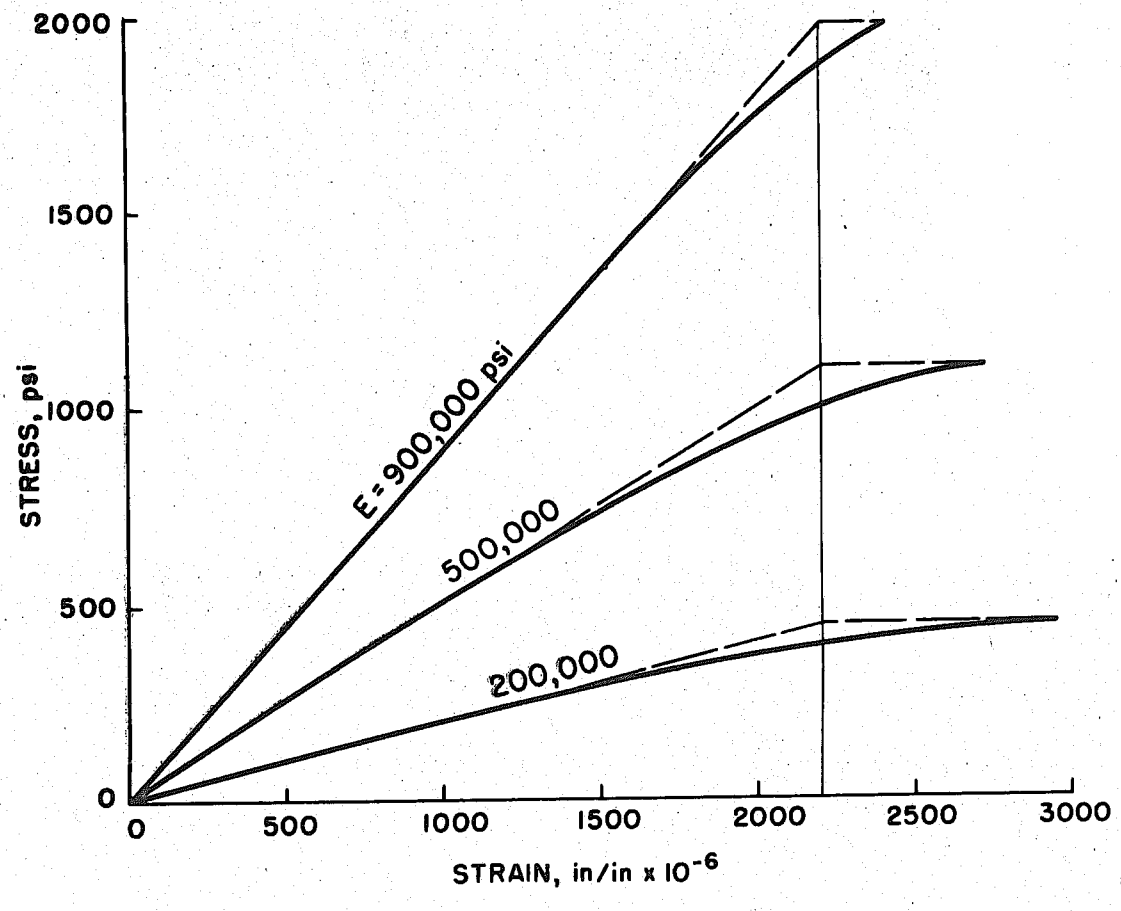


FIGURE 54 - COMPLETE STRESS-STRAIN DIAGRAMS SHOWING CONSTANT LIMITING STRAIN FOR A VARIETY OF PLASTERS

## The Effect of Drying on Strength and Elasticity

In a preceding section, the importance of the initial water-plaster ratio to the compressive strength and elasticity of hardened plaster was shown.

It must be emphasized that all the preceding remarks apply to test specimens mixed with the proportions shown, and dried three days at 95°F.

Drying is an important step in stabilizing the strength of plaster. Subsequent to the setting of a given plaster mixture, the strength and elasticity can be increased depending on the amount of water that is removed. The amount of water necessary to make a fluid mixture of plaster is many times that needed for combination with the hemihydrate to produce the dihydrate. Consequently, immediately after set there is present a large proportion of free or uncombined water. As shown in Figure 55, removal of this water

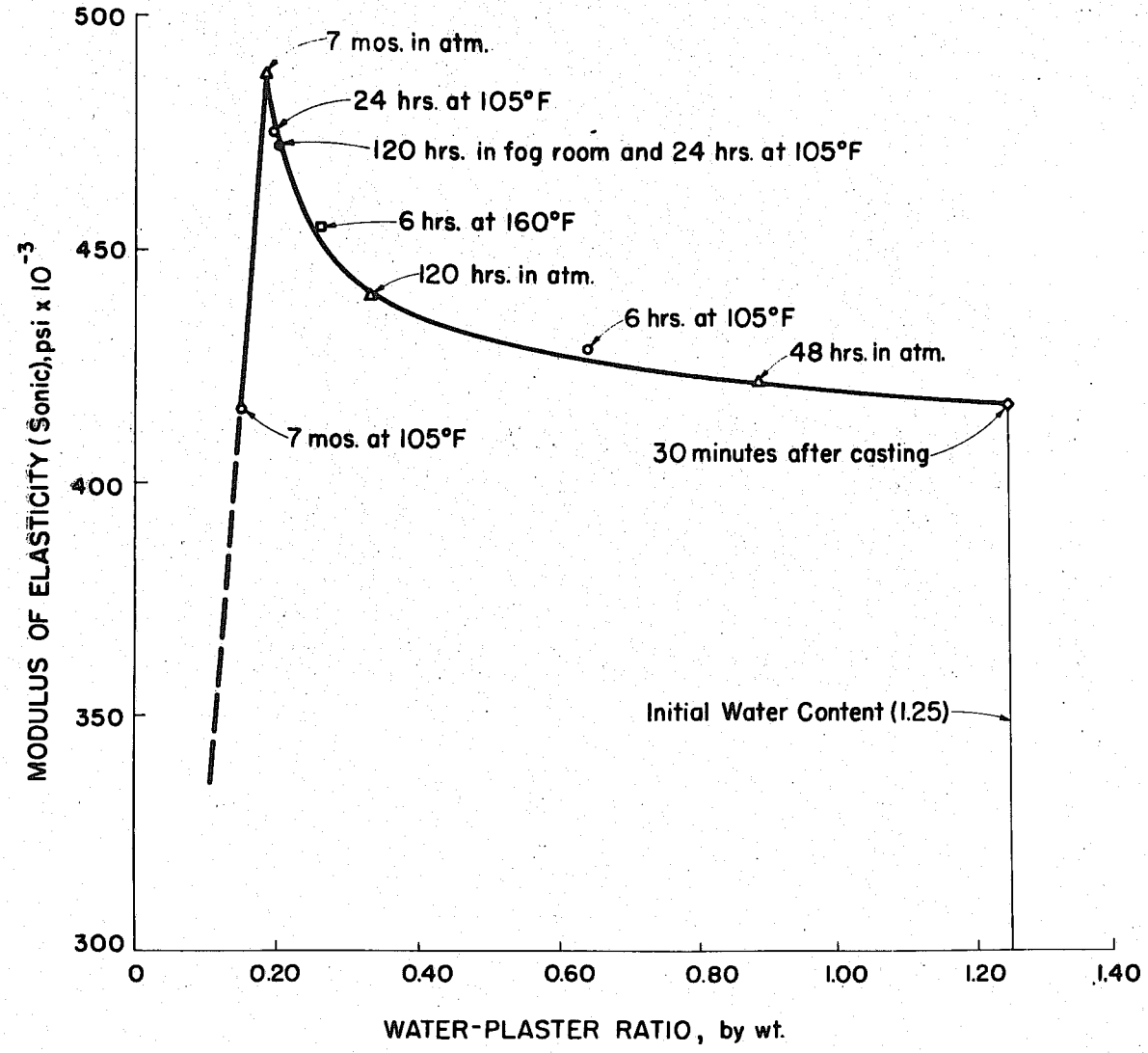


FIGURE 55 - EFFECT OF DRYING ON ELASTICITY

tremendcusly increases the strength of the hardened plaster. At the extreme right-hand end of the curve on Figure 55, a symbol is plotted to represent the elastic modulus of four plaster cylinders tested within 30 minutes of set. At various points on the curve, the strength of similar cylinders is plotted against water content for several different drying procedures. Some cylinders were dried in the laboratory atmosphere, some at 105°F., and some at 160°F.

Despite the variety of drying conditions, all points fall on a common curve, up to a water content of 0.186. At water contents below this point, the curve falls off rapidly. If it is recalled that the water content of 0.186 represents exactly the weight of the combined water in the dihydrate $CaSO_4 \cdot 2H_2O$, it can be seen that water contents less than this represent an actual change in state of the molecule. Many researchers have stated that dissociation can commence anytime that hardened plaster is stored above a definite temperature, often given as 130°F., but the curve of Figure 55 shows that such fears are groundless as long as the water content remains above 0.186. At the same time, it can be seen that if stored long enough at temperatures below this so-called point, sufficient water can be removed in time to affect the nature of the molecule.

The effect of ambient temperature on the drying of plaster is shown in Figure 56, which is an elaboration of Figure 55. Here it can be seen that below 95°F. the water content for the particular specimen being studied reached minimal value at ten days, and thence remained constant. For storage at 105°F., the minimum water content was reached in one day, and subsequent storage at the same temperature reduced the water content

slightly. When stored at the elevated temperature of 160°F., however, minimum water content was reached in about 7 hours, and considerable dissociation had been achieved by two days. It can be concluded that 95°F. is a safe limit for heating plaster for removal of excess water.

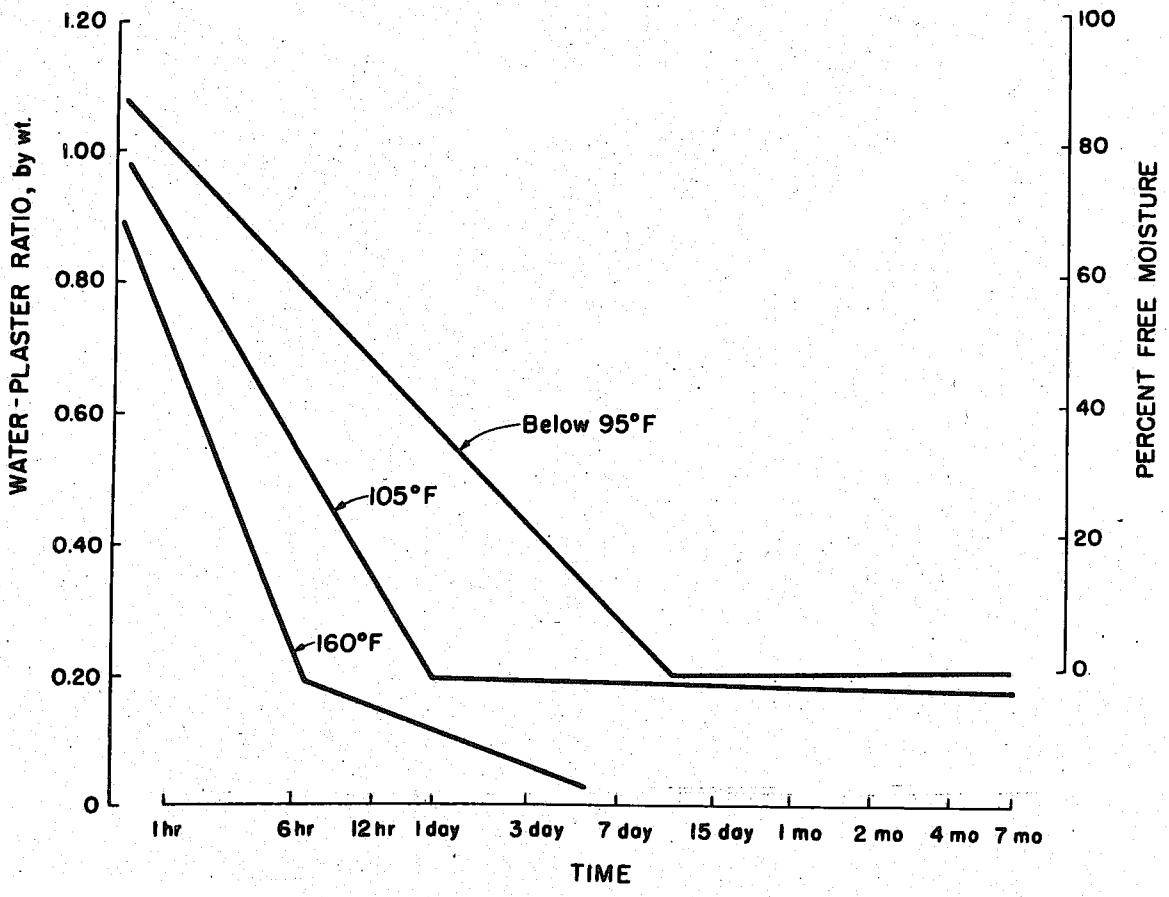


FIGURE 56 - DRYING RATES AT VARIOUS STORAGE TEMPERATURES

Since hardened plaster gives up water to the atmosphere readily, it can be seen that when no attempt is made to stabilize the water content of a model, the actual strength and elasticity for various parts of the solid substance will be unknown depending on how much water has been removed by evaporation. Although the curve of elasticity varies rather rapidly near

the point of zero free moisture content, it is easier to achieve and maintain this water content than any water content where the water tends to migrate from the solid. Hence, curing of the Oroville Dam model as well as all specimens was made in drying ovens at 95°F. for a period sufficient to achieve zero free moisture content.

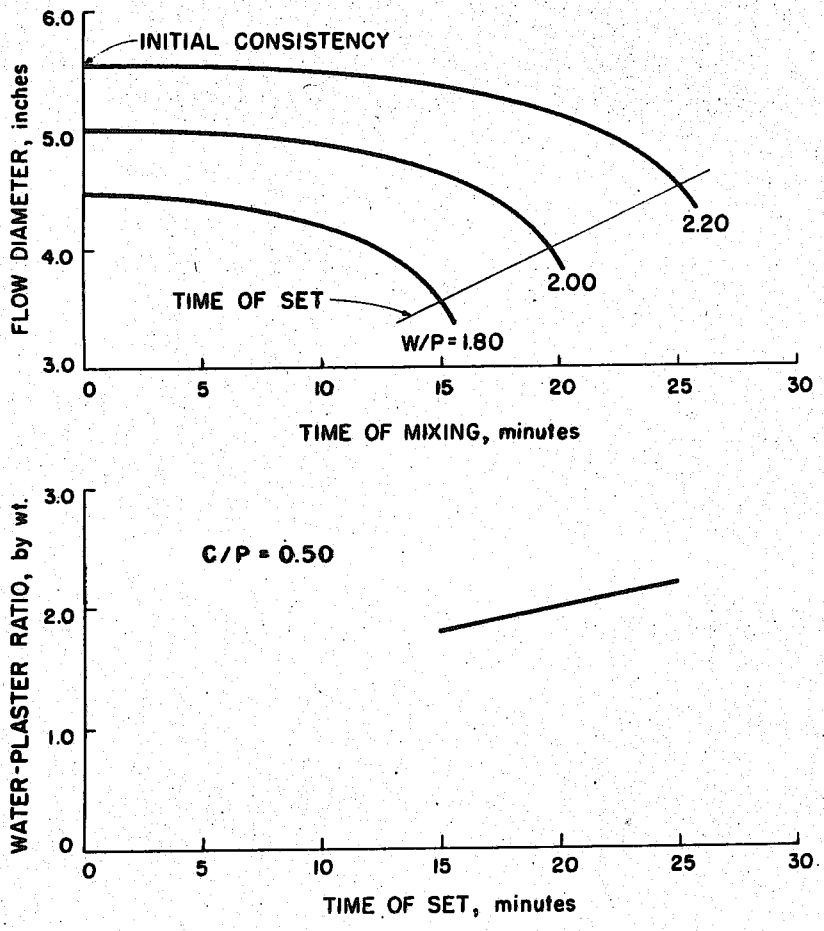


FIGURE 57 - EFFECT OF WATER ON CONSISTENCY AND SET

The Effect of Water and Celite on Consistency

As might be expected, an increase in the water content of a given plaster mixture increases its fluidity. Figure 57 shows that for a given proportion of plaster and celite, an increase in the water content increases

the flow diameter not only when first mixed, but also for the entire period during which the mixture remains fluid. The increased dispersal of the hydrated nuclei by additional water slows up both the thickening and the solidification of the mixture.

It will be recalled that the desired elastic modulus dictates the water-plaster ratio that must be used. If this results in too fluid a mixture, celite, with its high ratio of surface-to-volume, can be added to reduce the fluidity of the mixture. Figure 58 shows that for a given W/P, the flow diameter of a plaster-celite mixture is reduced as the celite-plaster ratio is increased. Conversely, as described above for a given C/P, flow diameter increases linearly with W/P.

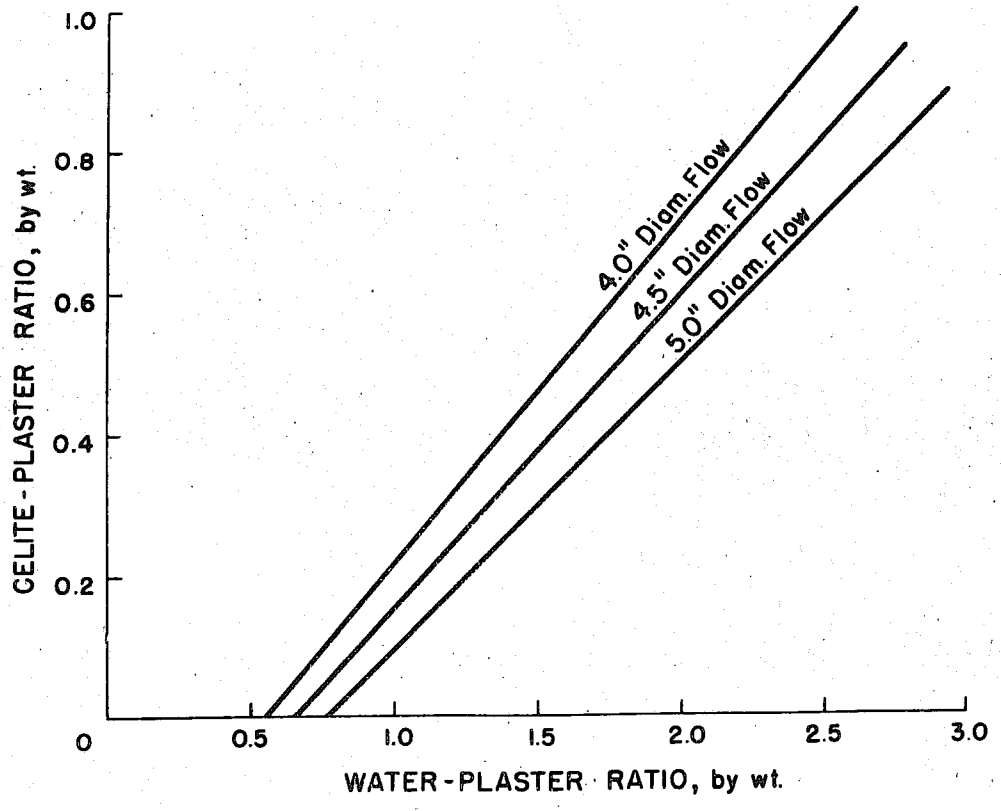


FIGURE 58 - EFFECT OF CELITE ON CONSISTENCY

## Time of Set

The setting of plaster is a continuous process involving a series of changes of state from a slurry of calcined calcium sulphate hemihydrate in water, through the intermediate stage of dissolved hemihydrate, to the completely recrystallized dihydrate. It can be seen that this dynamic process is quite similar to the setting of portland cement, although on a greatly accelerated time scale. Indeed, this close resemblance has led to the formulation of the ASTM Standard Test Method C26 for "Time of Setting" in which the same Vicat apparatus is used, as that used for testing the set of cement. For the ASTM test, "set" is considered to occur as soon as the thickening slurry offers resistance to the penetration of a 1 mm needle weighing 300 grams.

Experience with plaster-celite mixtures showed that under the retarding action of additional water and the various chemicals used, the flow diameter would remain essentially constant for a lengthy period. However, once crystallization had begun, it proceeded very rapidly to its conclusion. By defining "time of set" as the time at which the flow diameter had decreased by 1 inch, the remaining short time from "time of set" to complete crystallization was predictably nearly constant at 1-1/2 minutes. In this short interval, bleeding of water from the very dilute slurries used in the model was negligible.

## Effect of Water and Celite on Time of Set

In previous sections, it has been shown that the proportions of water and celite to plaster must both be varied together in order to obtain mixtures having a constant consistency. However, even though two mixtures may have the same consistency, the mixture having the higher W/P will take

longer to set. Beyond its original function of reducing the initial consistency, the celite contributes nothing to the thickening of the mixture. The stiffening comes from the gradual development of a tenuous network of crystals of the reconstituted dihydrate. Hence, the more they are separated by dilution, the longer it will take the crystals to form the network.

Figure 59 shows the variation of consistency with time for five mixtures having the same initial consistency, but in which W/P increased from 0.80 to 3.20, while C/P simultaneously increased from 0 to 1.00. For each combination, consistency decreased from the initial 5" to a minimal 3". (Below 3", the mixture will not flow readily through the cone of the consistometer.) As W/P and C/P increased, so too did the time to reach the 3" consistency.

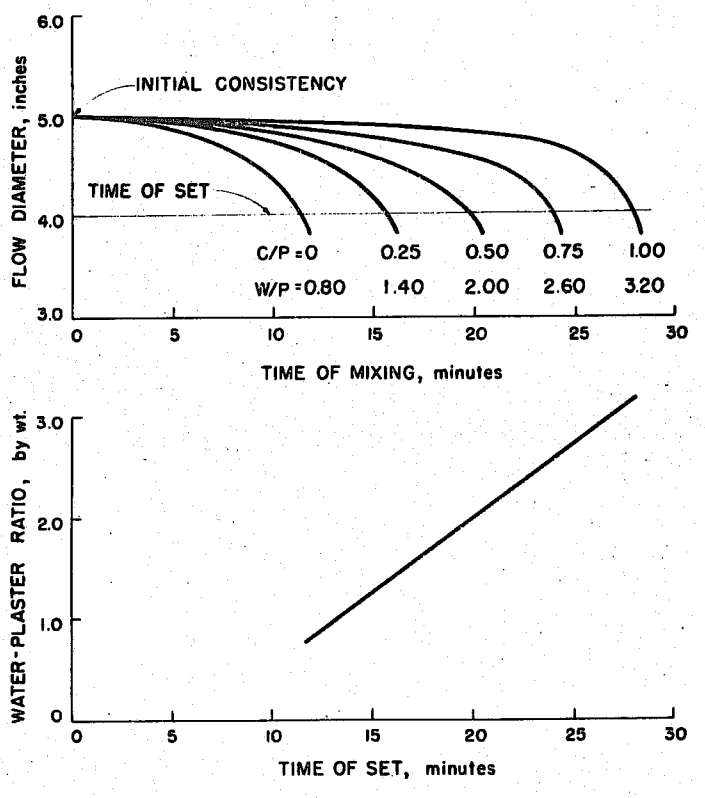


FIGURE 59 - EFFECT OF WATER AND CELITE ON TIME OF SET

By definition, "time of set" is the time when flow has decreased to 4". This time is plotted separately for the five mixtures, showing that time of set increased linearly from 12 minutes to 28 minutes, when W/P increased from 0.80 to 3.20.

Effect of Temperature on Time of Set

The temperature at which the ingredients are combined has a profound effect on the time of set of plaster mixtures. Consistency was determined at intervals for two plaster mixtures, identical except for their initial temperatures. Time of set from these two tests is plotted on Figure 60. It can be seen that the time of set was more than doubled, when the initial temperature of the mixtures was reduced from 63°F to 44°F. It can be noted that these data are in line with the common observation that reaction rate doubles with each 10°C rise in temperature. The curved line connecting the two points reflects this observation.

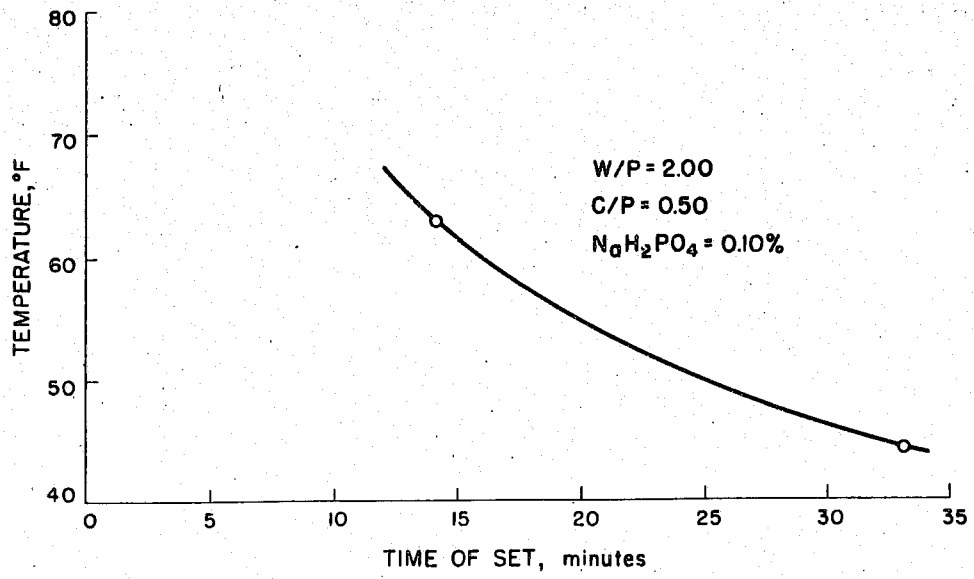


FIGURE 60 - EFFECT OF TEMPERATURE ON TIME OF SET

## Effect of Retarder on Time of Set

A retarder was needed for the model plaster to stretch out the working period for mixing and blending the materials before casting the plaster into the molds.

As its name implies, a retarder is a substance which when added to water, delays or retards the setting of a plaster mixture. Considering the sequential processes of solution, saturation, and crystallization involved in the setting of plaster, it has been shown[22] that certain substances delay set mainly by slowing down the rate of solution of the hemihydrate. Once the solution has reached the saturation point, crystallization proceeds at almost the same rate, regardless of how long it took to reach that point.

In studying how the hydration rates of gypsum plasters were affected by small amounts of dissolved substances, Coughlin, Conway, Koehler, and

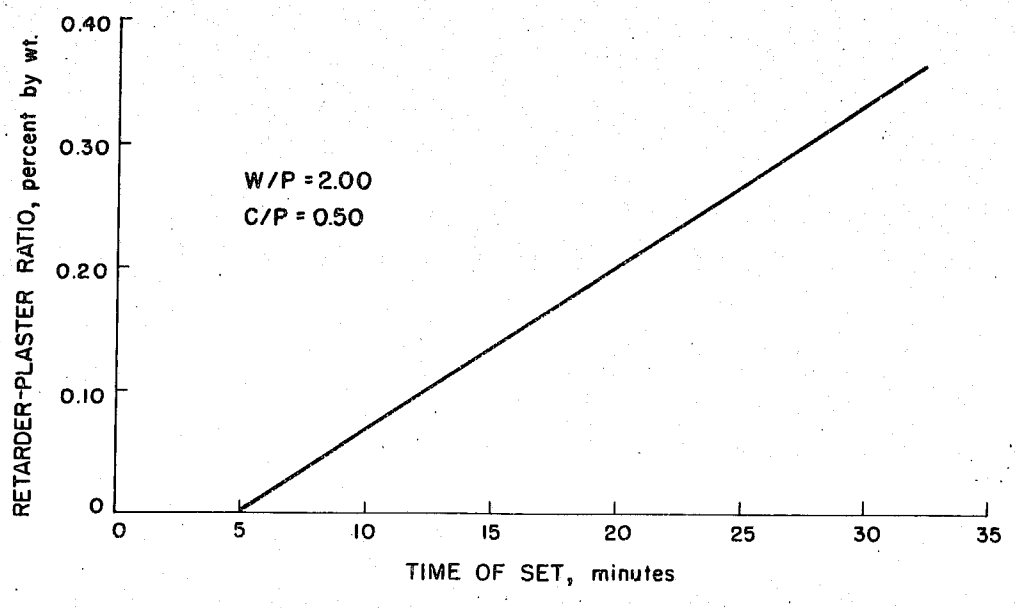


FIGURE 61 - EFFECT OF RETARDER ON TIME OF SET

Barry[23] concluded that mineral acids and salts of strong acids were accelerators, and that hydroxides, and salts of weak acids and strong bases were retarders.

Three phosphates were tested for the effect of concentration on delaying time of set: monobasic sodium phosphate $NaH_2PO_4 \cdot H_2O$, dibasic sodium phosphate $Na_2HPO_4 \cdot 12H_2O$, and a commercial water softener, sodium hexametaphosphate $(NaPO_3)_6$. Figure 61 shows that when small amounts of monobasic sodium phosphate were added to a plaster-celite mixture, the retardation of the time of set increased proportionally with the amount used. Similar effects were found for the other two retarders.

Effect of Retarder on Consistency

In addition to their effect on the time of set, retarders act as water reducing agents, affecting the consistency of the plaster mixture. The fluidity of a given flocculated suspension is increased when the ions of the retarding agent disperse the particles and break down the flocculated structure into a suspension of separate particles. Thus, for a given water-plaster ratio, increasing the relative quantity of retarder increases the fluidity of the mixture. Figure 62 shows the results of a number of tests made for plasters having the same water-plaster ratio, but varying the relative quantities of celite and of retarder. For a constant W/P and C/P, fluidity as measured by the flow diameter increases as the amount of retarder increases. With a given amount of retarder, fluidity can be decreased by increasing the amount of celite. Finally, to maintain a constant consistency, C/P must be increased as the amount of retarder is increased. If this simple relationship is ignored, a mixture having a desirable consistency without retarder will bleed excessively if a retarder is used.

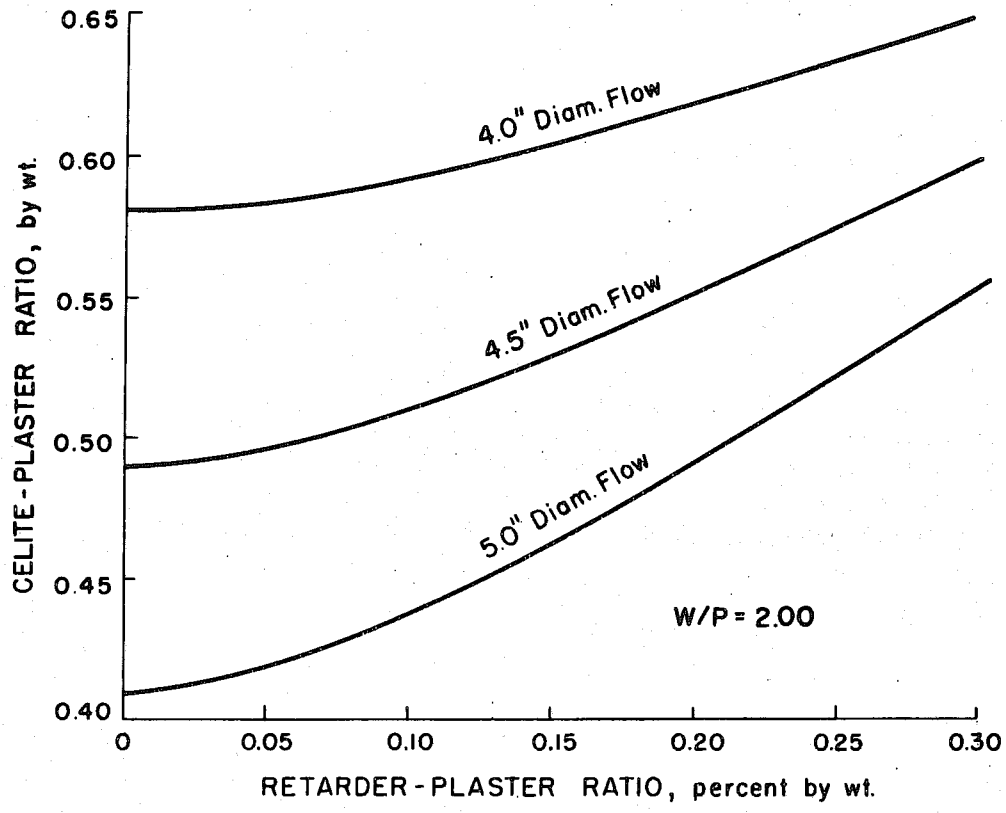


FIGURE 62 - EFFECT OF RETARDER ON CONSISTENCY

Volume Change During Setting

In discussing the volume changes that take place when hemihydrate with an excess of water hydrates to the dihydrate plus water, it is instructive to consider first the changes in the specific volume of the materials that enter into the hydration. The hemihydrate has a molecular weight of 145.16, and considering the relative amount of alpha- and beta-hemihydrate in the plaster used, an average specific gravity of 2.74, giving a specific volume of 52.98. The 3/2 molecules of water that combine with the hemihydrate to form the dihydrate have a specific volume of 27.02. Thus, the two materials together, before hydration, have a total specific volume of 80.00. Nonetheless, the dihydrate $CaSO_4 \cdot 2H_2O$ with its molecular weight of 172.18 has a

specific gravity of 2.32, yielding a specific volume of 74.21. Hydration has resulted in a decrease in specific volume from 80 to 4.21, a loss of 5.79 of 7.25 percent.

For a gram molecular weight mixture with a water-plaster ratio of 2.00, and a celite-plaster ratio of 0.50, before hydration the solid volume will be 52.98 cc for the hemihydrate, for the celite 31.5cc, and for the water 290.4cc. Of the total 290.4 cc of water, 27.02 cc enters into the hydration of gypsum, leaving 263.4 cc as the volume of free water. Thus, the total volume before hydration is 374.9cc. After the completion of hydration, the dihydrate has a volume of 74.21cc, the volume of the celite remains unchanged at 31.5cc, and the uncombined water also remains unchanged at a volume of 263.4 cc. Thus, after hydration, the total volume is 369.1cc, and the reduction of volume, as before is 5.8 cc. However, the percentage change spread over the larger base volume of 374.9 cc, has been reduced to 1.55 percent. Thus, it might be expected that the volume of the mixture would reduce 1-1/2 percent after hydration. If the gross apparent volume should remain unchanged, then there must have been created 1-1/2 percent internal voids, and the mass would have the capacity to take up this volume of water.

In fact, however, it is observed that the hydrating mass, rather than shrinking, actually expands by a fraction of a percent during hydration. As explained above, this creates internal voids under partical vacuum, and any free water on the surface is at once drawn into the mass. This has been described by some observers as "suction".[25]

Considerable speculation has arisen as to the cause of the expansion. In a previous section, it has been stated that upon heating gypsum, 3/4 of the water of crystallization is driven off to form the hemihydrate. Actually the process has a slight complication that is pertinent to the sequence of volume

changes that take place on setting. It has been noted[20] that when gypsum is heated, the temperature rise of the gypsum is not uniform, but a lag occurs during which the temperature remains nearly uniform at about 252°F until about 60% of the total water of crystallization has been driven off, and thence the temperature increases rather rapidly. Indeed, if the heating is not discontinued when 75% of the water of crystallization has been driven off, the reaction will continue until the anhydrite is formed.

It is considered by some that this lag, or induction period, represents the formation of an intermediate form of the dihydrate, with a different crystal form, the orthorhombic. The series of changes

$$\alpha\ CaSO_4 \cdot 2H_2O \rightleftharpoons \beta\ CaSO_4 \cdot 2H_2O \rightleftharpoons CaSO_4 \cdot 1/2H_2O + 3/2H_2O$$

Gypsum (monosymmetric) — Orthorhombic — Hemihydrate (Orthorhombic)

is considered completely reversible. According to Davis,[24] "Before gypsum can undergo dehydration to form the half-hydrate, it passes into the orthorhombic form of the dihydrate, and the latter is also the first product of the hydration of the half-hydrate." If it could be shown that the orthorhombic form of the dihydrate occupied a greater volume than gypsum, then the expansion of gypsum after setting would be complete elucidated. At any rate, this seems to explain the evolution of heat after the plaster has set. The heat is the product of the exothermic reation when the orthorhombic form reverts to the more stable form gypsum, and represent the recovery of the energy absorbed by the gypsum during the induction period.

One test was performed in an attempt to evaluate the setting expansion of a typical mixture used on the model, with the results shown on Figure 63.

The graphs shown on Figure 63 depict measurements made on a pair of 3 inch diameter by 12 inch high plaster cylinders, cast in cardboard molds.

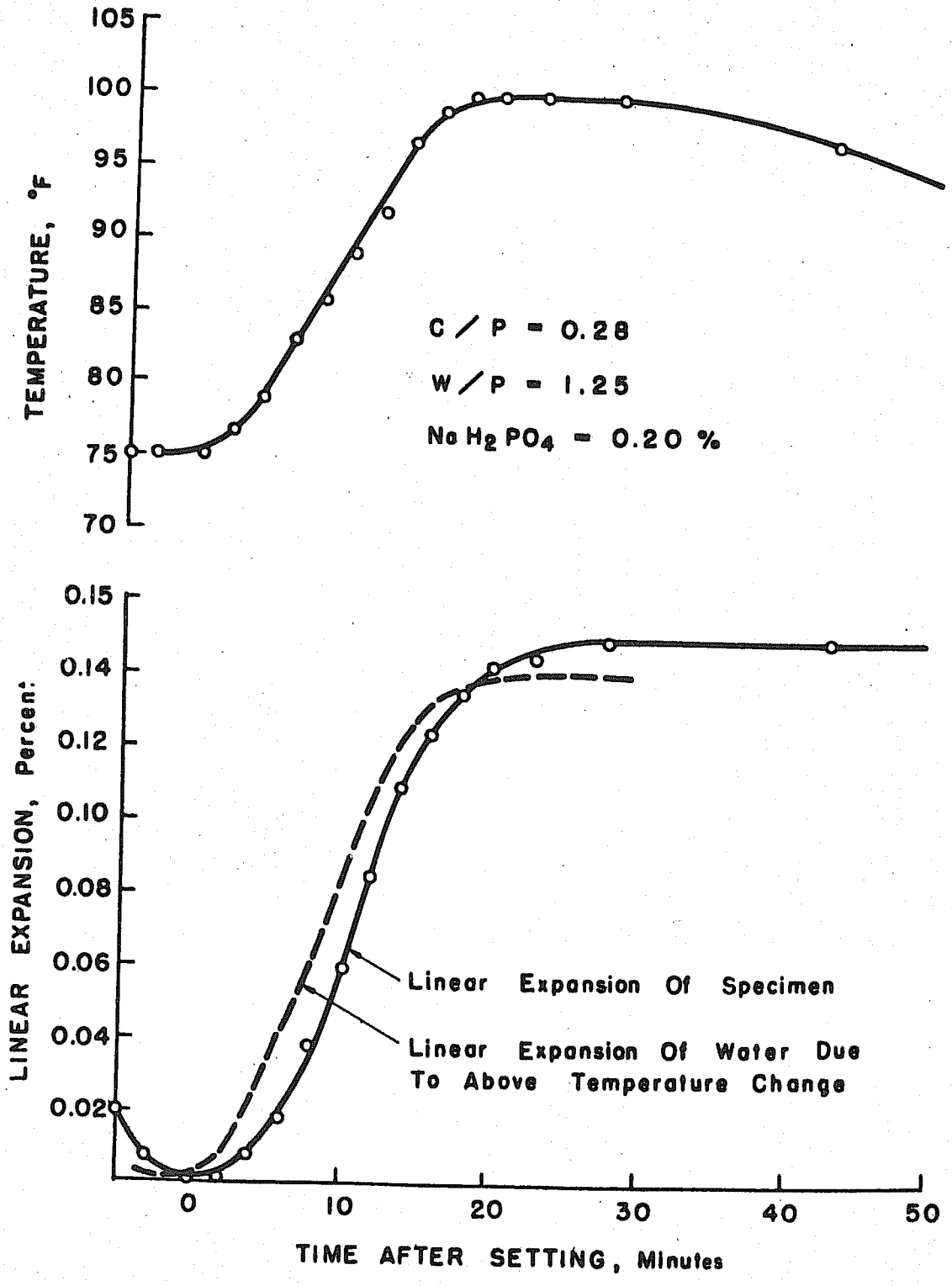


FIGURE 63 - TIME, TEMPERATURE AND VOLUMETRIC RELATIONSHIPS DURING HYDRATION OF PLASTER

One specimen was fitted with a dial gage bearing on a plastic plate which floated on the top of the plaster. Temperature was recorded for this specimen from a thermocouple embedded in its center. The other specimen was a companion cylinder used to determine set. After casting the specimens, the volume of the cylinder appeared to decrease, although much of this decrease must be ascribed to squeezing of the plaster paste past the plastic plate under the spring pressure of the dial gage. At any rate, this shrinkage ceased at set, which was indicated when the companion cylinder had gained so much strength that the cardboard mold could be stripped easily with no damage to the cylinder. This time is taken as zero time on the plot. Following set, as shown on the top graph, a linear and rapid temperature rise occurred during a period of about twenty minutes. Simultaneously, the cylinder began to expand, as shown in the lower graph, and continued to expand while heat was being evolved.

The dashed line in the lower graph is the theoretical volumetric expansion of pure water, when subjected to the temperature rise shown. The close correspondence of the observed volumetric expansion of the plaster with the computed volumetric expansion of water is marked.

The sequence of the setting of plaster, followed by the rapid evolution of heat does seem to lend support to the theory offered by Davis of the change of state of the dihydrate from the orthorhombic form to the monosymmetric form after setting. However, there are equally strong arguments that the induction period represents a thermodynamic process, and much more research is needed before the expansion of plaster on setting can be completely elucidated.

Shrinkage

At the very beginning of the materials investigation, two series of tests were run in an attempt to measure the shrinkage of plaster after setting. For the first series, bars similar to those used for testing shrinkage in cement mortars were used, but with no significant results, due to damage to the end plugs during stripping. A second series was made using 3 inch by 6 inch cylinders cast in steel molds with more protection on the end plugs, and these could be stripped successfully. While some results were obtained from this series, a re-evaluation of these data showed that the measurements were compounded of volume changes due to a number of sources, including among them temperature change, and the results are of no value. It was concluded from this series that shrinkage after set, for the plaster-celite mixture used, was of very little significance. This was further corroborated by the behavior of the foundation model. This indicated that while the expansion of the plaster mixture was of high significance in causing gaps in the foundation, there was no shrinkage after setting to off-set this expansive volume change. It can be seen from these qualitative remarks, that this area needs restudy with tests designed to evaluate the several phenomena.

Bleeding

From familiarity with cement-mortar mixtures, it was at first supposed that bleeding would be a common characteristic of all plaster mixtures. While there are some similarities between the bleeding of plaster and cement mixtures, the time scale regarding the set of the two mixtures is so dissimilar that bleeding can be completely eliminated from plaster mixtures by correct technique. In both types of mixtures, bleeding is actually a misnomer, since only a settlement phenomenon is active. In

cement mortars, set is so long delayed that the heavy particles can settle downward through the water for periods up to 90 minutes before enough of a structure has been initiated to resist this settlement. For the plaster mixtures, it was found that excessive settlement or bleeding occurred in cylinders that had been poured as soon as the materials had been blended. However, if mixing of the plaster mixture were continued until just before set, as indicated by a 1 inch decrease of the flow diameter, then no bleeding whatsoever would occur. Intermediate values of settlement and bleeding were found for intermediate mixing times. This factor became a highly significant part of the mixing technique for casting the model. Blending and mixing of the ingredients of a pour was continued until the initial flow diameter had decreased 1 inch. If poured at this time, sufficient time remained for the mold to be completely filled, and then the plaster would set within about two minutes. In the one case where pouring was initiated too soon, excessive bleeding resulted.

Effect of Mixing Time on Modulus of Elasticity

Having established controls so that time of set could be extended at will through the use of retarders, it was desirable to see if extended mixing had an effect on the modulus of elasticity of set plaster. Accordingly, for a number of mixes containing retarders, large batches were continuously mixed from which, at selected intervals, a cylinder was cast. Figure 64 shows the results of a typical test of this type. It can be seen that increasing the mixing time causes an increase in the modulus of elasticity up to a certain maximum, followed by a sharp decrease, although the actual shape of the curve differed with different plasters and celites. In fact, final selection of the plaster used in the model was primarily made on a plaster that exhibited

a very flat peak. For this plaster, considerable latitude could be allowed in the optimum time of pour, in order to have a uniform strength of plaster in the poured model. Even though the elasticity was affected by the time of mixing, consistency remained practically constant until just before final set occurred, as shown in the top part of the figure.

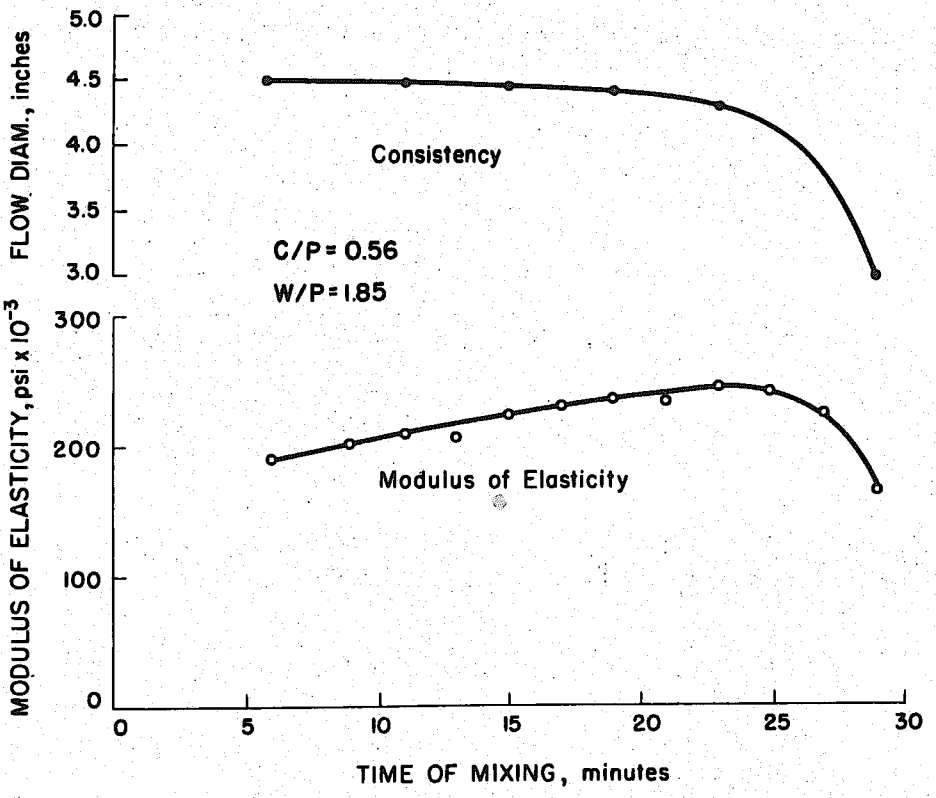


FIGURE 64 - EFFECT OF MIXING TIME ON CONSISTENCY AND MODULUS OF ELASTICITY

## Creep

A number of tests were run to evaluate creep in plaster-celite mixtures in order to predict the effect of creep on the validity of the strain measurements made on the model. Creep was measured on compression cylinders, and on beams in flexure. Both single-cycle and repeated-cycle

loadings were used.

The results of one of the flexural tests are shown in Figure 65. This test consisted of a thirty minute loaded period followed by a thirty minute unloaded period, and repeated for five complete cycles. A study of the plotted center deflections shows that two effects are superimposed. Each individual loading or unloading results in an immediate elastic deformation of large magnitude, followed by continued creep deformation at a decreasing rate. It will be noted that the total deformation steadily increases throughout the five cycles, shown by the gradual increase in the value by which the deflection fails to return to zero upon release of load. This is a secondary creep effect, caused by the average or half load, and reflects the fact that the average of

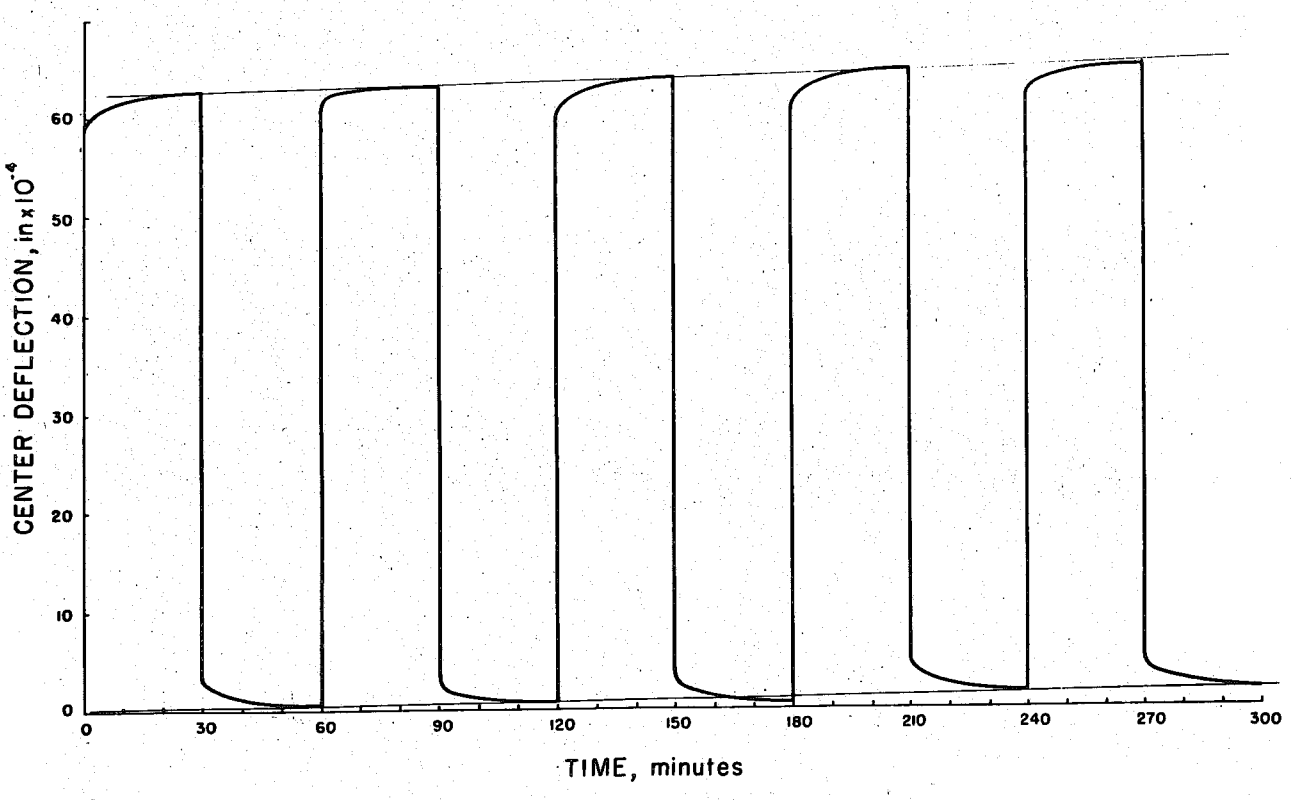


FIGURE 65 - EFFECT OF REPEATED LOADING ON FLEXURAL CREEP

the loaded and unloaded period is the same in the long run as a sustained load of half the magnitude of the original load maintained for the full five hours of the test. However, it can be noted that differences between corresponding points in the flattened portions of any two subsequent creep curves is nearly constant. Consequently, the measurement schedule for the strains in the model was designed to allow the initial rapid creep to take place, and to make the strain measurements during the last portion of each loaded or unloaded cycle, when creep is much slower, in order to eliminate as much as possible any drift in the indicated strains.

Design of Heavy Plaster Mixtures

In connection with the preliminary studies for determining dead load stresses in the model by the method of inversion, an investigation was begun into the design of high-density plaster mixtures. Since the role of the celite in the plaster-celite mixtures was solely to provide a large surface to hold the water in contact with the plaster, it was reasonable to assume that a heavier plaster having similar elastic properties could be produced by substituting a heavier powdered material for the celite. After a brief survey of the cost, behavior, and availability of such high-density materials as litharge, magnetite, and barite, the latter was chosen. Powdered barite is easily available at moderate cost, since it is a common ingredient of oil well drilling mud.

The design of high-density plaster mixtures is based on two principles:

1. The water and plaster in the mixture control the strength through the water-plaster ratio; the other powdered materials control consistency and density.
2. If each of the ingredients is mixed with water to a common consistency, the consistency of the combined mix will be the same, or: the consistency of the mix equals the sum of the consistencies of the parts.

The utilization of the second principle requires the determination of a new property, termed the "specific consistency", which is the number of pounds of water that must be mixed with a pound of dry powdered ingredient to give a specified consistency, in this case, a 3 inch flow diameter. For the materials used in the high-density plaster mixture, the basic properties were determined as shown in Table 8.

TABLE 8

Consistency Characteristics
(For 3 inch flow diameter)

| Ingredient | Specific Gravity | Specific Consistency |
|---|---|---|
| Plaster, P | 2.73 | 0.56 |
| Barite, B | 4.23 | 0.25 |
| Celite, C | 2.30 | 1.78 |

Thus, for a consistency represented by a flow diameter of 3 inches, the total weight of mixing water W required for a mixture of a plaster P with two inert materials B and C having density $\gamma$, specific gravity $\rho$, and specific consistency S will be

$$W = S_P P + S_B B + S_C C \qquad (1)$$

The total volume of the wet mixture is equal to the sum of the solid volumes of the dry ingredients plus the volume of the water, or

$$V = \frac{1}{\gamma_W}\left(\frac{P}{\rho_P} + \frac{B}{\rho_B} + \frac{C}{\rho_C} + W\right) \qquad (2)$$

If K is the fraction of water bound to the plaster by hydration (0.186) the remainder of the water being free to evaporate from the set plaster, then

the dry weight of the set plaster mixture M is:

$$W_M = (1+K)P + C + B \tag{3}$$

and the dry density can be expressed as

$$\gamma_M = \gamma_W \frac{\frac{B}{P}(S_C - S_B) + \frac{W}{P} + (1+K)S_C - S_P}{\frac{B}{P}\left(\frac{S_C}{\rho_P} - \frac{S_B}{\rho_C}\right) + \frac{W}{P}\left(S_C + \frac{1}{\rho_a}\right) + \left(\frac{S_C}{\rho_P} - \frac{S_P}{\rho_C}\right)} \tag{4}$$

For the specific case of the design of high-density plaster mixtures having a flow diameter of 3 inches, values from Table 8 are substituted in Equation (1) to give

$$W = 0.56P + 0.25B + 1.78C \tag{5}$$

which reduces to

$$\frac{C}{P} = 0.56\frac{W}{P} - 0.14\frac{B}{P} - 0.31 \tag{6}$$

Similarly, substituting values from Table 8 in Equation (4), and remembering that K is 0.186 we obtain

$$\gamma_M = 62.4\,\frac{1.53\frac{B}{P} + \frac{W}{P} + 1.56}{.313\frac{B}{P} + 2.22\frac{W}{P} + .411} \tag{7}$$

$$\gamma_M = \frac{95.5\frac{B}{P} + 62.4\frac{W}{P} + 97.2}{.311\frac{B}{P} + 2.22\frac{W}{P} + .411} \tag{8}$$

Equations (6) and (8) have been plotted on the design chart shown as Figure 66, which give all the variables necessary to design a high-density plaster mixture having a 3 inch flow diameter. The parameters of this figure are the water-plaster ratio, W/P, and the barite-plaster ratio, B/P. Equation (6), giving celite-plaster ratio C/P in terms of W/P and B/P, is plotted as the familty of light dashed lines. Equation (8), giving the dry density of the mixture in terms of the same two parameters, is plotted as the family of heavy full lines.

If a mixture with an elastic modulus of say 110,000 psi and a dry density of 100 pcf is desired, a glance at Figure 50 shows that this elasticity can be secured with a W/P of 3.00. Entering the design chart with W/P of 3.00, it can be seen that C/P must equal 0.43, and B/P must equal 6.70. No other quantities need be determined. In a number of mixtures that have been made, the density determined in the dried plaster differed from those predicted by the design chart by less than 1 percent.

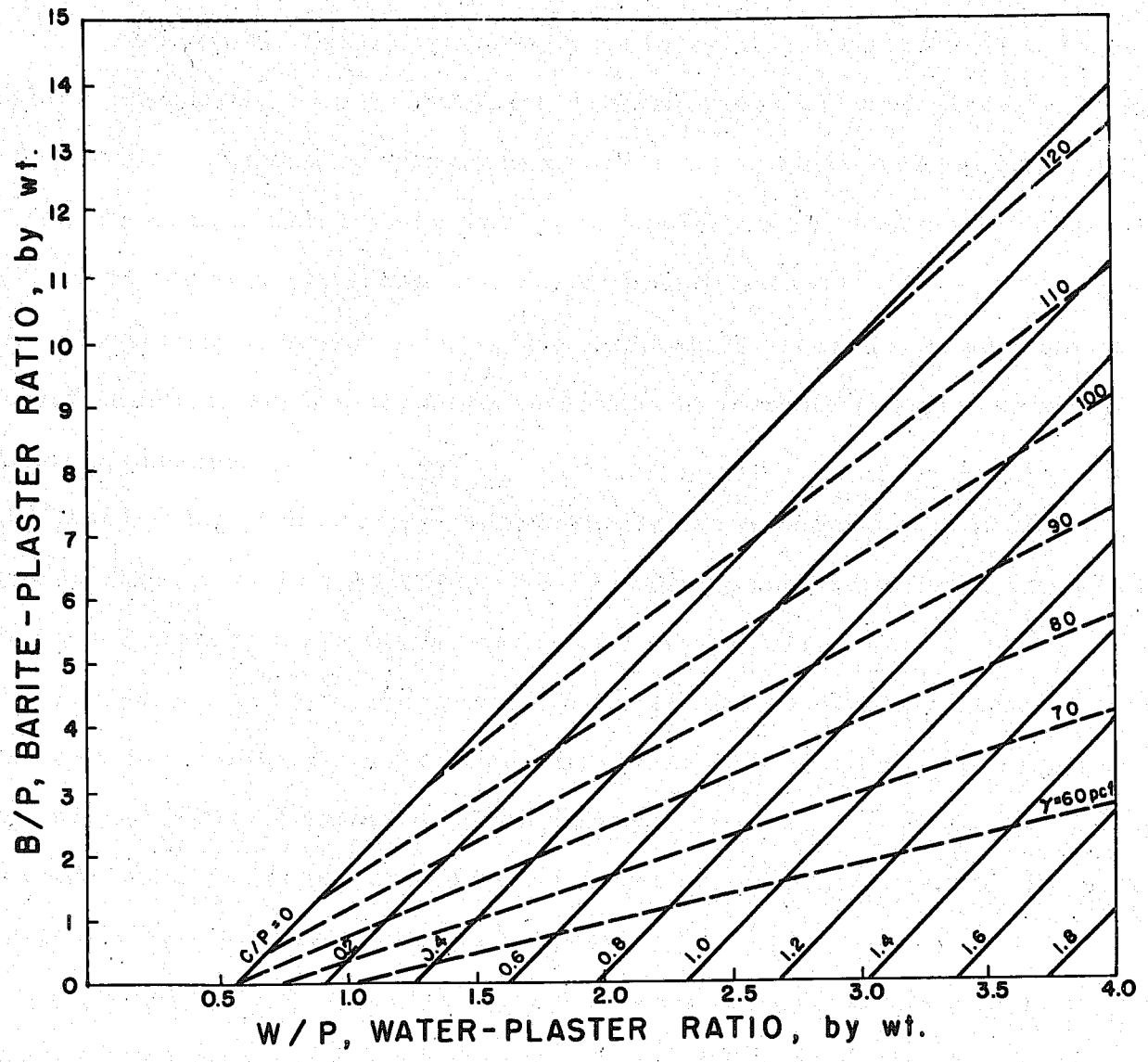


FIGURE 66 - DESIGN CHART FOR HEAVY PLASTER MIXTURES

6. Strength and elasticity of plaster mixtures are profoundly affected by the water content when mixed, and for any degree of drying.

7. The initial water content of a mixture controls its consistency, and by dispersion of the crystal structure, also controls its ultimate strength potential.

8. For a mixture having a given initial water-plaster ratio, the strength will increase as the non-combined water is removed, up to a water content of 18.6% which is the point when all uncombined water has been removed. Any further reduction in water content is at the expense of the water combined in the crystallized plaster, and causes reduction of strength.

9. The tensile strength of a plaster mixture is one fifth to one sixth the corresponding compressive strength of the same mixture at the same moisture content.

10. Poisson's ratio of plaster-celite mixtures ranged from 0.22 to 0.25.

11. No matter what the effect of the water-plaster ratio of the original mixture, or its subsequent state of dryness on the strength and elasticity of a plaster mixture, imminence of failure can be judged by a maximum strain of 2200 microinches per inch in compression, or 370 microinches per inch in tension.

12. Increasing the water content of a plaster mixture decreases its viscosity, and increasing the amount of celite in the mixture increases its viscosity.

13. Time of set of plaster mixtures can be controlled at will by chemical additives that control the rate of solution. The retardation of set is proportional to the amount of retarder added.

14. Time of set is also dependent to some extent on the water-plaster ratio since increased water content disperses the nuclei of the crystalizing plaster and delays the formation of a definite crystaline structure.

15. Retarders may be surface-active agents, increasing the effect of the water present, and hence increasing the fluidity of the mixture. Some adjustment to the mixture may be needed when using a retarder, decreasing the water in order to maintain the same consistency.

16. In common with many other chemical reactions, time of set is affected by temperature. Time of set was doubled by dropping the temperature of the ingredients by $14^{\circ}F$.

17. Despite the fact that the products of hydration of plaster occupy less solid volume than that of the materials entering into the reaction, plaster swells upon hydration. This appears to be closely tied to the heat of hydration or crystallization.

18. Bleeding of plaster mixtures can be avoided by delaying casting until just before set takes place.

19. The length of the time of mixing of plaster mixtures has some influence on the resulting strength and elasticity of the hardened plaster: the longer the mixing time, the higher the modulus of elasticity. This property varies with the individual plaster.

20. Hardened plaster mixtures creep under moderate load at room temperatures.

21. Three-component plaster mixtures can be designed to specified density and strength once each ingredient's specific gravity and specific consistency have been determined, in addition to the water-plaster ratio curve for strength.

22. The specific relationship governing all the foregoing conclusions for any particular plaster are probably dependent on the relative amounts of alpha- and beta-hemihydrate in the calcined plaster.

## REFERENCES


1. Banks, Harvey O., "The California Water Plan," Bulletin No. 3, State of California, Department of Water Resources, Division of Resources Planning, May, 1957

2. Raphael, Jerome M., Progress Report, "Oroville Dam Model Tests" University of California, June 13, 1957

3. Raphael, Jerome M., Progress Report, "Oroville Dam Model Studies," University of California, July 15, 1958

4. Raphael, Jerome M., Feasibility Report "Determination of Dead Load Stresses, Oroville Dam Model Studies, July 17, 1958

5. Raphael, Jerome M., Progress Report, "Oroville Dam Model Studies," November 12, 1958

6. Eberhart, Howard D., "Photoelastic Analysis of the Concrete Core Block for Oroville Dam," Progress Report to Department of Water Resources, State of California, March, 1958

7. Raphael, Jerome M., "Crustal Disturbances in the Lake Mead Area," U. S. Bureau of Reclamation, Engineering Monograph No. 21, August, 1954

8. Raphael, Jerome M., "The Development of Stresses in Shasta Dam," Trans. ASCE, Vol. 118, 1953

9. Pirtz, David, "Tests on Models of Rock-Fill Dams," M. S. Thesis, University of California, June, 1950

10. Meriam, J. L., R. F. Steidel, G. W. Brown, and P. T. Lyman, "Thermal Stresses in the S. S. Boulder Victory," Journal of Ship Research, V. II, No. 2, October, 1958

11. Wilson, John Sigismund, William Gore, "Stresses in Dams: An Experimental Investigation by Means of India-Rubber Models," Paper No. 3705, Proc. Inst. C. E. V. 172, pt. 2. 1908

12. Oberti, G., "The Aid of Models in the Study of Static Behavior of Large Dams in Concrete Built in Successive Stages", I. S. M. E. S. Publ. No. 19, Dec. 1958, Istituto Spesimentale Modelli & Stoutual (Also see 6th Congress on Large Dams, 1958)

13. Rocha, Manuel, J. Laginha Serafim, "Analysis of Concrete Dams by Model Tests," Communication No. C36, 5th Congress on Large Dams, Paris, 1955

14. Biot, M. A., "Distributed Gravity and Temperature Loading in Two-Dimensional Elasticity Replaced by Boundary Pressures and Dislocations," J. Applied Mechanics, V. 2, 1955

15. Polivka, J. J., "Analysis of Gravity Load Stresses by Photoelastic Methods," Proc. 16th Semi-Annual Eastern Photoelasticity Conference, 1942

16. Armour Research Foundation, "Experimental Stress Analysis of the Bekhme Dam," Final Report, Privately issued for Harza Engineering Company, December 1956

17. Dukleth, G. W., "Arch Analysis by Influence Lines," Unpublished Report to California Department of Water Resources, Dec. 1957

18. Lavoisier, A. L., Acad. Sci., Compt. Rend.," Feb. 27, 1765 and March 16, 1766, Oevres

19. Kelley, K. K., J. C. Southard, and C. T. Anderson, "Thermodynamic Properties of Gypsum and Its Dehydration Products," Technical Paper 625, U. S. Bureau of Mines, 1941

20. Riddell, W. C., "Physical Properties of Calcined Gypsum," Rock Products, V. 53., No. 5, May 1950

21. Simonds, A. W. "Construction of the Plaster and Celite Model of Hoover Dam," Bureau of Reclamation Techanical Memorandum No. 306, October 1, 1932

22. Riddell, W. C., "Effect of Some Inorganic and Organic Compounds on the Solubility, Setting Time and Tensile Strength of Calcined Gypsum," Rock Products, V. 57, No. 10, October, 1954

23. Coughlin, J. P., K. C. Conway, M. F. Koehler, and D. F. Barry, "Hydration-Rate Studies of Gypsum Plasters: Effects of Small Amounts of Dissolved Substances," Bureau of Mines, Report of Investigations 5477, 1959

24. Davis, W. A., "The Nature of the Changes Involved in the Production and Setting of Plaster of Paris," Jl. Soc. Chem. Ind., V. XXVI No. 13, July 15, 1907

25. O'Kelly, B. M., "Physical Changes in Setting Gypsum Plaster," Technical Paper 75, ASTM Bulletin, No. 237, April 1959